THE IMPORTANCE OF RADIAL MIGRATION TO SPIRAL GALAXY EVOLUTION

by

Kathryne J. Daniel

A dissertation submitted to The Johns Hopkins University in conformity with the requirements for the degree of Doctor of Philosophy.

Baltimore, Maryland

August, 2015

Abstract

Spiral galaxy evolution is frequently considered in the context of environment, but internal processes may also play an important role. One such process, called "radial migration", rearranges the angular momentum distribution of the disk without causing kinematic heating. Should radial migration be efficient, it could cause a substantial fraction of disk stars to move large radial distances over the lifetime of the disk, thus having significant impact on its kinematic, structural and chemical evolution. However, clues to its efficiency from observational and simulated data are inconclusive and insight from analytic studies is limited. We here aim to build an analytic framework for understanding the physics important to the efficiency of radial migration. In order for a star to migrate radially, it must first be in a "trapped" orbit (a family of orbits that occurs near corotation) due to a transient spiral pattern. The efficiency of radial migration depends on both the duty cycle for transient patterns and the RMS change in orbital angular momentum from each pattern, $\langle(\Delta L_z)^2\rangle^{1/2}$. This work focuses on the physics that determines the magnitude of $\langle(\Delta L_z)^2\rangle^{1/2}$, which increases with increasing fraction of and radial excursions for stars in trapped orbits.

ABSTRACT

In this work, we derive both an expression for the maximum radial excursion of a trapped orbit and an analytic "capture criterion" that predicts whether or not a disk star with finite random orbital energy is in a trapped orbit. We then use the capture criterion, in a series of disk galaxy models, to find the fraction of stars in trapped orbits.

We show it is primarily a star's orbital angular momentum that determines whether or not it is in a trapped orbit. For an ensemble of stars, the trapped fraction decreases with increasing radial velocity dispersion as $e^{-\sigma_R^2}$. Further, the maximum radial excursions for trapped orbits is smaller than excursions expected from the random motions of stars in MW-like spirals. We conclude that radial migration may play a role in the evolution of disk galaxies, but it is not important enough to form major structural components.

Primary Reader: Rosemary F. G. Wyse

Secondary Reader: Alexander Szalay

Acknowledgments

First and foremost, I would like to express my deepest gratitude to Rosemary Wyse. I have not met a more brilliant person than Rosie and it has been a privilege to grow as a scientist under her tutelage. She encouraged my curiosity and guided me toward finding my own answers. From Rosie, I have learned how to successfully be an independent thinker, what it takes to be a leader in the field, how to clearly express my thoughts, and how to challenge the status quo with grace. More than anything else, perhaps, she taught me to believe in myself. Her support over the years was more than I ever could have asked for. Thank you, Rosie, for giving me more than I can say in this small space.

It truly takes a village to raise a doctoral student, especially a doctoral student who is raising two elementary school students. To all my parents, thank you for feeding me Cosmos for breakfast, self evaluation for lunch, and a healthy dose of unconditional love for dinner. Thank you for bailing me out when my graduate student salary wasn't enough to make ends meet, for providing a loving "second home" for my children when I had a deadline, and for Granpa Summer Camp. To my two sisters, Heather and

ACKNOWLEDGMENTS

Sarah, your love, support in all things, and humor was more necessary than you can know. To the entire Daniel-Allison-Miller-Adams-Stamis-Hertz entourage, thank you for supporting me on this academic journey.

To the administrative staff, especially Carm and Pam, thank you for picking up my slack when I was too self-absorbed as an aspiring academic to care for myself.

Jennifer, Johti, my teacher and dearest friend, thank you for always being there when I needed you. Whether our lives remain parallel or diverge dramatically, I'm sure we will remain the best of friends for the rest of our days.

Cathy, your generosity in all things is unmatched. Your homemade meals and honest conversations were always an oasis in a land of hard numbers and careful diplomacy.

Christopher Paul, you are my Sun and stars, my soul mate. Thank you for keeping me warm when I was cold and for bringing lightness into my life while I trudged to the finish line. I'm so excited to embark on the next chapter of life with you.

Finally, Rowan and Nyala, you have never known a time when Mom wasn't in school. Many nights, I worked in the hall between your bedrooms (and between lullabies) while you fell asleep. Thank you for tolerating my strange schedule. I hope you find the dedication I have to my work to be inspiring rather than neglectful! I love you both with every fiber of my being and I am more in awe of you two each day than I ever could be of something so simple as astrophysics.

Dedication

This thesis is dedicated to my two children. Rowan and Nyala, you are my heart of hearts. May your inquisitive minds carry you toward discovering your greatest dreams.

Contents

Abstract **ii**

Acknowledgments **iv**

List of Tables **xi**

List of Figures **xii**

1 Introduction **1**

1.1 Introduction to Radial Migration 3

1.2 Theoretical Exploration 5

1.3 Observational Signatures 10

1.4 Motivation for Analytic Work 14

2 Underlying Physics for Radial Migration **17**

2.1 Definition of a Trapped Orbit 17

2.2 Underlying Physics 18

3 The Model **27**

3.1 Model for the Disk Potential 28

3.2 Models for the Kinematics of the Disk 29

3.2.1 Gaussian Velocity Distribution 29

3.2.2 Distribution Function for a Warm Disk 33

4 Analytic Criterion for Capture at Corotation **35**

4.1 Stars with Zero Random Orbital Energy 35

4.1.1 Capture Region 39

4.2 Stars with Non-Zero Random Orbital Energy 40

4.3 Special Case: Power-Law Potential 43

4.4 Numerical Exploration 51

4.4.1 The Approach 51

4.4.2 Testing the Capture Criteria 52

4.4.3 Scattering 58

4.5 Capture for a Non-Steady Spiral Pattern 65

5 The Amplitude of Radial Excursions **75**

5.1 Analytic Evaluation of the Radial Excursions from a Spiral 78

5.2 Important Observational Constraints 83

6 Modeling the Distribution of Trapped Orbits **87**

6.1 The Approach 89

6.2 Trapped Fraction for a Constant Radial Velocity Dispersion 91

6.2.1 Radial Distribution of the Fraction of Stars in Trapped Orbits 92

6.2.2 The Integrated Fraction of Stars in Trapped Orbits 98

6.2.3 The Functional Dependencies of the Integrated Fraction . . . 104

6.2.4 Comparison to Previous Work 109

6.3 Trapped Fraction for Radially Dependent Velocity Dispersion 111

6.3.1 Prescriptions for the Radial Velocity Dispersion 112

6.3.2 Orbital Angular Momentum Distributions 114

6.3.3 Trapped Fraction for a Given Normalization of Velocity Dispersion117

6.3.4 Trapped Fraction for a Given Radius of Corotation 121

6.4 Discussion 124

7 Summary & Conclusions **141**

7.1 Summary 142

7.1.1 Capture Criterion 142

7.1.2 Amplitude of Radial Excursions 144

7.1.3 Mixed Fraction 145

7.2 Conclusions 147

8 Future Work **150**

A Two Capture Criteria **153**

A.1 Criterion used by Sellwood & Binney 154

A.2 Criterion derived by Contopoulos 157

Curriculum Vitae **168**

List of Tables

3.1 Adopted parameter values 27

6.1 Linear best-fit parameters for the integrated fraction 106
6.2 Gaussian best-fit parameters for the integrated fraction 106
6.3 Important parameters for the models presented in §6.3 112

List of Figures

2.1 Capture region and the trajectory of a trapped orbit 25
2.2 Lindblad diagram. 26

4.1 Significance of higher order term in generalized capture criterion . . . 46
4.2 Capture criterion in phase space 68
4.3 Relation between orbital trajectory and capture criterion: Un-trapped 69
4.4 Relation between orbital trajectory and capture criterion: Un-trapped 70
4.5 Relation between orbital trajectory and capture criterion: Trapped . 70
4.6 Azimuthal dependence of capture criterion 71
4.7 Properties of a trapped orbit that is not scattered 72
4.8 Properties of a trapped orbit that is scattered away from resonance . 73
4.9 Properties of a trapped orbit that is scattered from resonant overlap . 74

5.1 Maximum radial excursions for trapped orbits 86

6.1 Capture region for potential with parameter values from Table 3.1. . 127
6.2 Contour maps of $f_G(\mathbf{v})_{\mathbf{x}}$ for two different radial coordinates 128
6.3 Random azimuthal velocity distributions 129
6.4 Radial distributions of trapped orbits: Asymmetric drift 130
6.5 Integrated fraction and associated measures: Asymmetric drift 131
6.6 Trapped mass ratios: Asymmetric drift 132
6.7 Best fit curves for $\mathcal{F}_1$, $\mathcal{F}_2$, and $\mathcal{F}_{FWHM}$ 133
6.8 Integrated fraction and associated measures: Spiral strength 134
6.9 Integrated fraction and associated measures: Radius of corotation . . 135
6.10 Prescriptions for the radial velocity dispersion profile 136
6.11 Radial distribution of L_z: Three models presented in Table 6.3 137
6.12 Integrated fraction and associated measures: Normalization of $\sigma_R(R)$ 138
6.13 Radial distribution of L_z: Normalization of $\sigma_R(R)$ 139
6.14 Integrated fraction and associated measures: Radius of corotation . . 140

Chapter 1

Introduction

Spiral galaxies in the local universe have several common characteristics. These include thick and thin disk components, both of which have an exponential surface density profile (e.g. van der Kruit, 1987; Jurić et al., 2008; de Jong et al., 2010). Thick disks are composed of old stars and have an exponential scale height a few times that of the thin disk (e.g. Gilmore & Reid, 1983; Gilmore & Wyse, 1985; Allende Prieto et al., 2006). Thin disks are composed of gas and stars in all stages of evolution and host spiral patterns that have a range of morphologies. Beyond the radius at which star formation is expected to take place, there frequently exists an outer disk that is populated with old stars and can have one of a range of surface density profiles (e.g. Pohlen & Trujillo, 2006). Although these characteristics are observed to exist, many fundamental questions remain unanswered. A few of these are: What is the origin of the thick and outer disks? What is the origin of the exponential sur-

face density profile? What is the nature of spiral structure (Goldreich & Lynden-Bell, 1965; Lin & Shu, 1966; Julian & Toomre, 1966; Sellwood & Carlberg, 2014) and what causes spiral disruption (e.g. D'Onghia et al., 2013; Sellwood & Carlberg, 2014)? Each of these outstanding questions represents a topic that is central to understanding galaxy evolution and each will be explored in this work.

Galaxies are known not to evolve in isolation, but rather under the influence of external effects such as interactions with neighbors, or gas infall/outflow (see Somerville & Davé, 2014, for a review). In addition, galaxies are also subject to secular internal processes (see Sellwood, 2014a; Kormendy, 2013, and references therein). As such, a wide range of processes have been identified that drive the evolution of spiral galaxies, each producing a set of kinematic and chemical signatures. These processes include, but are certainly not limited to, major and minor mergers, smooth and clumpy accretion, feedback, close encounters, the chemical evolution of the gas and stars in and around galaxies, and kinematic heating via inhomogeneities in the density of the thin disk.

In a groundbreaking work, Sellwood & Binney (2002) proposed that transient spiral arms could permanently change the mean orbital radii of stars and gas clouds in the disk, without increasing their random motions. This "radial migration" across the disk would mix stellar populations and gas without inducing kinematic heating, thus challenging the following two long held assumptions: a permanent change in the mean orbital radius of a star requires an increase in its random motions, and a

population of stars primarily maintains the mean orbital radius of its birth. Should radial migration be important to galaxy evolution, the interpretation of the chemical abundance patterns and kinematics in the disk of spiral galaxies would have to be reevaluated.

Since its introduction, radial migration has been invoked as a formation mechanism for thick and outer disks, as being responsible for the origin of the exponential surface density profile, and to explain the distribution of chemical abundances of solar neighborhood stars. (We discuss each of these points in detail below.) This work aims to place constraints on the importance of radial migration, and thus to assist in understanding the evolution of spiral galaxies.

1.1 Introduction to Radial Migration

Sellwood & Binney (2002) identified the process resulting in what is now commonly referred to as "radial migration". They used both analytic and numerical techniques to demonstrate that under certain circumstances a transient spiral arm in a two-dimensional disk can permanently change the orbital angular momentum of a star without causing a significant change in its orbital random energy, ΔE_{ran}. They showed that in the epicyclic approximation, the increase in orbital random energy of a star due to an encounter with a spiral of pattern speed Ω_p, is related to its change

in orbital angular momentum, ΔL_z, as follows:

$$\Delta E_{ran} \propto (\Omega_g - \Omega_p)\Delta L_z \tag{1.1}$$

where Ω_g is the orbital frequency of the star's guiding center. Thus a star that is on a nearly circular orbit with guiding center radius approximately equal to the corotation radius (R_{CR}, at which the circular orbital frequency, $\Omega_c(R_{CR})$, equals the pattern speed of the spiral) can experience a finite change in orbital angular momentum with negligible accompanying increase in random motions.

The change in orbital angular momentum corresponds to a change in guiding center radius. As proposed by Sellwood & Binney (2002), such radial excursions induced through "resonant scattering" across corotation by a *transient* spiral could be permanent, leading to "radial migration", whereby stars move radially within the disk without experiencing a significant change in their orbital circularity, i.e. the stellar disk remains kinematically cold. Note this restricted application of the term "radial migration", excludes a change of guiding center radius that is associated with heating; there is no consensus on the usage of this term in the literature, but was named "churning" by Schönrich & Binney (2009a).

The importance of radial migration to galaxy evolution depends on both the duty cycle for transient spiral arms and the efficiency of radial migration from each transient spiral arm. Should a disk's history include the occurrence of multiple, transient

spiral arms with a distribution of pattern speeds (and hence a distribution of corotation radii across the extent of the disk), radial mixing of stellar populations - and of gas - due to the induced radial migration could have a substantial impact on the chemical, kinematic and structural evolution of disk galaxies (e.g. Sellwood & Binney, 2002; Debattista et al., 2006; Sellwood, 2014a). However, the physical parameters that determine the efficiency of radial migration, and therefore its importance to galaxy evolution, have not yet been rigorously explored.

1.2 Theoretical Exploration

Schönrich & Binney (2009a,b) pioneered an exploration of how radial migration could affect disk evolution by including a prescription for the probability of radial migration within a chemical evolution model for a spiral galaxy. In their model they assumed disks of gas and stars with fixed exponential scale lengths and derived an expression for the probability for radial migration of stars and gas for a given annulus of the disk that scaled simply with the surface mass density of that annulus. This probability was independent of the properties of the spiral perturbations or of the stellar populations.[1] Schönrich & Binney assumed that the vertical energy of a migrating stellar population (characterized by the vertical velocity dispersion, σ_z) is conserved. Their model led to the emergence of a stellar thick disk-like structure

[1]Their expression for the probability of radial migration was based on a dimensional argument considering a random walk within a self-gravitating disk.

as stars that migrated outward from the inner regions of the disk, where velocity dispersions are higher, experienced a weaker vertical restoring force from the lower surface-density outer disk.

In a 3D N-body simulation, Solway, Sellwood, & Schönrich (2012) found that it is not the vertical energy of a population that is conserved but rather the vertical action and that outwardly migrating stars do not thicken the disk enough to produce a thick disk-like structure. Assuming the conservation of vertical action in a self gravitating exponential disk, Minchev et al. (2012) showed analytically that the vertical velocity dispersion (σ_z) for a population of migrating stars decreases exponentially with radius as the square root of the disk surface density, though not as rapidly as the underlying, non-migrating population.

One might appeal to high-resolution N-body/SPH simulations for clarification on how radial migration could affect disk evolution. However, such simulations published to date show evidence for varying degrees of importance for radial migration, ranging from negligible to significant. Bird, Kazantzidis, & Weinberg (2012) performed a comparative analysis of a suite of simulations of disk galaxies evolved over 2.5 Gyr with various initial conditions. They concluded that in the absence of satellite bombardment (which imparts changes in orbital angular momentum as well as vertical energy), the number and strength of transient spiral arms is correlated with greater changes in orbital radii, but appears to have little effect on the vertical distribution

of stars. In a separate suite of fully cosmological simulations[2] that follow the evolution of galaxies over $\sim$ 10 Gyr, radial migration appears to be much more efficient and is arguably responsible for the formation of a dual radial exponential surface density profile (i.e. an outer disk, Roškar et al., 2008) and a thick disk-like structure (Loebman et al., 2011). While these ideas are exciting, it should be noted that formation mechanisms other than radial migration have been proposed for both outer disks (e.g. Elmegreen & Hunter, 2006; Peñarrubia et al., 2006) and thick disks (e.g. Jones & Wyse, 1983; Abadi et al., 2003; Brook et al., 2004; Hayashi & Chiba, 2006; Wyse et al., 2006; Villalobos & Helmi, 2008).

Chemical abundances could provide a means to probe the past importance of radial migration. In the classical "closed-box" (i.e. isolated) model of galactic chemical evolution (Schmidt, 1963; Searle & Sargent, 1972), lower metallicities[3] are predicted in older stars because a well mixed ISM is steadily enriched with time. Stars formed after the initial onset of star formation (SF) are expected to be α-enhanced[4] since they formed from gas that has predominantly been enriched by Type II SNe (Matteucci & Francois, 1989; Gilmore & Wyse, 1991).[5] Generations of stars that form $\gtrsim 10^8 - 10^9$ yrs after the onset of SF have lower [α/Fe] ratios as these stars form from an ISM that has been steadily enriched by Type Ia SNe ejecta. Assuming that

[2]Galaxies in these simulations are "fully cosmological" in the sense that they form from collapsing gas inside a live dark matter halo.

[3]Metallicity is defined to mean the abundance of chemical elements heavier than helium.

[4]A star that is α-enhanced has a ratio of α-elements such as Mg, Si, Ca, and Ti to iron that is high compared to solar abundance ratios, denoted [α/Fe].

[5]The ejecta from Type II SNe have a high [α/Fe] ratio, whereas the [α/Fe] ratio for ejecta from Type Ia SNe is low because they are relatively iron rich.

the annular star formation rate (SFR) is a function of gas surface density (Schmidt, 1959; Wyse & Silk, 1989), the central regions of an exponential disk will have rapidly converted gas into stars, while the outer regions of the disk will have maintained a lower SFR. In this manner, the closed-box model predicts that the disk builds from the inside-out. Consequently, stars of a given age should be more metal rich toward the galactic center, the outer disk should be populated by relatively younger, metal-poor stars, and the oldest stars at a given radius should be [α/Fe] rich.

Schönrich & Binney (2009a,b) included a chemical evolution prescription in their semi-analytic model where SF depends on the surface density of cold gas (as does the closed-box model), but they included gas infall and flows to maintain the disk scale lengths (for the gas and stellar components). Outwardly migrating stars gradually thickened the disk, where the oldest stars (α-rich and metal poor) had the most time to migrate and thus composed the thickest component of the disk. Consequently, the radial migration scenario for thick disk formation (Schönrich & Binney, 2009a,b; Loebman et al., 2011) predicts that in the solar neighborhood there should be a positive vertical *gradient* in age and [α/Fe] abundances, and a negative vertical gradient in [Fe/H] abundances. This picture does not support two distinct disks (thick and thin).

Recent theoretical work favors a scenario where the disk(s) primarily forms from the inside-out, but includes satellite bombardment, gas flows in the disk and gas infall (Bird et al., 2013; Minchev et al., 2013, 2015). In this revised picture, heavy

satellite bombardment (taking elements from the models proposed by Abadi et al., 2003; Brook et al., 2004; Villalobos & Helmi, 2008; Kazantzidis et al., 2008) perturbs the disk at early times. These older populations of stars, therefore, have higher velocity dispersions, shorter scale-lengths, and longer scale-heights. At later times, when the merger history is relatively quiescent (in this model), forming stars maintain a lower velocity dispersion (because they are not perturbed by satellites) and their evolution is dominated by secular processes, like scattering and radial migration. Simulations rely on star particle ages and birth radii since sub-grid chemical evolution and SF models remain controversial. It is therefore difficult to make strong predictions for the observed chemical abundance patterns from the simulated data.

The origin of the range in the inferred importance for radial migration to disk evolution is poorly understood, in large part because of the many parameters in the simulations and the fact that it is unknown what physical parameters underlie the efficiency of radial migration. Thus, it is uncertain how time- and mass-resolution, integration time, the presence or not of a live, dark-matter halo, the initial conditions and assumed sub-grid physics may affect the evolution of simulated disks in this respect (see also Sellwood, 2014a). As a result, it is unclear how the efficiency of radial migration in these simulations relates (or not) to that of real disk galaxies.

1.3 Observational Signatures

In principle, there should be observable signatures of the past importance of radial migration in the properties of solar neighborhood stars. In practice, however, observational uncertainties currently make it difficult to determine the amplitude (if any) of such signatures.

It is well established that stellar orbits evolve as stars interact with fluctuations in the underlying galactic potential (like GMCs Chandrasekhar, 1943). These scattering processes[6] can permanently change the mean orbital radius, R_L, of a star (and thus its orbital angular momentum via $L_z \propto R_L\, v_c(R_L)$) while simultaneously increasing the amplitude of radial excursions from R_L (related to an increase in random orbital energy, E_{ran}, and orbital eccentricity). The velocity dispersion of an ensemble of stars will therefore increase over time (Spitzer & Schwarzschild, 1953; Barbanis & Woltjer, 1967; Wielen, 1977; Lacey, 1984; Carlberg & Sellwood, 1985; Fuchs, 2001; De Simone et al., 2004). A sample of the solar neighborhood stars will inevitably be contaminated by stars that have distant birth radii, an effect that will be more exaggerated for older stars. Given that the velocity dispersion has a measurable (e.g. Nordström et al., 2004) and possibly predictable (eg. Spitzer & Schwarzschild, 1953; Carlberg & Sellwood, 1985) growth rate, one can assume a prescription for the

[6]It should be understood that our use of the term "scattering" is distinct from the term "resonant scattering" used by Sellwood & Binney (2002) in reference to the changes in orbital angular momentum at corotation with no associated heating. It is also distinct from the redirection of random motions without heating as is expected from interactions with corotating GMCs (Spitzer & Schwarzschild, 1953; Lacey, 1984; Sellwood, 2014a) or transient spirals (Carlberg & Sellwood, 1985).

expected radial excursions of stars for a given velocity dispersion to place a time dependent upper limit on the expected degree of contamination to the local stellar population (eg. Wielen et al., 1996; Schönrich & Binney, 2009a; Hayden et al., 2015).

In the paradigm of a closed-box model, it is not clear that the chemical abundance patterns in the the local stellar population can be completely explained by contamination by stars on non-circular orbits that were born at distant galactocentric radii. Should radial migration be an efficient process, a sampling of stars with a mean orbital radius near solar would include stars that have significantly different radii. This could give rise to a scatter in stellar metallicity in the solar neighborhood as a function of age (i.e. a scatter in the age metallicity relationship - AMR) beyond what is expected from scattering processes (Wielen et al., 1996).

To what degree the AMR necessitates radial migration has been somewhat controversial. The Geneva-Copenhagen Survey (GCS) (Nordström et al., 2004; Holmberg et al., 2009) found a scatter in metallicity of σ[Fe/H]$\sim$0.2 in the local stellar population, with little to no age dependence. Casagrande et al. (2011) performed a careful recalibration of the GCS temperature scale and found an intrinsic spread of $\sim$0.1 dex in the [Fe/H] ratio and $\sim$ 1 Gyr uncertainty in their sample of stars with "well-determined" ages. Indeed, the large uncertainty inherently associated with stellar age determination gives rise to significant difficultly in making strong conclusions about age dependent trends in stellar properties. As such, although Casagrande et al. do see an increase in the scatter of metallicity with age, they are unable to determine if the

trend can be completely explained by the age dependent velocity dispersion or if it requires a further mechanism such as radial migration. In an effort to lower the internal random error in individual stellar properties (including metallicity), Burnett et al. (2011) used a Bayesian method developed by Burnett & Binney (2010) to analyze data from the RAVE (Radial Velocity Experiment) survey (Steinmetz et al., 2006). They found a FWHM spread of [M/H] in thin disk stars (z$<$ 300 pc) of all ages to be ~ 0.15 dex where the median individual internal error was 0.17 dex, implying a very narrow distribution in thin disk metallicities. Hayden et al. (2015) independently confirm the trends in the chemical abundances of solar neighborhood stars found by Casagrande et al. (2011) and Burnett et al. (2011) using APOGEE/SDSS-III Data Release 12 data. Nonetheless, Kordopatis et al. (2015) recalibrated the metallicities of the RAVE DR4 data and found that the solar neighborhood has a significant contribution of low eccentricity ($e \leq 0.15$) stars with super-solar metallicities, consistent with radial migration from the inner disk.

Should radial migration be responsible for forming the thick disk (Schönrich & Binney, 2009a,b; Loebman et al., 2011), it is expected that there should be a vertical metallicity gradient (see §1.2). Observational data support a vertical metallicity gradient (Ivezić et al., 2008; Bond et al., 2010; Kordopatis et al., 2011; Katz et al., 2011; Ruchti et al., 2011; Bovy et al., 2012b), but whether this is an intrinsic property of the thick disk (Ivezić et al., 2008; Bond et al., 2010; Bovy et al., 2012a) or the result of integrating over the smooth transition between disk and halo components

(Katz et al., 2011; Kordopatis et al., 2011) is a matter of debate.

Hayden et al. (2015) probe the chemical properties of stars across the MW disk, not just in the solar neighborhood, and find that the skew in the metallicity distribution function is a function of galactocentric radius. They are only able to fit the skew in the metallicity distributions for the outer disk when they include radial migration in their models.[7] They find two distinct sequences in [α/Fe]-[Fe/H] space, which is not in good agreement with the disk formation model presented by Schönrich & Binney (2009b)[8] and Loebman et al. (2011).

Wielen et al. (1996) used chemical abundances as a tracer for the radial migration of the Sun. They found the solar metallicity to be higher than that of the averaged local, solar aged F- and G-type stars by $+0.17 \pm 0.04$ dex. Wielen et al. (1996) adopted a radial gradient in [Fe/H] (they used ∂[Fe/H]/∂R found in thin disk open clusters by Friel & Janes (1993)) and assumed it has not changed in the lifetime of the Sun. They concluded that the Sun originated $\sim$ 2 kpc closer to the galactic center than our current position. This study has been used to support the possibility that radial migration may play a large role not only in the distribution of stars in the MW, but in our own origins. However, since both Casagrande et al. (2011) and Burnett et al. (2011) found that all stars in the solar neighborhood show a peak nearly *at* solar abundance, making the Sun a typical solar neighborhood star rather than

[7]Hayden et al. (2015) use a simple diffusion of guiding center radii for their model for the probability of radial migration.

[8]Schönrich & Binney (2009b) found that a thickened disk that formed via radial migration, rather than distinct thick and thin disk components, had a continuous distribution in [α/Fe]-[Fe/H] space.

an exception, the data suggest that radial migration is not important to the Sun's history.[9]

Observational data suggest that radial migration may play a role in the evolution of the MW, particularly in the outer disk at later times (see Kordopatis et al., 2015; Hayden et al., 2015). Nonetheless, uncertainties in the observational data make it difficult determine whether or not radial migration is necessary to explain trends in solar neighborhood metallicity distributions (Wielen et al., 1996; Casagrande et al., 2011; Burnett et al., 2011).

1.4 Motivation for Analytic Work

Analytical arguments offer an alternate means to gain insight into the physical parameters important to the efficiency of radial migration. The published analytic derivations of the requirements for radial migration offer limited insight because they are applicable only to stars on purely or nearly circular orbits (Contopoulos, 1978; Binney & Tremaine, 1987; Sellwood & Binney, 2002). It is generally expected that the effectiveness of radial migration must decrease with increasingly non-circular orbits, since stars in non-circular orbits cannot keep station with the perturbing pattern speed (Sellwood & Binney, 2002). Indeed, Solway et al. (2012) found a decrease in the RMS change in the orbital angular momenta of a population of star particles in

[9]In contrast, Martínez-Barbosa et al. (2015) do a statistical analysis of solar neighborhood dynamics to find that the Sun likely did not migrate.

the presence of a transient spiral, as the value of the radial velocity dispersion (σ_R) of the population increased (see their Figure 10). In a separate N-body simulation of a sub-maximal disk, Vera-Ciro et al. (2014) found that radial migration preferentially affected stellar populations with low vertical velocity dispersion. The impact of spiral strength, lifetime, and pitch angle on the efficiency of radial migration remains largely unexplored (but will be addressed in this study).

This study is intended to identify the important factors contributing to the efficiency of stellar radial migration and to determine simple scaling relations which can be implemented within models of disk evolution. It should be noted that gas is also affected at the corotation resonance, but we do not address the migration of gas or, indeed, any dissipative physics here. Our analysis of the efficiency of radial migration is simplified to only include stellar radial migration that is induced by a single spiral pattern in a 2D disk. We use the following three measures of the efficiency of radial migration: (1) the fraction and distribution of disk stars captured in trapped orbits; (2) the RMS change in orbital angular momentum of migrating stars; and (3) the time-scale to reach the maximum value of the RMS change in orbital angular momentum for the ensemble of migrating stars. In Chapter 2, we review the underlying physics for radial migration. In Chapter 3, we give the model parameters, underlying potential and distribution functions assumed throughout this work. In Chapter 4, we derive an analytic criterion to determine whether or not a star with some finite random orbital energy is captured in a trapped orbit. In Chapter 5, we explore the

parameters important to the amplitude of radial excursions of stars in trapped orbits, a component to understanding measure (2). Chapter 6 focuses on measure (1) by applying the capture criterion to models of stellar populations with a given distribution function in a disk galaxy. In Chapter 7, we discuss our conclusions and in Chapter 8 we give an outline for future work toward understanding the efficiency of radial migration in spiral galaxies.

Chapter 2

Underlying Physics for Radial Migration

2.1 Definition of a Trapped Orbit

The first step of the process that can lead to radial migration is for an object (star, asteroid, planet, etc.) to be captured onto a particular family of resonant orbits that can occur near the radius of corotation with a non-axisymmetric potential. Members of this family of orbits are uniquely characterized by periodic changes in orbital angular momentum with negligible accompanying change in random orbital energy. A star on an orbit that is a member of this family will henceforth be referred to as being in a "trapped" orbit (the name proposed by Barbanis, 1976). Trapped orbits were predicted as a solution to the three-body problem for an asteroid in the

orbital path of Jupiter around the Sun (Brown, 1911), and were dubbed "tadpole" or "horseshoe" orbits, because these approximate the shape of the orbital path in the rotating frame (see Goldreich & Tremaine, 1982, for a discussion of these orbits in planetary systems). The shapes of stellar orbital paths about the galactic center in the presence of a spiral or bar perturbation are slightly different, but the physics is the same (see below).

2.2 Underlying Physics

In order to understand the periodic changes in orbital angular momentum of a star in a trapped orbit, it is instructive to restrict the analysis to an initially circular orbit in a 2D disk with a flat rotation curve. In this case the star's initial orbital radius, R, equals its guiding center radius, R_g, and its azimuthal velocity, v_ϕ, equals the circular velocity, v_c. Assume that a steady m-armed perturbation to the potential is imposed, with pattern speed $\Omega_p = v_c/R_{CR}$ and that the star is located close to the radius of corotation, R_{CR}. Further, assume that the strength of the perturbation is approximately constant across corotation. The net force on the star, in the frame that rotates with the pattern is then predominantly in the azimuthal direction ($\mathbf{F} \approx F_\phi \hat{\boldsymbol{\phi}}$). The resulting torque ($\boldsymbol{\tau} = d\mathbf{L_z}/dt \propto R_{CR} F_\phi \hat{\mathbf{z}}$) will alter the star's z-directional angular momentum (L_z), which results in a change in the star's orbital radius. The time-dependent torque a star experiences during a trapped orbit

(see the physical explanation in Sellwood & Binney, 2002, §3.4) will cause the star's guiding center to oscillate radially. Should the perturbation be transient, the star will likely not complete this oscillation, its orbital angular momentum and guiding center radius will then be permanently changed (Sellwood & Binney, 2002) and the star will have migrated radially.

The analysis of orbits in a steadily rotating, non-axisymmetric disk is most conveniently carried out in the frame rotating with the pattern. As discussed in standard textbooks e.g. Binney & Tremaine (2008), in such a potential neither energy nor angular momentum (measured in the non-rotating frame) is conserved, and consequently, there are no circular orbits in a non-axisymmetric potential. A combination of orbital energy in the inertial frame, E, and orbital angular momentum (L_z) is given by the Jacobi integral, E_J, where the E_J is the Hamiltonian in a time-independent, non-axisymmetric potential. Hence E_J is conserved only in the rotating frame and is given by (Binney & Tremaine, 2008, equations 3.113)

$$E_J = E - \Omega_p L_z = \frac{1}{2}|\dot{\mathbf{x}}|^2 + \Phi_{eff}(\mathbf{x}), \tag{2.1}$$

with

$$\Phi_{eff}(\mathbf{x}) \equiv \Phi(\mathbf{x}) - \frac{1}{2}|\mathbf{\Omega_p} \times \mathbf{x}|^2 \tag{2.2}$$

being the effective potential (Binney & Tremaine, 2008, equations 3.114), $\Phi(\mathbf{x})$ the actual potential, and $\mathbf{x}$ and $\dot{\mathbf{x}}$ being, respectively, the position and velocity of the star

in the rotating frame. It is evident that a star with a given value of E_J will have zero velocity at locations where $\Phi_{eff}(R, \phi) = E_J$, and thus the contour of Φ_{eff} with this value traces the Zero Velocity Curve (ZVC) for such stars.

Figure 2.1 shows an example of contours of $\Phi_{eff}(\mathbf{x})$ near the radius of corotation of a $m = 4$ armed spiral pattern superposed on an underlying logarithmic potential (we describe our model in detail in §3). The parameters are chosen such that for the spiral $R_{CR} = 10$ kpc, pitch angle $\theta = 35^\circ$ (measured from the line of azimuth, such that spirals with small θ are ring-like), amplitude at corotation $|\Phi_s(R_{CR})| = 322$ km^2 s^{-2}, and with circular speed in the underlying potential $v_c = 220$ km s^{-1}. The zero of the azimuthal coordinate, ϕ, is taken to be halfway between the maxima of the spiral pattern and in the figure is along the direction of the positive x-axis, and ϕ increases in a counter-clockwise direction. There exist $m = 4$ local maxima in the effective potential at $R = R_{CR}$ and with azimuthal coordinates located at the mid-points between the spiral arms, i.e. at $\phi = \{0, \pi/2, \pi, 3\pi/2\}$.[1] There also exist $m = 4$ local minima (saddle points) in the effective potential at R_{CR} and $\phi = \{\pi/4, 3\pi/4, 5\pi/4, 7\pi/4\}$, at the peak of the spiral potential. We define ϕ_{max} and ϕ_{min} to be the azimuthal coordinates of the maximum and minimum of the effective potential nearest the star to be considered, respectively.

As may be seen in Figure 2.1, the local maxima in the effective potential are surrounded by contours in the effective potential that encircle these maxima, rather

[1] These local maxima correspond to the Lagrange points L_4 and L_5 in the three-body problem.

than encircling the galactic center. The solid, black boundary of the grey shaded region in Figure 2.1 is where the Jacobi integral of a star with zero random energy in the inertial frame will be equal to the value of the effective potential at the local minima at the radius of corotation, and very nearly follows the closed contours of the effective potential that encircle the local maxima. The shaded region will henceforth be called the "capture region" for reasons that will become apparent in §4.1.1. The areas enclosed by the contours around the maxima in the effective potential and of the capture region are larger for higher amplitude spiral patterns (we explore this in Chapter 5); note that we have chosen a high-amplitude spiral for the purpose of illustration.

Sellwood & Binney (2002) (their equations 1-4) used the conservation of E_J (equation 2.1 for a star moving in a 2D non-axisymmetric potential to derive the relationship, in the epicyclic approximation, between the change in a star's orbital random energy, expressed in terms of the radial action, J_R, and the change in its orbital angular momentum. They found that

$$\Delta J_R = \frac{\Delta E_{ran}}{\kappa} = \frac{(\Omega_p - \Omega_g)}{\kappa} \Delta L_z, \tag{2.3}$$

where κ is the epicyclic frequency of radial oscillations for a star with small excursions

from a circular orbit (Binney & Tremaine, 2008, equation 3.80),

$$\kappa^2(R_L) = \left(R\frac{d\Omega_c^2}{dR} + 4\Omega_c^2 \right)_{R_L}, \tag{2.4}$$

with guiding center radius given by

$$R_L = R\left(\frac{v_\phi}{v_c}\right), \tag{2.5}$$

where v_ϕ is the instantaneous azimuthal velocity of the star in the inertial frame. The random orbital energy in the inertial frame,

$$E_{ran} = E_* - E_c(R_L), \tag{2.6}$$

is evaluated in the underlying axisymmetric potential, where E_* is the total stellar energy in the inertial frame, and $E_c(R_L)$ is the energy of a star in a circular orbit at R_L (Dehnen, 1999a).

In Figure 2.2, we show a Lindblad diagram similar to Figure 1 from Sellwood & Binney (2002) to illustrate how changes in orbital angular momentum relate to changes in orbital energy (equation 2.3) through the Jacobi integral (equation 2.1). Circular orbits lie along the solid curve. Orbits are therefore restricted to the unshaded region in the upper, left-hand side of the diagram. The Jacobi integral for a star (E_J) is conserved along lines with slope equal to the pattern speed, Ω_p. Note that at corotation

($\Omega_g = \Omega_p$), changes in orbital angular momentum are not accompanied by changes in random energy.

The orbital path of a star with nearly zero random orbital energy that is captured in a trapped orbit is visualized in Figure 2.1. The star has initial position 1.1 kpc beyond corotation (causing it to lag the pattern in the rotating frame), mid-way between trailing spiral arms, which places it inside the capture region at $t = 0$. The trajectory of the star is plotted in rainbow colors, beginning with red and ending with violet. The star has a low value of the initial velocity in the rotating frame and since $\Omega_g \approx \Omega_p$, little increase in random motions (see equation 2.3). The star therefore remains on a trajectory that closely follows its ZVC, the contour for $\Phi_{eff}(\mathbf{x}) = E_J$ (dashed contour in Figure 2.1). Note that the star sensibly does not cross into the forbidden region where $\Phi_{eff}(\mathbf{x}) > E_J$.

Any star on an orbit with Jacobi integral less than the value of the effective potential at the local saddle point (the lowest value of the effective potential within the shaded grey area in Figure 2.1) i.e. $E_J < \Phi_{eff}(R_{CR}, \phi_{min})$, will not be able to cross the corotation radius and will therefore not be able to oscillate around the local maximum in Φ_{eff}, i.e. is not trapped and will instead have an orbital path in the rotating frame that encircles the galactic center.

In contrast, a star with $E_J > \Phi_{eff}(R_{CR}, \phi_{min})$ can cross the corotation radius. Should such a star have zero random orbital energy in the inertial frame, i.e. the orbital energy of a star in circular orbit in the underlying axisymmetric potential at

that radius, it would have coordinates that are inside the capture region (shown in the next section). Its orbital path would closely follow a contour in $\Phi_{eff}(\mathbf{x})$ that encloses a local maximum, as shown in Figure 2.1.[2]

[2]In the special case that a star with zero random energy has $E_J = \Phi_{eff}(R_{CR}, \phi_{min})$, it can cross R_{CR} and may be in a heteroclinic orbit (e.g Martinet, 1974).

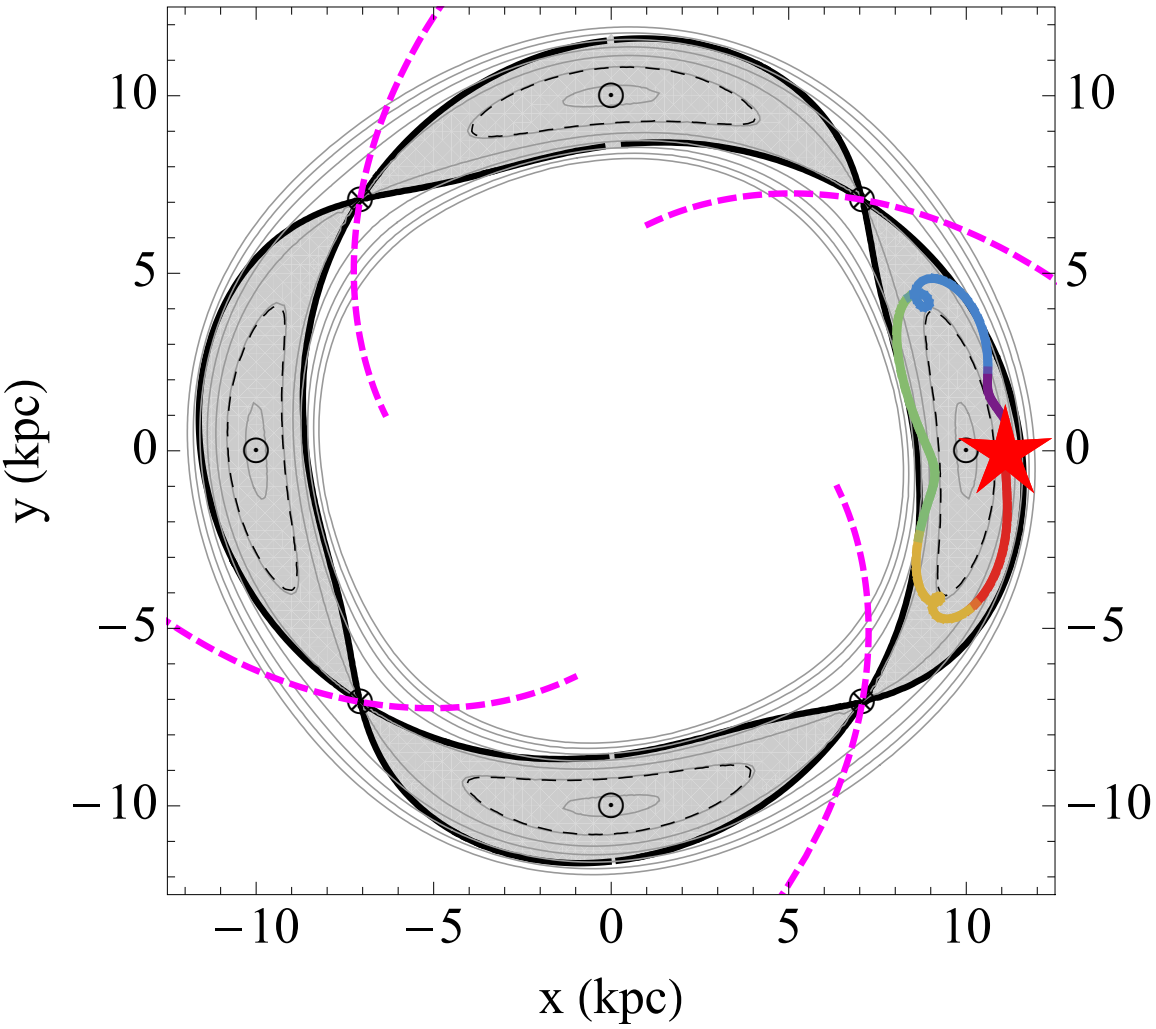

Figure 2.1: Effective potential, Φ_{eff}, for a trailing, $m = 4$ spiral pattern with pitch angle $\theta = 35°$, $R_{CR} = 10$ kpc and amplitude at corotation $|\Phi_s(R_{CR})| = 322$ km^2 s^{-2} superposed on an underlying logarithmic potential with $v_c = 220$ km s^{-1}. The peak of the spiral perturbation is shown as thick, dashed magenta curves. The local maxima in Φ_{eff} (between spiral arms) are marked with the symbol $\odot$ and the saddle points (the deepest part of the spiral potential at corotation) are marked with $\otimes$. The capture region has a thick, black outline and is shaded grey. The orbital path in the rotating frame of a captured star (shown in solid rainbow colors that begin red and end violet) that was launched with $(v_R, v_\phi) = (0, 220)$ km s^{-1} in the inertial frame with initial position 1.1 kpc outside corotation and $\phi = 0$ (marked with a red star) was followed for 1 Gyr. The ZVC for the star, where $\Phi_{eff}(R, \phi) = E_J$, are indicated by the dashed line.

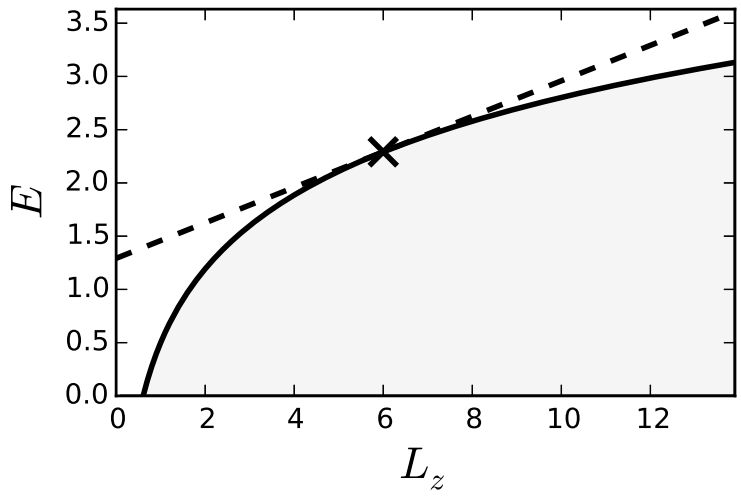

Figure 2.2: Lindblad diagram similar to Figure 1 from Sellwood & Binney (2002) illustrating how changes in orbital angular momentum relate to changes in orbital energy via the Jacobi integral. The solid, black curve represents circular orbits, the shaded region is inaccessible since an orbit cannot have energy less that circular. Vertical distance from the solid curve represents random orbital energy. The 'X' marks the radius of corotation and the dashed line has slope equal to the pattern speed (Ω_p) of the spiral pattern. Since the Jacobi integral is conserved along lines with slope Ω_p, stars near corotation that have changes in orbital angular momentum will have little to no changes in random energy. For illustrative purposes this diagram uses units where $v_c = L_z/R = 1$.

Chapter 3

The Model

In this section we describe our approach and models for the disk and stellar populations that will be used throughout this work. Unless otherwise stated, we use the values given in Table 3.1 when quantitative calculations are required.

Table 3.1: Adopted parameter values when a quantitative analysis is required, unless otherwise stated.

Parameter	Symbol	Value
Circular velocity	v_c	220 km s^{-1}
Scale length for underlying potential	R_p	1 kpc
Radius of corotation	R_{CR}	8 kpc
Number of spiral arms	m	4
Spiral pitch angle	θ	25°
Fractional amplitude of spiral surface density	ϵ_Σ	0.3
Surface density normalization	$\Sigma(R = 8 \text{ kpc})$	50 $M_\odot$ pc^{-2}
Scale length for surface density	R_d	2.5 kpc
Radial size of an annulus	dR	0.1 kpc

3.1 Model for the Disk Potential

We assume a 2D disk potential, $\Phi(R, \phi)$, in cylindrical coordinates, resulting from an underlying axisymmetric potential, $\Phi_0(R)$, plus a spiral perturbation, $\Phi_1(R, \phi, t)$. The axisymmetric potential that gives rise to a flat rotation curve,

$$\Phi_0(R) = v_c^2 \ln(R/R_p), \tag{3.1}$$

where v_c is the circular velocity and R_p is the characteristic scale length of the potential. We superpose an m-armed spiral density wave (Lin & Shu, 1964; Lin et al., 1969; Binney & Tremaine, 2008) given by

$$\Phi_1(R, \phi) = |\Phi_s(R)| \cos[m \cot\theta \ln(R/R_{CR}) + m(\Omega_p t - \phi)], \tag{3.2}$$

which in the frame that rotates with the spiral pattern speed, Ω_p, is

$$\Phi_1(R, \phi) = |\Phi_s(R)| \cos[m \cot\theta \ln(R/R_{CR}) - m\,\phi]. \tag{3.3}$$

Here $R_{CR} = v_c/\Omega_p$ is the radius of corotation and θ is the pitch angle of the spiral arm (measured counter-clockwise from a line of constant azimuth). The amplitude of the spiral potential is given by

$$\Phi_s(R) = \frac{2\pi G \Sigma(R) \epsilon_\Sigma}{k(R)}, \tag{3.4}$$

where $\Sigma(R)$ is the surface density of the disk, ϵ_Σ is the fractional amplitude in surface density of the spiral pattern, and $k(R)$ is the radial wave-number of the spiral pattern. The radial wave number is

$$k(R) = \frac{m}{R \tan\theta}. \tag{3.5}$$

We assume that the spiral may be modeled as a density wave for two reasons; the pattern speed is invariant with radius and its form is analytic.

3.2 Models for the Kinematics of the Disk

In conjunction with the potential, Φ, the phase space distribution function, $f(\mathbf{x}, \mathbf{v})$, and its moments determine the dynamical properties of a stellar population. In order to explore the parameters important to determining the spatial distribution of stars in trapped orbits, we use two prescriptions for the distribution function in this work.

3.2.1 Gaussian Velocity Distribution

The 4D phase space distribution function for a 2D disk has the form (the 6D form is given by Binney & Tremaine, 2008, equation 4.22),

$$f(\mathbf{x}, \mathbf{v}) = \Sigma(\mathbf{x})\, f(\mathbf{v})_{\mathbf{x}}, \tag{3.6}$$

where $f(\mathbf{v})_{\mathbf{x}}$ is the velocity distribution function at coordinate $\mathbf{x}$ and $\Sigma(\mathbf{x})$ is the surface density of the disk.

We model the velocity distribution function using a 2D Gaussian velocity distribution, $f_G(\mathbf{v})_{\mathbf{x}}$. The velocity and random velocity, $\mathbf{v}_{ran}$, are defined in the inertial frame and are related by,

$$\begin{aligned} \mathbf{v} &= v_R\hat{\mathbf{R}} + v_\phi\hat{\boldsymbol{\phi}} \\ &= v_{ran,R}\hat{\mathbf{R}} + (v_c + v_{ran,\phi})\hat{\boldsymbol{\phi}} \\ &= \mathbf{v}_{ran} + \mathbf{v}_c. \end{aligned} \tag{3.7}$$

The radial velocity distribution is centered on $\langle v_{ran,R}\rangle = 0$ with standard deviation given by the assumed radial velocity dispersion, σ_R, at that the coordinate of evaluation ($\mathbf{x}$). The azimuthal velocity distribution is centered at $v_c + \langle v_{ran,\phi}\rangle = v_c - v_a$ (we discuss this offset of the centroid toward slower rotation, due to a simple model for asymmetric drift, in §6.2). In order to determine the distribution of azimuthal velocities we adopt solar neighborhood values for the ratio of azimuthal to radial velocity dispersions (Nordström et al., 2004),[1]

$$\sigma_\phi/\sigma_R = 0.63 \tag{3.8}$$

[1]One can also derive this ratio for a flat rotation curve using the Oort constants (Binney & Tremaine, 2008, equation 3.100), which gives $\sigma_\phi/\sigma_R = 0.71$.

and (Dehnen & Binney, 1998)

$$v_a = \sigma_R^2/(80\,\mathrm{km\,s^{-1}}). \tag{3.9}$$

By using constant ratio, σ_ϕ/σ_R, we assume that the shape of the velocity ellipsoid is the same everywhere. The 2D probability distribution for velocity at a given spatial coordinate is,

$$\begin{aligned} f_G(\mathbf{v})_\mathbf{x} &= \frac{1}{2\pi\sigma_R\sigma_\phi}\exp\left\{-\frac{(v_R-\langle v_R\rangle)^2}{2\sigma_R^2}-\frac{(v_\phi-\langle v_\phi\rangle)^2}{2\sigma_\phi^2}\right\} \\ &= \frac{0.63}{2\pi\sigma_R^2}\exp\left\{-\frac{v_{ran,R}^2}{2\sigma_R^2}-\frac{(v_c+v_{ran,\phi}+\sigma_R^2/(80\,\mathrm{km\,s^{-1}}))^2}{2(0.63\sigma_R)^2}\right\}. \end{aligned} \tag{3.10}$$

This prescription defines the velocity distribution as a function of σ_R only, since we have assumed $\sigma_\phi = \sigma_\phi(\sigma_R)$ and $v_a = v_a(\sigma_R)$. At any spatial position in the disk the shape of velocity distribution ($f_G(\mathbf{v})_\mathbf{x}$), the distribution of orbital angular momentum and orbital energy, and thus the fraction of stars in trapped orbits, is entirely dependent on the radial velocity dispersion (σ_R).

Our chosen prescription, $f_G(\mathbf{x},\mathbf{v})$, is a close approximation to the Schwarzchild distribution function (Binney & Tremaine, 2008, equation 4.156) for a 3D disk in the 2D plane. We here impose a prescription for the lag in azimuthal velocity in the 2D disk that is dependent on the radial velocity dispersion rather than derive it from first principles. The advantage to our choice of distribution function (f_G) is that we are able to isolate how asymmetric drift affects the fraction and spatial distribution

of trapped stars (see §6.2). Under the assumption of an exponential disk and a given radial velocity dispersion, the normalized integral of the Schwarzchild distribution function over coordinate space and radial velocity produces an azimuthal velocity distribution that well describes that of the solar neighborhood (Nordström et al., 2004) (for further details see Binney & Tremaine, 2008, Figure 4.17). We therefore impose an exponential surface density profile for the stellar disk,

$$\Sigma(R) = \Sigma_0 e^{-R/R_d}, \tag{3.11}$$

with radial scale length R_d.

The full Gaussian distribution function we use in this study has the form

$$\begin{aligned} f_G(\mathbf{x},\mathbf{v}) &= \Sigma(\mathbf{x})\, f_G(\mathbf{v})_{\mathbf{x}} \\ &= \Sigma_0 e^{-R/R_d}\, \frac{0.63}{2\pi\sigma_R^2} \exp\left\{ -\frac{v_{ran,R}^2}{2\sigma_R^2} - \frac{(v_c + v_{ran,\phi} + \sigma_R^2/(80\,\mathrm{km\,s^{-1}}))^2}{2(0.63\sigma_R)^2} \right\}. \end{aligned} \tag{3.12}$$

Models that adopt a Gaussian velocity distribution cannot include the skew in the observed azimuthal velocity distribution. The azimuthal velocity distribution at a given radius is directly related to the orbital angular momentum distribution at that radius through the relation $L_z \propto R\, v_\phi$. We are therefore implicitly modeling the orbital angular momentum distribution in the disk. In Chapter 4, we show that orbital angular momentum is the most important parameter for determining whether or not a star is in a trapped orbit. Therefore the predictive power of these models

is limited insofar as it holds true that the fraction of stars in trapped orbits depends more on the shift of the peak of the azimuthal velocity distribution and than on its low velocity tail.

The reader should note that stellar populations with different values for σ_R will also have different orbital angular momentum distributions. We discuss this last point in more detail in §6.3.2.

3.2.2 Distribution Function for a Warm Disk

We use the following expression for the distribution function for a dynamically warm disk, f_{new} (Dehnen, 1999b),

$$f_{new}(E, L_z) = \frac{\Sigma(R_E)}{\sqrt{2}\pi\sigma_R^2(R_E)} \exp\left\{\frac{\Omega(R_E)[L_z - L_c(R_E)]}{\sigma_R^2(R_E)}\right\}, \tag{3.13}$$

where L_z represents orbital angular momentum about the z-axis, E is orbital energy, and Ω is the circular orbital frequency. R_E is the orbital radius or a star at in a circular orbit with energy E is in a circular orbit and $L_c(R)$ is the orbital angular momentum (L_z) of a star in a circular orbit at radius R. In a disk with a flat rotation curve (equation 3.1), a star in a circular orbit has energy

$$E = \frac{1}{2}v_c^2 + v_c^2 \ln(R_E/R_p), \tag{3.14}$$

and thus,

$$R_E = R_p \exp\left\{\frac{E - \frac{v_c^2}{2}}{v_c^2}\right\}. \tag{3.15}$$

This distribution function (f_{new}) is an extension of the Shu distribution function, ${f_S}^2$, for a warm disk (Shu, 1969; Binney, 1987; Dehnen, 1999b) modified to more closely approximate properties of disk populations. Dehnen (1999b) finds that at radii greater than a disk scale length, the surface density generated from f_{new} is well approximated by an exponential surface density profile (equation 3.11).

[2]In these distribution functions (f_S or f_{new}), the radial excursions of stars on non-circular orbits from the inner disk naturally give rise to asymmetric drift and a low velocity tail in the azimuthal velocity distribution (Shu, 1969).

Chapter 4

Analytic Criterion for Capture at Corotation

4.1 Stars with Zero Random Orbital Energy

The criterion for whether or not a star *with zero random energy* in the inertial frame is captured in a trapped orbit (henceforth called the "capture criterion") has been previously explored in the literature (Contopoulos, 1973, 1978; Papayannopoulos, 1979a,b; Sellwood & Binney, 2002; Binney & Tremaine, 2008). For both the reader's convenience and to highlight the physics relevant to this study, we will briefly summarize these analyses, but defer to those papers for a more thorough treatment. The

requirements for a star to be in a trapped (or "horseshoe") orbit that are derived in Binney & Tremaine (1987) (Ch. 3.3b) and discussed in Sellwood & Binney (2002) use a different set of assumptions from the capture criterion outlined in this section. In appendix A, we explore the relationship between these two criteria.[1]

Contopoulos (1978) derived an analytic capture criterion for stars with zero random energy in a 2D disk where the potential, $\Phi(R, \phi)$, was composed of an underlying axisymmetric potential, $\Phi_0(R)$, plus a perturbation, $\Phi_1(R, \phi)$, that varied sinusoidally in the azimuthal direction. In the frame rotating with the pattern, the perturbation to the potential near the radius of corotation is given by:

$$\Phi_1(R, \phi) = |\Phi_s(R)| \cos(m\phi), \tag{4.1}$$

with $|\Phi_s(R)|$ being the amplitude of the potential and m the number of spiral arms.

Contopoulos simplified the equations by introducing the constant quantity denoted here by h_{CR}, being the value of the Jacobi integral for a star in a circular orbit at R_{CR} in the underlying axisymmetric potential. He then used a 2^{nd} order expansion of the Jacobi integral (E_J) of a star near the maximum in Φ_{eff}, at (R_{CR}, ϕ_{max}), in terms of action-angle variables (re-expressed by Papayannopoulos, 1979b, equation 37),

[1]The capture criterion of Binney & Tremaine (1987) emerges from the equations of motion for a star in a trapped orbit. Sellwood & Binney (2002) used the equations of motion from this analysis to approximate the maximum radial excursion during, and the minimum peroid for, a trapped orbit (their equations (11) and (12)).

$$E_J = h_{CR} + \kappa_{CR} J_R + a_{CR} J_R^2 + 2 b_{CR} J_R J_\phi + c_{CR} J_\phi^2 + \Phi_{s,CR} \cos(m\phi_1), \tag{4.2}$$

where the coefficients (Contopoulos, 1975, Appx. A),

$$\begin{aligned} a_{CR} &= \frac{1}{16}\kappa_{CR}^2 \left[\Phi''''_{0,CR} + \frac{60\Phi'_{0,CR}}{R_{CR}^3} - \frac{5}{3\kappa_{CR}^2}\left(\Phi'''_{0,CR} - \frac{12\Phi'_{0,CR}}{R_{CR}^2} \right)^2 \right] \\ b_{CR} &= \frac{\Omega_{CR}\kappa'_{CR}}{R_{CR}\kappa_{CR}^2} \\ c_{CR} &= \frac{\Omega_{CR}\Omega'_{CR}}{R_{CR}\kappa_{CR}^2} \end{aligned} \tag{4.3}$$

where prime indicates the radial derivative, ϕ_1 is the azimuthal angular distance from (R_{CR}, ϕ_{max}) (i.e. $\phi_1 = \phi - \phi_{max}$), $J_\phi = L_z(R) - v_{circ}(R_{CR})R_{CR}$ is the azimuthal action in the rotating frame and the subscript "CR" denotes evaluation at the radius of corotation.

Setting $J_R = 0$ in equation 4.2, as appropriate for a star with zero orbital random energy, yields a simple quadratic equation:

$$J_\phi^2 = \frac{1}{c_{CR}} \left[E_J - h_{CR} - |\Phi_s|_{CR} \cos(m\phi_1) \right]. \tag{4.4}$$

As Contopoulos noted, real solutions (requiring that the right-hand side be greater than zero) exist for all values of the angle ϕ_1 only if $E_J - h_{CR} < -|\Phi_s|_{CR}$ (Contopoulos, 1978, equation 16). Real solutions exist for only a restricted range in ϕ_1 when (see

also Contopoulos, 1978, equation 17)

$$-|\Phi_s|_{CR} < E_J - h_{CR} \leq |\Phi_s|_{CR}. \tag{4.5}$$

Such stars are captured in trapped orbits, oscillating about the maximum in the effective potential (recall that the approximate expression for the Jacobi integral was valid only near the maximum).

Both E_J and h_{CR} are time-independent, so that the quantity,

$$\Lambda_c \equiv \frac{E_J - h_{CR}}{|\Phi_s|_{CR}} \tag{4.6}$$

is also conserved, (where the subscript "c" denotes that the analysis assumes a star on a circular orbit in the underlying axisymmetric potential). Substitution for this parameter reduces the statement of the criterion for a star with zero random orbital energy to be trapped (equation 4.5) to the more compact form:

$$-1 < \Lambda_c \leq 1. \tag{4.7}$$

A star (with zero orbital random energy) that meets the capture criterion - and is therefore in a trapped orbit - could migrate radially if the perturbation were transient. Should the star have random energy, however, equation 4.7 would no longer be a valid criterion to determine whether or not the star is in a trapped orbit. We turn to this

more realistic situation in §4.2.

4.1.1 Capture Region

We use the criterion from equation 4.7 to derive the location and boundaries of the "capture region" introduced in Chapter 2. Here we show an example for the derivation for the case of a disk with a flat rotation curve. The maximum and minimum values for the effective potential at the radius of corotation can be expressed as,

$$\Phi_{eff}(R_{CR}, \phi_{max}) = h_{CR} + |\Phi_s|_{CR} \tag{4.8}$$

and

$$\Phi_{eff}(R_{CR}, \phi_{min}) = h_{CR} - |\Phi_s|_{CR}. \tag{4.9}$$

The Jacobi integral (equation 2.1) for a star with zero random energy in a disk with a flat rotation curve can be explicitly written,

$$E_{J,flat} = \frac{1}{2}\Omega_p^2(R_{CR} - R)^2 + \Phi(R, \phi) - \frac{1}{2}\Omega_p^2 R^2, \tag{4.10}$$

where the first term ($E_{rot} = \frac{1}{2}v_{rot}^2 = \frac{1}{2}\Omega_p^2(R_{CR} - R)^2$) is an expression for the energy associated with the circular orbital velocity of a star in the rotating frame at some radial distance from corotation. Equation 4.5 describes the criterion for stars with zero random energy to be captured in trapped orbits. We can therefore use equation 4.10

to re-express equation 4.5 as,

$$\Phi_{eff}(R_{CR}, \phi_{min}) < \frac{1}{2}\Omega_p^2 R_{CR}^2 - \Omega_p^2 R R_{CR} + \Phi(R, \phi) \leq \Phi_{eff}(R_{CR}, \phi_{max}). \quad (4.11)$$

The coordinate-space solutions to the following equation

$$\Phi_{eff}(R_{CR}, \phi_{min}) = \frac{1}{2}\Omega_p^2 R_{CR}^2 - \Omega_p^2 R R_{CR} + \Phi(R, \phi) \quad (4.12)$$

define the boundary to the region of the disk wherein a star with zero random energy will be captured in a trapped orbit. This expression describes the "capture region" introduced in §2, which is shaded grey in Figure 2.1. The value of the difference $\Phi_{eff}(R_{CR}, \phi_{max}) - \Phi_{eff}(R_{CR}, \phi_{min})$ is set by the amplitude of the spiral potential (via equation 3.4) at corotation. Higher amplitude spirals will, therefore, lead to a larger area for the capture region. We investigate how the area of the capture region affects the efficiency of radial migration for a population of stars in Chapter 6.

4.2 Stars with Non-Zero Random Orbital Energy

Stars always have finite random orbital energy. It is well established that a star's orbital angular momentum and random orbital energy can be altered together when

the star encounters a fluctuation in the underlying disk potential away from corotation, particularly at the Lindblad resonances (eg. Spitzer & Schwarzschild, 1953; Barbanis & Woltjer, 1967; Wielen, 1977; Carlberg & Sellwood, 1985; Sellwood & Binney, 2002). As mentioned in §1.3, we refer to any event that changes both a star's random orbital energy and its orbital angular momentum as a "scattering" event. (We give a detailed discussion of scattering and the consequences of scattering for stars in trapped orbits in §4.4.3.) While stars are, in general, born on nearly circular orbits, scattering events lead to non-circular orbits. Therefore, the above capture criterion (equation 4.7) has limited utility in a disk galaxy and it is necessary to derive a capture criterion for stars on orbits that have random energy.

Equation 4.2 can be re-written in the standard quadratic form:

$$0 = AJ_\phi^2 + BJ_\phi + C \tag{4.13}$$

by making the following substitutions,

$$\begin{aligned} A &= c_{CR} \\ B &= 2b_{CR}J_R \\ C &= -E_J + h_{CR} + |\Phi_s|_{CR}\cos(m\phi_1) + \kappa_{CR}J_R + a_{CR}J_R^2. \end{aligned} \tag{4.14}$$

Real solutions for J_ϕ exist when

$$B^2 - 4AC \geq 0 \tag{4.15}$$

is satisfied. Provided that the disk is not in solid body rotation, $A = c_{CR}$ is inherently negative so that $-c_{CR} = |c_{CR}|$ and we can rewrite equation 4.15 to give:

$$E_J - h_{CR} - \kappa_{CR} J_R - \left(a_{CR} + \frac{b_{CR}^2}{|c_{CR}|} \right) J_R^2 \leq |\Phi_s|_{CR} \cos(m\phi_1). \tag{4.16}$$

Real solutions for J_ϕ exist for all values for ϕ_1 - and hence the star circulates about the galactic center in the rotating frame - when,

$$\Lambda_{nc} \equiv \frac{1}{|\Phi_s|_{CR}} \left[E_J - h_{CR} - \kappa_{CR} J_R - \left(a_{CR} - \frac{b_{CR}^2}{c_{CR}} \right) J_R^2 \right] \leq -1, \tag{4.17}$$

where the subscript "nc" indicates that Λ_{nc} sets the criterion for stars in non-circular orbits in the unperturbed potential.

Solutions are real for only a restricted range of values for ϕ_1 - and hence the orbit oscillates in azimuthal angle - for Λ_{nc} in the range

$$-1 < \Lambda_{nc} \leq 1. \tag{4.18}$$

A star that meets this criterion (equation 4.18) will be captured in a trapped orbit

librating around the local maximum in the effective potential (e.g. L_4). Note that when $J_R = 0$, the quantity $\Lambda_{nc} = \Lambda_c$.

The value of Λ_{nc} is a time-dependent quantity (in contrast to Λ_c which is time-independent) since both J_R and L_z are time-dependent (and related through the Jacobi integral) in a non-axisymmetric potential. A star that meets the criterion in equation 4.18 (and is therefore in a trapped orbit) will experience changes in its value for J_R as its orbital angular momentum oscillates (see equation 2.3), unless the star also has an instantaneous orbital angular frequency equal to the pattern speed of the perturbation. Consequently, a star that initially meets the capture criterion in equation 4.18 may not indefinitely continue to do so and could begin to orbit around the galactic center in the rotating frame. We discuss how the time-dependence of radial action and of angular momentum affect trapped orbits in §4.4.3.

4.3 Special Case: Power-Law Potential

Consider the special case of a star moving in a 2D plane under the influence of an unperturbed potential described by a spherical power law (see also Dehnen, 1999a, Appx. B) (an approximation for the multi-component galactic system - halo, bulge

and disk), plus an imposed spiral pattern

$$\Phi_0 = \begin{cases} \Phi_{00} \left(\frac{r}{r_p}\right)^{2-\beta} & \text{if } \beta \neq 2 \\ v_c^2 \ln(r/r_p) & \text{if } \beta = 2 \end{cases} \tag{4.19}$$

where r_p is the scale length of the potential, Φ_{00} is a constant, and the index β (related to the index used by Dehnen (1999a) - here denoted β_{Dehnen} - by $\beta = 2(1 - \beta_{Dehnen})$) can take a value between 0 (corresponds to solid body rotation) and 3 (Keplerian motion). The unperturbed circular frequencies in the plane of the disk vary with cylindrical coordinate R as

$$\Omega_c \propto R^{-\beta/2}. \tag{4.20}$$

The guiding center radius, R_L is given by equation 2.5. The epicyclic frequency of radial oscillation, κ (equation 2.4), can now be expressed in terms of the parameter β and the circular orbital frequency:

$$\kappa^2(R_L) = (4 - \beta)\Omega_c^2(R_L). \tag{4.21}$$

With these approximations, equations 4.3 can be expressed in terms of β for a given normalization.

The equations leading to the capture criterion may now be expressed in terms of

β, after substituting for κ. In particular, a_{CR} in equation 4.17 reduces to:

$$a_{CR} = \begin{cases} \left[\dfrac{v_c(R_{CR})^4}{R_{CR}^6}\dfrac{(4-\beta)(2-\beta)}{16}\right] \times \\ \quad [(1-\beta)(\beta)(1+\beta) + 60 - \frac{5}{3}(4-\beta)(2-\beta)(3+\beta)^2] & \text{if } \beta \neq 2 \\ -\dfrac{11 v_c^4}{3 R_{CR}^6} & \text{if } \beta = 2, \end{cases} \tag{4.22}$$

where the circular velocity at radial coordinate R is given by $v_c(R) \equiv \sqrt{R\Phi'}$ for $\beta \neq 2$ and v_c is constant for $\beta = 2$.

The ratio $-b_{CR}^2/c_{CR}$ in equation 4.17 can be expressed as

$$-\frac{b_{CR}^2}{c_{CR}} = \frac{\beta}{2R_{CR}^2}. \tag{4.23}$$

Figure 4.1 shows the value of the last term in equation 4.17, $(a_{CR} - b_{CR}^2/c_{CR})\, J_R^2$, as a function of R_{CR}, adopting the normalization so that $v_{c,\odot} = 220$ km s^{-1} at $R_\odot = 8$ kpc for all rotation curves and using equation 2.3 to express J_R in terms of random orbital energy in the epicyclic approximation. We use equation 2.3 to express $(a_{CR} - b_{CR}^2/c_{CR})\, J_R^2$ in units of energy given by $[E_{ran}^2/v_{c,\odot}^2]$. For $R_{CR}/R_\odot \gtrsim 0.1$, the value of $(a_{CR} - b_{CR}^2/c_{CR})\, J_R^2$ is of order unity for all allowed values of β. In comparison, the third term in equation 4.17 (i.e. $\kappa_{CR} J_R$) is equal to $v_{c,\odot}^2/E_{ran}$, in units of $[E_{ran}^2/v_{c,\odot}^2]$.[2] This ratio is large for the epicyclic approximation to be valid. For example, if one assumes that the disk has $v_{c,\odot}$ of order 10^2 km s^{-1} and random

[2]From equation 2.3, $\kappa_{CR} J_R = E_{ran} = v_{c,\odot}^2/E_{ran}\, [E_{ran}^2/v_{c,\odot}^2]$.

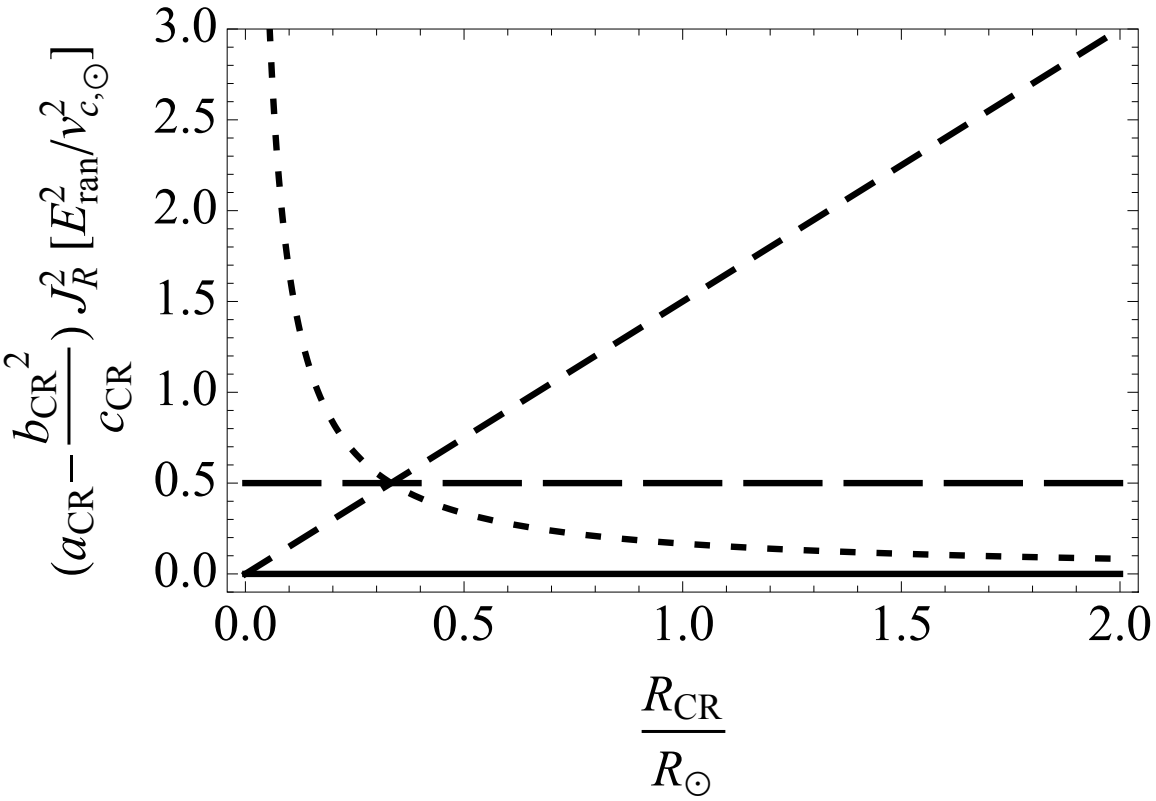

Figure 4.1: Value for $(a_{CR} - b_{CR}^2/c_{CR})\ J_R^2$ at $R_{CR}/R_\odot$ for $\beta = 0$ (solid; solid body rotation),1 (short-dash) 2 (long-dash; flat rotation curve), and 3 (medium-dash; Keplerian motion), normalized so that $v_{c,\odot} = v_c(R_\odot) = 220$ km s^{-1}, where $R_\odot = 8$ kpc.

velocity associated with the random energy (i.e. $v_{ran} = \sqrt{2E_{ran}}$) of order 10 km s^{-1}, then $\kappa_{CR}J_R$ is of order 10^3, while $(a_{CR} - b_{CR}^2/c_{CR})\ J_R^2$ is of order unity. We therefore omit the last term ($(a_{CR} - b_{CR}^2/c_{CR})\ J_R^2$) from equation 4.17 and write,

$$\Lambda_{nc,\beta} = \frac{1}{|\Phi_s|_{CR}} \left[E_J - h_{CR} - \kappa_{CR} J_R\right]. \tag{4.24}$$

The subscript, β, signifies that equation 4.24 is a good approximation within an underlying potential set by equation 4.19 for $0 \leq \beta \leq 3$.

Combining equations 4.24 and 4.18 we find the capture criterion for a star near

the corotation resonance of a spiral that has pattern speed Ω_p and amplitude at corotation, $|\Phi_s|_{CR}$, to be,

$$-|\Phi_s|_{CR} < E_J - h_{CR} - \kappa_{CR} J_R \leq |\Phi_s|_{CR}. \tag{4.25}$$

Substituting E_{ran}/κ for the radial action (as above) gives the following expression:

$$-|\Phi_s|_{CR} \leq E_J - h_{CR} - \left(\frac{R_L(t)}{R_{CR}}\right)^{\beta/2} E_{ran}(t) \leq |\Phi_s|_{CR}, \tag{4.26}$$

where we have explicitly shown the time dependent quantities in the non-axisymmetric potential.

Equation 4.26 gives the criterion for a star to be captured in a trapped orbit, in terms of orbital energy and orbital angular momentum (via $R_L(t)$), for all disk stars on orbits for which the epicyclic approximation holds. We expect the criterion in equation 4.26 to break down for highly eccentric orbits or for excursions in radius beyond the validity of the approximation of constant density in the underlying matter distribution. Rearranged and in a potential with a flat circular velocity (rotation) curve ($\beta = 2$),

$$\Lambda_{nc,2}(t) \equiv \Lambda_c - \left(\frac{R_L(t)}{R_{CR}}\right)\left(\frac{E_{ran}(t)}{|\Phi_s|_{CR}}\right), \tag{4.27}$$

The capture criterion for stars in orbits that are not highly eccentric is, in this case,

to a very good approximation,

$$-1 < \Lambda_{nc,2}(t) \leq 1. \tag{4.28}$$

As expected, $\Lambda_{nc,2} \rightarrow \Lambda_c$, the criterion for stars with zero radial action, in the limit that $E_{ran} \rightarrow 0$. The physical parameters that determine whether or not a star is captured in a trapped orbit are embedded in equation 4.28.

We showed in §4.1.1 that a star with zero random energy must have physical coordinates (R, ϕ) in the capture region (i.e. the grey region in Figure 2.1) to be in a trapped orbit. Solutions to equation 4.12 define the size, location, and shape of the capture region in a flat rotation curve. We now explore the significance of this capture region for stars with non-zero random orbital energy.

The direction of v_{ran} for a star at a given coordinate is important for determining whether or not that star meets the capture criterion, $-1 < \Lambda_{nc,2} \leq 1$. Figure 4.2 illustrates values of a star's random velocity (in the inertial frame) that satisfy the capture criterion for a spiral with $R_{CR} = 10$ kpc, $\theta = 10°$, and $\epsilon_\Sigma = 0.2$ in an underlying potential with a flat rotation curve and $v_c = 220$ km s^{-1}. Shaded panels indicate coordinates within the capture region (note that a star with $v_{ran} = 0$ satisfies the capture criterion only in the capture region). The curves in Figure 4.2 show values of $\Lambda_{nc,2}$, within the range $-1 < \Lambda_{nc,2} \leq 1$, for v_{ran} entirely in the radial direction (solid, red) and entirely in the azimuthal direction (dashed, blue). Note that in the

capture region, the solid (red) curve spans a broad range of random radial velocities, indicating that the value of $\Lambda_{nc,2}$ is not sensitive to radial random motion. This contrasts with the dashed (blue) curve, which satisfies the capture criterion for only a restricted range of velocities, illustrating that $\Lambda_{nc,2}$ is sensitive to azimuthal random motion. The direction of the random velocity is important because the azimuthal velocity determines the angular momentum of the star, and therefore its guiding center radius, R_L (equation 2.5), whereas a star with random motion solely in the radial direction will have $R = R_L$.

Consider the situation of two stars (Star A and Star B) that have the same instantaneous position ($\mathbf{x}$) and instantaneous angular momentum ($R_{L,A} = R_{L,B}$), but have different values for their instantaneous random energy (E_{ran}). Star A has $E_{ran,A} = 0$ and Star B has some finite random energy, $E_{ran,B}$. The value of E_J for Star B will therefore be greater than that of Star A ($E_{J,B} > E_{J,A}$). All the instantaneous random energy must be in the form of radial motion at that time and therefore the rotational (E_{rot}) and random (radial) components of $\dot{\mathbf{x}}^2$ in equation 2.1 are orthogonal, and $E_{J,A} = E_{J,B} - E_{ran,B}$. With the capture region defined as in equation 4.10 ($\Phi_{eff}(R_{CR}, \phi_{min}) = E_{rot}(R) + \Phi_{eff}(R, \phi)$), and given that the velocities leading to E_{rot} and E_{ran} are orthogonal, the capture criterion (equation 4.26) can be written as:

$$\Phi_{eff}(R_{CR}, \phi_{min}) < E_{rot}(R) + \Phi_{eff}(R, \phi) + \left(1 - \frac{R_L(t)}{R_{CR}}\right)^{\beta/2} E_{ran}(t) \leq \Phi_{eff}(R_{CR}, \phi_{max}). \tag{4.29}$$

Should Star A be within the capture region at the time under consideration then $R_L \approx R_{CR}$. In that case, even though Star B may have a different value for E_{ran}, given that $R_{L,B} = R_{L,A}$, the value of the random energy is of little consequence as to whether or not the star meets the capture criterion.[3] For example, the solid (red) curve in the panel of Figure 4.2 where $R = 10.2$ kpc and $\phi = -15°$ shows that the value of $\Lambda_{nc,2}$ has little dependence on the value of the random energy.

The case of a star with random velocity in the azimuthal direction is more complex. The rotational (v_{rot}) and random (v_{ran}) velocities in the rotating frame are not orthogonal, and therefore the random orbital energy and the angular momentum are not independent. The dashed, blue curve in Figure 4.2 shows the value of $\Lambda_{nc,2}$ in the limiting case of a star particle that has its random motion entirely in the azimuthal direction. In every panel in Figure 4.2, it is clear that the value of $\Lambda_{nc,2}$ has a strong dependence on the value of the random velocity in the azimuthal direction. In combination with the above discussion on radial motion, one can conclude that whether or not a star is in a trapped orbit is primarily determined by its orbital angular momentum ($R_L(t)$), and less so by $E_{ran}(t)$.

Finally, when a single star is scattered (i.e. it has changes in angular momentum with associated changes in random energy by equations 2.3), the value of $\Lambda_{nc,2}(t)$ may change to such a degree that the star no longer meets the capture criterion (equation 4.28). This arises since a star's value of E_J (and therefore Λ_c) is conserved,

[3]For R_L away from corotation, other gravitational processes, like interactions with the Lindblad resonances, become important. We discuss this in more detail in §4.4.3

while $E_{ran}(t)$ and $R_L(t)$ are time dependent. We discuss this in more detail in §4.4.3.

In the next section we carry out numerical tests of the predictive power of equation 4.28, in a 2D disk with an imposed spiral perturbation.

4.4 Numerical Exploration

4.4.1 The Approach

We use an orbital integrator[4] to follow the orbits of test particles in an underlying potential. We follow each particle for 2×10^9 yr using 10^2 yr fixed time-steps. We verified that differences of 1 km s^{-1} in the initial orbital velocity did not lead to largely divergent orbital paths in the underlying axisymmetric potential; we therefore conclude that our choice for the length of the time-step is sufficient for this analysis. The mean fractional deviation in the value of the Jacobi integral per time-step is of order $\sim 10^{-5}$.

We adopt the underlying potential given by equation 4.19 with $\beta = 2$ and parameter values given in Table 3.1. Therefore the rotation curve in the plane of the disk is flat. Our chosen value for the potential scale length renders changes in $\Phi_0(R)$ for stars in trapped orbits (usually moving a radial distance < 1 kpc around R_{CR}) to be $|\Delta\Phi_0|/|\Phi_0| < 10\%$ between $4 < R_{CR} < 15$ kpc.

We adopt an exponential radial surface density for the disk given in equation 3.11

[4]We use a 2^{nd} order leapfrog orbital integrator.

with normalization constant and scale length as given in Table 3.1.

We superimpose a perturbation to the underlying potential corresponding to an m-armed Lin-Shu spiral density wave (Lin & Shu, 1964; Lin, Yuan, & Shu, 1969; Binney & Tremaine, 2008) with pattern speed, Ω_p discussed in §3.1. Consequently the spiral amplitude (Φ_s) is larger for small wavenumber (k) in our model. Further, the spiral amplitude for fixed pitch angle (θ) peaks at the disk scale length (R_p), since $\Sigma(R)/k(R) \propto R\, e^{-R/R_d}$ for an exponential disk. Note that the choice for the radius of corotation, fractional amplitude in surface density, spiral wave number, and pitch angle of the spiral pattern therefore affects the the size, shape and location of the capture region (§4.1.1). We will investigate the effects of these choices in Chapters 5 & 6.

For illustrative purposes we adopt a spiral amplitude that is typically higher (e.g. $\theta = 25^\circ$ and $\epsilon_\Sigma = 0.3$) than estimates from observations of external disk galaxies (e.g. Rix & Zaritsky, 1995; Seigar & James, 1998; Ma, 2002). Our choice of spiral amplitude causes the capture region to be larger than one would expect from a more modest choice and consequently a larger fraction of stars in the disk will meet the capture criterion.

4.4.2 Testing the Capture Criteria

We model stars as test particles and compute the orbits assuming a range of initial conditions. We adopt parameter values for the spiral patterns such that $0.1 \leq \epsilon_\Sigma \leq 0.5$, $5^\circ \leq \theta \leq 45^\circ$, $0 \leq m \leq 4$ and $4 \leq R_{CR} \leq 15$ kpc. Each test particle is launched

with an initial position in the rotating frame $(R(t_0), \phi_1(t_0)) \equiv (R_0, \phi_{1,0})$ that is within 5 kpc of corotation and at a range of azimuthal positions[5]. Each initial velocity

$$\mathbf{v}_0 = \mathbf{v}_{ran,0} + \mathbf{v}_c \tag{4.30}$$

has a speed in any direction up to 50 km s^{-1}.

For each set of initial conditions, we test (1) the validity of the appropriate capture criterion (equations 4.7 or 4.28) and (2) the importance of orbital angular momentum and random energy to determining whether or not a star is in a trapped orbit. We do not show the results from our exploration across the entire range of initial conditions, but rather a representative subset, where we have adopted parameter values given in Table 3.1, unless otherwise stated.

The choice of direction for the initial random velocity of a star determines the phase on its epicyclic orbit and thus the coordinate of its guiding center at $t = 0$. Therefore, the primary difference between launching a star at (R_0,$\phi_{1,0}$) with given random energy and initial random velocity ($E_{ran,0} \equiv E_{ran}(t = 0) = \frac{1}{2}v^2_{ran,0}$ per unit mass) either entirely in the $\hat{\mathbf{R}}$-direction or entirely in the $\hat{\boldsymbol{\phi}}$-direction is that the former corresponds to an orbit with $R_{L,0} \equiv R_L(t = 0) = R_0$, while the latter corresponds to an orbit with $R_{L,0} = R_0(v_{ran,0,\phi} + v_c)/v_c$ (equation 2.5).

Figure 4.3 shows an orbit for a test particle that does not meet either capture

[5]We set the azimuthal coordinate $\phi = 0$ at the position of the minimum surface density, which is located between the spiral arms

criterion ($\Lambda_c = -2.8$ and $\Lambda_{nc,2}(t = 0) = -2.6$, as printed in panel (b)) at the time of launch and is therefore expected not to be in a trapped orbit (§4.3).[6] The test particle has initial coordinate $(R_0, \phi_{1,0}) = (6.5 \text{ kpc}, 0)$ and initial random velocity $|v_{ran,0}| = 0$ km s^{-1}. This orbit is not circular, despite having zero initial random velocity, since neither angular momentum nor random energy is conserved in a non-axisymmetric potential. Note that neither R_0 nor $R_{L,0}$ is in the capture region and the star orbits around the galactic center. Panel (a) shows the orbital path in the rotating frame (solid, rainbow) for a star with initial position marked with a red star. The solid dark-green curve in both panels indicates the radius of corotation. The shaded grey area shows the capture region, and the curved lines (thin, magenta) show the location of the spiral arms. The epicyclic phase at launch is shown in the inset of panel (a) (positioned arbitrarily so as not to obscure the figure). Panel (b) shows $R_L(t) - R_{CR}$ (dotted, black) and $R(t) - R_{CR}$ (solid, red) as a function of time. A star that is in a trapped orbit will have a guiding center radius, $R_L(t)$, that oscillates about the radius of corotation.

Figure 4.4 shows a test particle launched with the same set of initial conditions used to produce the orbit in Figure 4.3, except that the initial random motion in the radial direction is modified so that $v_{ran,0,R} = 50$ km s^{-1}. A test particle in this orbit has the same guiding center radius as the star in Figure 4.3, but its value for $E_{ran,0}$ is higher. The discussion at the end of §4.3 would suggest that this test particle should

[6]Recall that the capture criteria (equations 4.7 & 4.28) predict that a star is in a trapped orbit only for stars with a value of Λ_c or $\Lambda_{nc,2}(t)$ (respectively) between -1 and 1.

not be in a trapped orbit, even when its orbital trajectory enters the capture region. Indeed, panel (a) of Figure 4.4 shows that the test particle orbits the galactic center in the rotating frame, and panel (b) shows that the guiding center radius does not oscillate about the radius of corotation (both indicating that it is not in a trapped orbit). The two capture criteria (equations 4.7 & 4.18) give different predictions; the capture criterion for a star with zero random energy suggests that the star is in a trapped orbit ($\Lambda_c = 0.5$), whereas the capture criterion we derive is not satisfied ($\Lambda_{nc,2}(t = 0) = -2.0$), suggesting that the test particle is not in a trapped orbit. We conclude that the capture criterion derived in §4.2 accurately predicts whether or not this is a trapped orbit.

Figure 4.5 shows a test particle that is launched with the same set of initial conditions used to produce the orbit in Figure 4.3 except that the initial random motion in the azimuthal direction is modified so that $v_{ran,0,\phi} = 30$ km s^{-1}. A test particle in this orbit has both higher random orbit energy and orbital angular momentum ($R_{L,0} = 7.4$ kpc) than the test particle in Figure 4.3. The capture criterion for a star with zero random energy suggests that the star is not in a trapped orbit ($\Lambda_c = 1.7$), whereas the capture criterion we derived is satisfied ($\Lambda_{nc,2}(t = 0) = -0.3$), leading to the expectation that the test particle is in a trapped orbit. The figure confirms the prediction given by our capture criterion ($\Lambda_{nc,2}(t = 0)$), as the test particle oscillates about the corotation radius and between the spiral arms indicating that it is in a trapped orbit. Again, the capture criterion derived in §4.2 accurately predict

whether or not this is a trapped orbit. In this case, the guiding center radius is within the capture region, while the orbital trajectory is not confined to it.

In Figure 4.6, we explore how the azimuthal position of a star affects whether or not it is in a trapped orbit, given the same initial radius ($R_0 = 9.1$ kpc), random orbital energy and orbital angular momentum. With these things held constant between test particles, the value of Φ_{eff} is not the same for different initial azimuthal coordinates, because $\Phi_{eff} = \Phi_{eff}(R, \phi)$. Consequently, the value of Jacobi integral, and thus the value of $\Lambda_{nc,2}(t = 0)$, for each test particle is different and therefore two test particles under these conditions might not both have the same trapped status. The $m = 2$ spiral perturbation used in Figure 4.6 has $R_{CR} = 9.5$ kpc and is otherwise the same prescription used in Figure 4.3. The initial conditions are modified from Figure 4.3 such that each test particle is launched from the apocenter of its epicycle with the value of the initial velocity being $(v_{ran,0,R}, v_{ran,0,\phi}) = (0, -10)$ km s^{-1}. The initial azimuthal coordinates in the three sets of panels in Figure 4.6 are $\phi_{1,0} = \{\phi_{max}, \phi_{min}/2, \phi_{min}\} = \{0, \pi/4, \pi/2\}$ (from top to bottom). In the left panels, we plot the contour for which $\Phi_{eff} = E_J$ (the ZVC) as a thin, dashed line, when a ZVC exists. In the top and middle sets of panels, the capture criterion is met ($\Lambda_{nc,2}(t = 0) = 0.8$ and 0.0, respectively) and the test particle is in a trapped orbit. In the bottom set of panels, $\Lambda_{nc,2}(t = 0) = -1.1$ and the test particle is *not* in a trapped orbit and instead circles the galactic center in the rotating frame. We again note that in all cases where the test particle is in a trapped orbit,

the guiding center radius (thick, dotted, black curve) is within the capture region, and in all cases where the test particle is not trapped it is not in the capture region. The results in Figure 4.6 demonstrate that the range in R_L for which a star meets the capture criterion is dependent on azimuthal position, as one might expect from the radial thickness of the capture region as a function of azimuth. This matches the prediction of the capture criterion (equation 4.28) at $t = 0$ printed in the panels on the right.

The value of the quantity $\Lambda_{nc,2}(t = 0)$ in Figures 4.3-4.6 is much better at predicting (via equation 4.28) whether or not a test particle with some finite value for E_{ran} is in a trapped orbit than is Λ_c (criteria for stars with $E_{ran} = 0$), as is expected. In the case that $E_{ran} = 0$, $\Lambda_{nc,2}(t = 0) = \Lambda_c$ and both are valid capture criteria. Although the derivation of $\Lambda_{nc,2}$ assumes the epicyclic approximation, our tests (not all shown) suggest that the value of $\Lambda_{nc,2}(t)$ is a valid predictor of "trapping" for stars on non-circular orbits where the unperturbed orbital trajectory would not be well described by the epicyclic approximation (e.g. radial excursions in Figure 4.4 are on order of a scale length). We therefore conclude that the value of $\Lambda_{nc,2}(t)$ (via equation 4.28) is a robust indicator for whether or not a star is in a trapped orbit, while Λ_c (via equation 4.7) is only able to predict whether or not a star on an orbit with no random energy is in a trapped orbit. We further explore our capture criteria in the event of scattering in the next subsection (§4.4.3).

In all the cases we tested numerically (not all of which are shown), a star is

captured in a trapped orbit when its guiding center radius (not the star itself) is within the capture region. Further, a test particle that is not captured in a trapped orbit has its guiding center radius outside the capture region. In the limit that a star has zero random energy (i.e., $R = R_L$) it is in a trapped orbit when the star itself is positioned in the capture region. There is no such requirement for the trajectory of test particles with some finite random orbital energy since the guiding center of the star is not equal to its coordinate position. A trapped test particle may have a trajectory that physically leaves the capture region, while its guiding center radius remains within the capture region (e.g. Figure 4.5). A test particle that is not captured in a trapped orbit may enter the capture region (e.g. Figure 4.4), while its guiding center radius does not enter the capture region. We, therefore, confirm our earlier prediction (§4.3) that it is largely orbital angular momentum that determines whether or not a star is in a trapped orbit.

4.4.3 Scattering

We defined scattering in §1.3 & §4.2 as any process that changes both a star's orbital angular momentum and random orbital energy (e.g. Spitzer & Schwarzschild, 1953; Barbanis & Woltjer, 1967; Wielen, 1977). This is in contrast to the oscillatory changes in the orbital angular momentum of a star in a trapped orbit, that are not accompanied by significant changes random orbital energy. Up to this point we have not discussed what happens to a star that is in a trapped orbit when it is scattered.

A star is in a trapped orbit when the amplitude of the quantity $\Lambda_{nc}(t)$ (equation 4.17) is less than unity (by equation 4.18). This quantity depends on both a star's orbital angular momentum and random orbital energy, and is not conserved. A star on an orbit that initially meets the capture criterion (equation 4.26) will continue to do so unless it is scattered such that $|\Lambda_{nc,\beta}(t)|$ becomes greater than unity, at which time the star will no longer be in a trapped orbit.

Our orbital integrator uses a smooth underlying potential, with a superposed spiral perturbation that has constant amplitude for the duration of the orbital integration. This is appropriate for testing the validity of equation 4.28, but such a potential is also somewhat unrealistic. It is well established that small-scale fluctuations in the galactic potential (such as GMCs) (Spitzer & Schwarzschild, 1953; Wielen, 1977; Lacey, 1984) as well as short lived, physically extended fluctuations (such as transient spiral arms) (Barbanis & Woltjer, 1967; Carlberg & Sellwood, 1985; De Simone, Wu, & Tremaine, 2004) lead to scattering of stellar orbits, altering random orbital energies and orbital angular momenta. It is therefore important to understand that stars we find to remain in trapped orbits indefinitely may not be representative of stellar behavior in a lumpy (i.e. small scale-length fluctuations in the potential), time-dependent underlying potential, where we expect that many of these stars would be scattered out of their trapped orbits.

Despite the rather smooth potential we assume, we are able to observe the effects of scattering on the orbital trajectory of a test particle and its value of $\Lambda_{nc,2}(t)$. We

observe two processes by which stars are scattered (illustrated below).

First, a star in a non-axisymmetric potential is scattered whenever it is not in instantaneous corotation with the perturbing pattern (by equation 2.3, and equation 4 in Sellwood & Binney, 2002). There is a range of values for the guiding center radius, $R_L(t)$ (and therefore a range in Ω_g), that satisfies the capture criterion (equation 4.28), not simply the 0^{th} order assumption that $R_L = R_{CR}$. Indeed, a star in a trapped orbit has an oscillating value for $R_L(t)$ (i.e. $\Omega_g(t)$). Therefore, other than when a star's guiding center radius equals the radius of corotation - which happens twice during its trapped orbit - the star will experience changes in its orbital angular momentum that are accompanied by changes in random orbital energy (see equation 2.3). This type of scattering becomes particularly important when the spiral wave number is large (i.e. the radial spacing between spiral arms is small) and a star particle that is in a trapped orbit has a close approach to a spiral arm away from corotation. Through such interactions away from corotation, a star particle that is initially captured in trapped orbits may begin circling the galactic center in the rotating frame (i.e. no longer in a trapped orbit).[7] We defer a discussion of the time-scale for this type of scattering out of a trapped orbit to future work (see Chapter 8).

Second, changes to a star's random orbital energy ($E_{ran}(t)$) are most dramatic at

[7]The first order change to a phase space *distribution function* tends to zero away from spiral resonances (Carlberg & Sellwood, 1985).

the Lindblad resonances, the radii at which

$$\kappa = \pm m(\Omega_p - \Omega_\phi), \tag{4.31}$$

where the star passes (or is passed by) the perturbation at the star's epicyclic frequency. One would expect enhanced scattering should a star in a trapped orbit cross a Lindblad resonance. The capture region can overlap with a Lindblad resonance when either, (1) the radial range of the capture region is large (e.g. the amplitude of the spiral potential is high), or (2) the Lindblad resonances are close to corotation (e.g. for values of R_{CR} that are close to the galactic center). We observe erratic changes in the motion when the guiding center radius ($R_L(t)$) of a star in a trapped orbit encounters a Lindblad resonance (including the ultra-harmonic Lindblad resonances, where

$$\kappa = \pm 2m(\Omega_p - \Omega_\phi). \tag{4.32}$$

Chirikov (1979) predicted that chaotic behavior would emerge when an object enters a region of resonant overlap in phase space (i.e. the region in a surface of section where two resonances occupy the same space). Irregular orbital motions (sometimes called "wild" or ergodic) have been observed to arise in simulations when stars pass through regions of resonant overlap in phase space (eg. Martinet, 1974; Athanassoula et al., 1983; Pichardo et al., 2003); where Pichardo et al. (2003) used a Lyapunov exponent analysis to identify these motions as chaotic.

In the present case, we are observing resonant overlap in coordinate space. The boundary between orbits that circle the galactic center in the rotating frame and orbits that are trapped is called the "separatix" in a surface of section diagram. In the case of zero random energy, the separatix can be projected onto coordinate space as a contour that encloses the capture region. As per the discussion in §4.4.2, stars with some finite random orbital energy that are in trapped orbits have guiding center radii that are inside the capture region. We do not quantitatively prove that we are observing the emergence of chaotic behavior at resonant overlap, however, our tests are consistent with this theory as there is a sudden increase in random energy and change in orbital trajectory when the guiding center radius of a trapped star encounters a Lindblad resonance (equations 4.31 & 4.32).

Figures 4.7, 4.8, & 4.9 show the orbits of test particles for three sets of initial conditions. Each test particle initially meets the capture criterion (equation 4.28) and is launched with initial random velocity $(v_{ran,0,R}, v_{ran,0,\phi}) = (10, 10)$ km s^{-1} at an initial radius 1 kpc inside the radius of corotation for $R_{CR} = \{8.5, 8.0, 6.0\}$ kpc respectively. For each set of initial conditions, panel (a) shows the orbital path in the rotating frame, as in Figure 4.3. Panel (b) shows the time evolution of $\Lambda_{nc,2}(t)$ (solid, red). The horizontal black lines at $\Lambda_{nc,2}(t) = 1$ and -1 are the upper and lower limits for trapped orbits. Panel (c) shows the random orbital energy normalized by its initial value $(E_{ran}(t)/E_{ran,0})$ (solid, blue). The horizontal black line at $E_{ran}(t)/E_{ran,0} = 1$ indicates the initial value. Panel (d) shows $(R_L(t) - R_{CR})$ (solid, black). In both

panes (a) and (d), dashed, dark-green curves show the inner and outer Lindblad resonances (ILR/ORL, equation 4.31), and the dotted dark-green lines show the first ultra-harmonic Lindblad resonances (these are the $2m$:1 resonances for an m-armed perturbation, equation 4.32). Figure 4.7 shows a star particle in a trapped orbit that is not significantly scattered. Figures 4.8 & 4.9 show star particles that are initially in a trapped orbit but are scattered such that they no longer meet the capture criterion. The vertical black line in panels (b)-(d) marks the time when $|\Lambda_{nc,2}(t)| > 1$, and thus the star particles are no longer in trapped orbits. The star particle in Figure 4.8 is scattered out of a trapped orbit when the star approaches a spiral arm away from corotation (instantaneous $R_L \neq R_{CR}$). As can be seen in panel (d), the vertical black line does not correspond to a time when the guiding center radius crosses a Lindblad radius, but rather when the star has an increase in random orbital energy as it approaches the peak density of the spiral perturbation away from corotation. Figure 4.9 shows a star particle that initially meets the capture criterion but is scattered out of a trapped orbit (marked by the vertical black line in the right-hand panels). In panel (d), it is clear that this corresponds to the time when the guiding center radius ($R_L(t)$) crosses the ultra-harmonic OLR (dotted, horizontal line). These plots illustrate that a star with some finite random orbital energy, which is initially in a trapped orbit, can be scattered leading to $|\Lambda_{nc,2}(t)| > 1$. Although we do not show an example here, it is possible that a star that is not initially in a trapped orbit could be captured in a trapped orbit if it is scattered in such a way

that equation 4.28 is satisfied.

A capture region with a larger area, which grows with spiral strength (see discussion in §4.1.1), will be able to support trapped orbits for stars with guiding center radii farther from corotation. The radial range of the capture region is important since a star's random energy slowly increases with radial distance from corotation and since a broad capture region is more likely to overlap with a Lindblad resonance. Therefore the amplitude of our chosen spiral perturbation to the potential (equation 3.4) is greater for spirals that have a high fractional amplitude in surface density (ϵ_Σ), in regions of the disk that have a small wave number ($k(R) = m\cot(\theta)R^{-1}$), and as $|R - R_d| \to 0$ in a disk with an exponential surface density since $\Phi_s \propto R\,\Sigma(R)$.

In a lumpy underlying potential (unlike the one we use), a star that is in a trapped orbit will also have gravitational interactions with fluctuations in the potential other than the spiral pattern. These interactions will cause the star to have changes in its orbital angular momentum and random energy (see Sellwood, 2014a, and references therein) that may cause the star to no longer meet the capture criterion.

Finally, resonant overlap can also occur when there are two (or more) perturbations to the underlying axisymmetric potential with different pattern speeds. Minchev & Famaey (2010) simulated (further explored by Minchev et al., 2011) a disk with both a bar and spiral perturbation. They found that when resonances of the two patterns overlapped, the changes to the orbital angular momentum of disk stars were greater than the sum of the separate changes in orbital angular momentum from the individual

non-axisymmetric patterns. In the context of the present work, we would expect irregular orbits to emerge in the case that the OLR of a central bar pattern overlaps the capture region from the spiral pattern.

4.5 Capture for a Non-Steady Spiral Pattern

Thus far in this work, we have considered the case of a spiral perturbation with a pattern speed that is independent of radius and time. However, N-body simulations of disk galaxies frequently exhibit spiral arms that appear to have pattern speeds that are radially dependent (e.g. Grand, Kawata, & Cropper (2012), Baba et al. (2013), Roca-Fàbrega et al. (2013); but see Sellwood & Carlberg (2014) for an alternative interpretation) or that evolve in time (e.g. Roškar et al., 2012). We now explore how radial migration would differ from the analysis in this work should either scenario be the case.

In Appx. A, we explore the difference between two different capture criteria for stars with zero random energy. Equations A.6 and A.9 relate the radial range for a star with zero random orbital energy to be in a trapped orbit (and therefore the size of the capture region) to the shape of the rotation curve given the spiral has a constant pattern speed. The nature of this relationship is most transparent in equation A.5, but can be obtained from equation 4.24 or equation A.8 with appropriate choice of

the functional form of $\dot{x}_\phi$. Equation A.5 can be rearranged to solve for the radial range of the capture region (ie. the maximum value for $|R(t) - R_{CR}|$) in the effective potential for a given shape of the rotation curve. For the same amplitude of the perturbation ($|\Phi_b|$) and pattern speed (Ω_p), a central point potential has the smallest radial range for the capture region, while stars in solid body rotation are in corotation at all R and therefore are captured at all radii. The corollary is that the radial range of the capture region is determined by the rate of divergence with distance from corotation between the possibly radially dependent pattern speed ($\Omega_p(R)$) and the circular orbital frequency ($\Omega_c(R)$). Should the functional form of the pattern speed approach that of the circular orbital frequency, the radial range for capture would include the entire disk. In support of this interpretation, Grand et al. (2012) found that in a 3D N-body simulation of a disk with transient spiral arms with $\Omega_p(R) \approx \Omega(R)$, stars from a wide range of initial radii migrated along the spiral arms, sometimes having $10 - 20\%$ changes in angular momentum.

In the case of steady spiral patterns, very efficient radial migration requires multiple transient spiral patterns, with a random distribution of pattern speeds, over the lifetime of the disk. In such a scenario, a star will migrate radially as a random walk, where the size of any step is determined by the amplitudes of the perturbations (Sellwood & Binney, 2002, see Chapter 5 and) and the number of steps is related to the duty cycle of transient spirals. However, should a spiral pattern speed be time-dependent, a small amplitude spiral could cause a star to migrate over a large

radial distance. To understand this, consider a disk with a flat rotation curve and a spiral pattern speed that decreases in time, thus causing the radius of corotation to increase with time and the location of the capture region to move to ever larger radii. Should the guiding center radius of a trapped star be increasing at the same rate as the radius of corotation, the star could continuously migrate outward for the lifetime of the spiral pattern. In the same scenario, a star which had a different initial phase in its trapped orbit such that its guiding center radius is decreasing might only be trapped briefly as the capture region moves outward. Such time dependent pattern speeds could cause the ensemble of disk stars to migrate longer distances preferentially outward (or inward in the case of a pattern speed that increases with time), and even a low amplitude spiral could lead to large radial excursions for such stars. There are examples of time-dependent spiral structure in simulations of spiral galaxies (e.g. Roškar et al., 2012; Sellwood & Carlberg, 2014), but it is unclear whether or not these patterns host stars that migrate large radial distances.

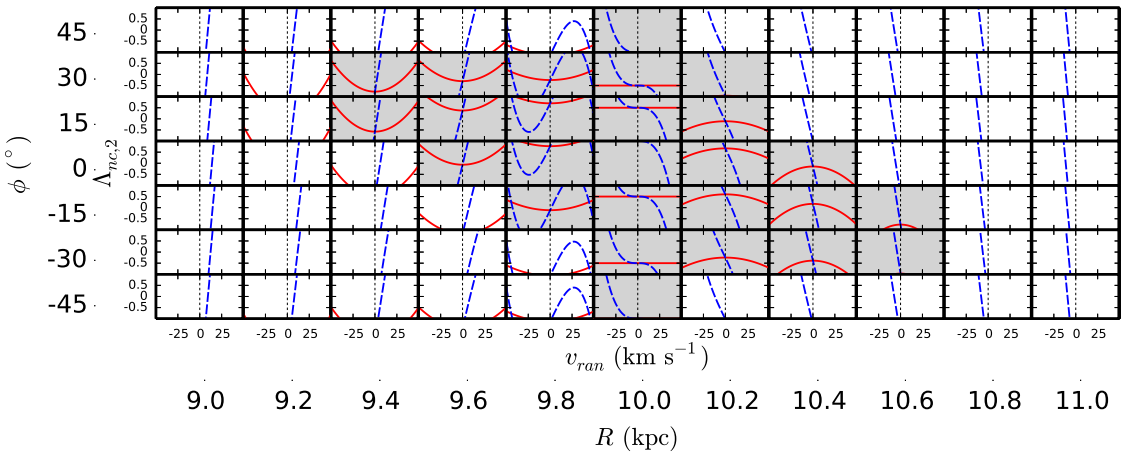

Figure 4.2: Each panel shows the value of the random velocity in the inertial frame (v_{ran}) on the x-axis and its associated value of $\Lambda_{nc,2}$ on the y-axis, (within the range $-1 < \Lambda_{nc,2} \leq 1$, which satisfies the capture criterion), for a star at a given coordinate. The coordinate corresponding with each panel falls in the range 9 kpc$\leq R \leq$ 11 kpc in 0.2 kpc intervals (horizontal direction) and $-45° \leq \phi \leq 45°$ in 15° intervals (vertical direction). The coordinate grid is labeled on the exterior of the plot. We have assumed a spiral with $R_{CR} = 10$ kpc, $\theta = 10°$, and $\epsilon_\Sigma = 0.2$, in an underlying potential with a flat rotation curve and circular velocity $v_c = 220$ km s^{-1}. Solid (red) curves show the value of $\Lambda_{nc,2}$ corresponding to $\mathbf{v}_{ran} = |v_{ran}|\hat{\mathbf{R}}$, and the dashed (blue) curves are for $\mathbf{v}_{ran} = |v_{ran}|\hat{\boldsymbol{\phi}}$. The capture region is defined as the locus within which a star with zero random motion in the inertial frame ($v_{ran} = 0$ marked by a vertical, dotted line) satisfies the capture criterion. Panels for coordinates that are within the capture region have a shaded background. For a star with coordinates within the capture region, there is a large range in radial random motion that gives rise to orbits that satisfy the capture criterion (solid, red), suggesting that random orbital energy alone is not a significant determining factor for trapped orbits. The range of random motion in the azimuthal direction - associated with orbital angular momentum as well as random orbital energy - for a star to satisfy the capture criterion (dashed, blue) is relatively small, leading to the conclusion that whether or not a star is captured in a trapped orbit is sensitive to the value of that star's orbital angular momentum. A star with coordinates that is outside the capture region may still satisfy the capture criterion. For example, the panel with $R = 9.2$ kpc and $\phi = 30°$ illustrates that over a narrow range of random velocities in either direction $|\Lambda_{nc,2}| < 1$.

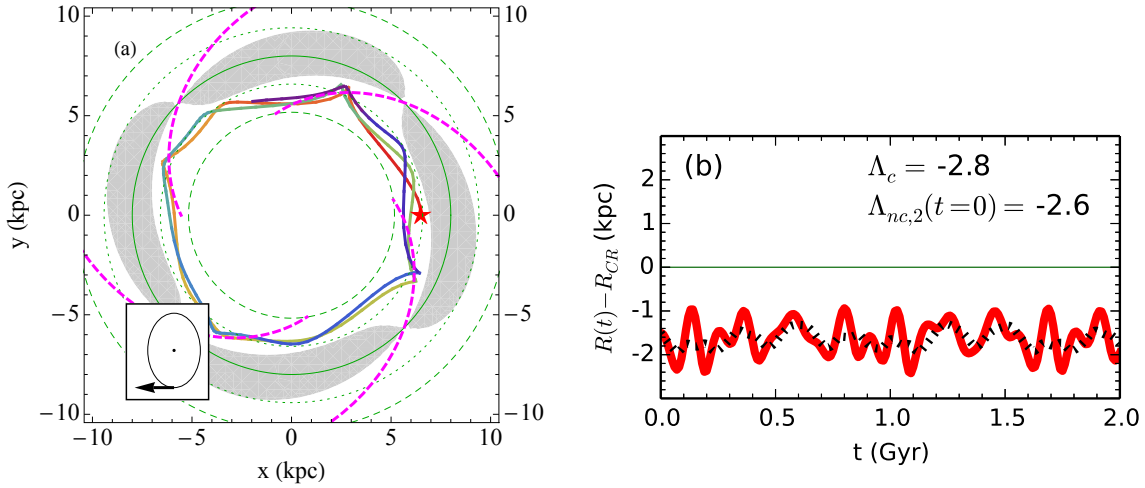

(a) (b)

Figure 4.3: Orbital trajectory and properties for a star that is not in a trapped orbit. The potential is modified from that shown in Figure 2.1 by setting $R_{CR} = 8$ kpc and $\theta = 25°$. The test particle is launched with zero random energy ($|v_{ran,0}| = 0$ km s^{-1}) at $(R_0, \phi_{1,0}) = (6.5 \text{ kpc}, 0)$ (red star). Panel (a) shows the orbital trajectory in the rotating frame (solid, rainbow) for 2 Gyr ($\gtrsim$ 2 orbital periods). The shaded area shows the capture region and the inset shows the phase of the star's epicyclic orbit at the time of launch. The solid dark-green line marks the radius of corotation, R_{CR}, in both panels. Panel (b) shows the time-dependent guiding center radius, $R_L(t) - R_{CR}$ (black, dotted), and radial coordinate $R(t) - R_{CR}$ (solid, red). The value for Λ_c and the initial value for $\Lambda_{nc,2}(t = 0)$ are printed in panel (b).

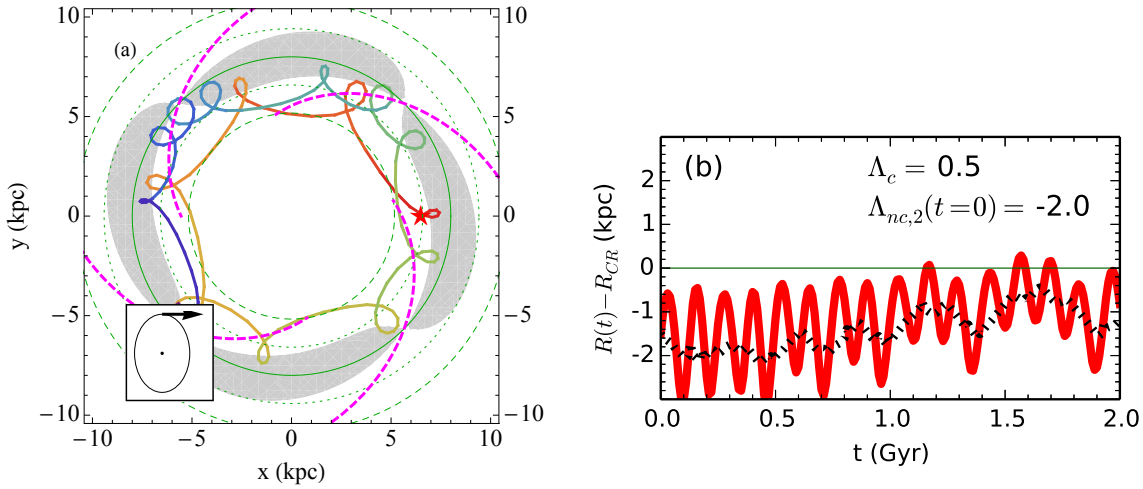

(a) (b)

Figure 4.4: The panels and plotted colors and curve patterns have the same meaning have the same as in Figure 4.3. Initial conditions are the same except the initial radial velocity is modified so that $v_{ran,0,R} = 50$ km s^{-1}. This star's orbital trajectory enters the capture region but its guiding center does not. As expected from the capture criterion, this star is not in a trapped orbit.

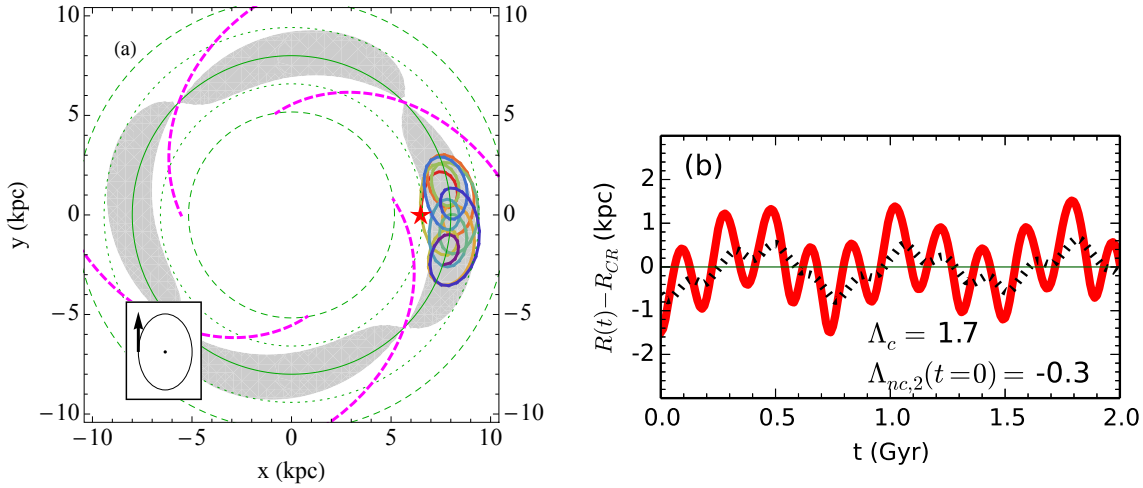

(a) (b)

Figure 4.5: The panels and plotted colors and curve patterns have the same meaning as in Figure 4.3. Initial conditions are also the same except the initial azimuthal velocity is modified so that $v_{ran,0,\phi} = 30$ km s^{-1}. The orbital trajectory leaves the capture region, but R_L remains within the capture region. This star is in a trapped orbit.

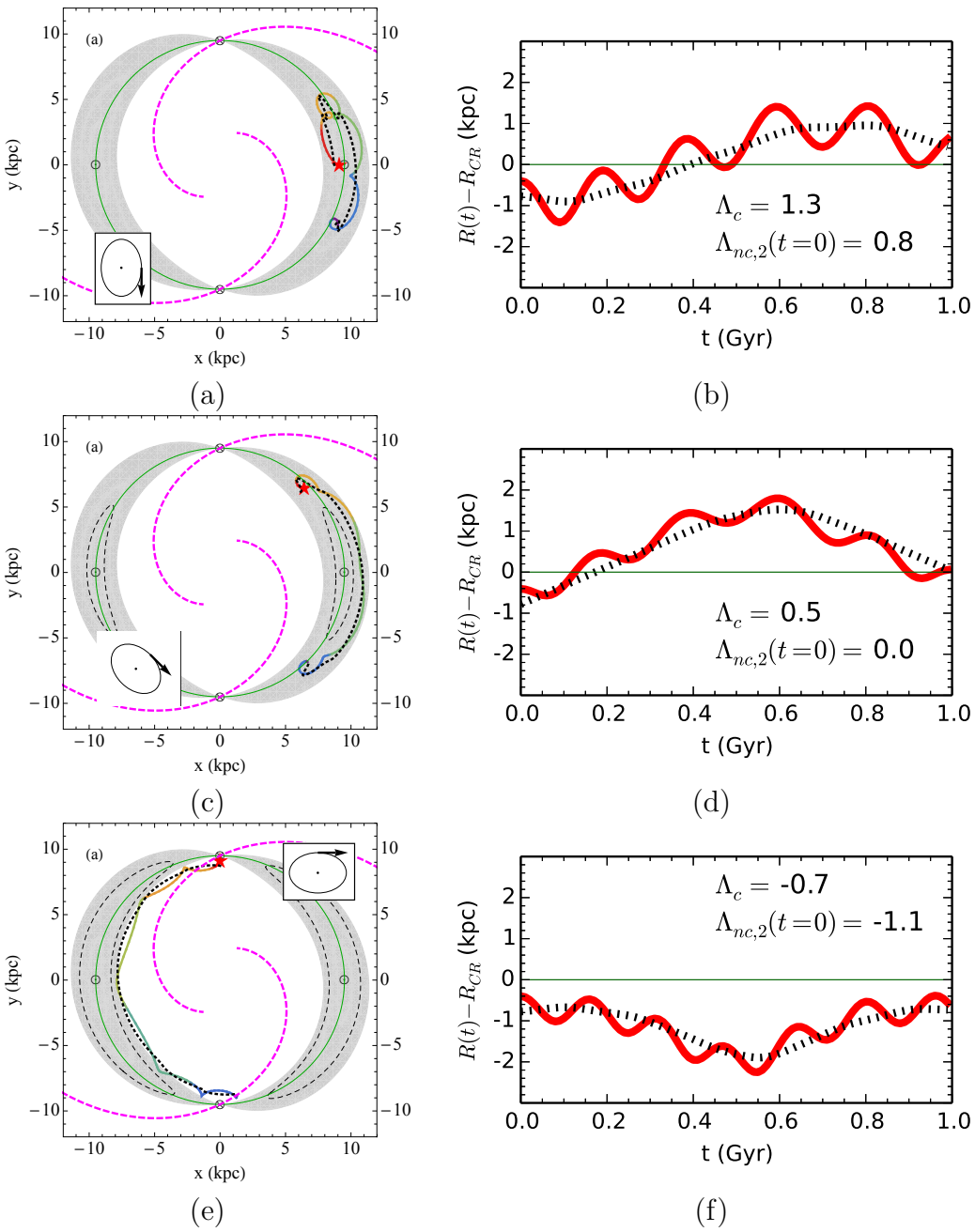

Figure 4.6: The panels and plotted colors and curve patterns have the same meaning as in Figure 4.3. Initial conditions are modified so that $m = 2$, $R_{CR} = 9.5$, $v_{ran,0,\phi} = -10$ km s^{-1} and from top to bottom $\phi_{1,0} = \{0, \pi/4, \pi/2\}$. Each particle is launched at $R_0 = 9.1$ kpc, the apocenter of its epicycle. The top and middle panels show a star that is in a trapped orbit, and the bottom panels show a star that is not in a trapped orbit.

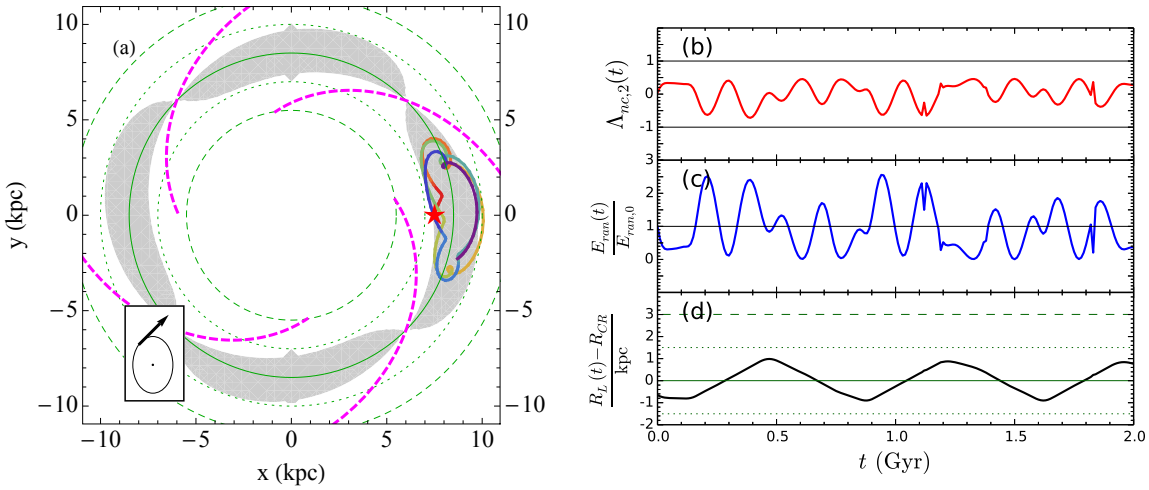

(a) (b)

Figure 4.7: Orbital properties of a star particle launched at 1 kpc inside corotation with $(v_{ran,R,0}, v_{ran,\phi,0}) = (10, 10)$ km s^{-1} ($R_{L,0} = 7.8$ kpc) in a potential modified from Figure 4.3 so that $R_{CR} = 8.5$ kpc. Panel (a) is the same as in Figure 4.3. Panel (b) shows $\Lambda_{nc,2}(t)$ as a solid red line. The horizontal, grey lines at 1 and -1 are the upper and lower limits for $\Lambda_{nc,2}(t)$ for the star to be in a trapped orbit. Note that the star is in a trapped orbit for the entire integration and therefore $|\Lambda_{nc,2}(t)| < 1$ at all times. Panel (c) shows the ratio $(E_{ran}(t)/E_{ran,0})$ as a solid, blue line. Panel (d) shows $(R_L(t) - R_{CR})$ [kpc] as a solid, black line. In panels (a) and (d), the dashed and dotted dark-green curves show the Lindblad resonances (equation 4.31) and the ultra-harmonic Lindblad resonances (equation 4.32), respectively. This star is in a trapped orbit.

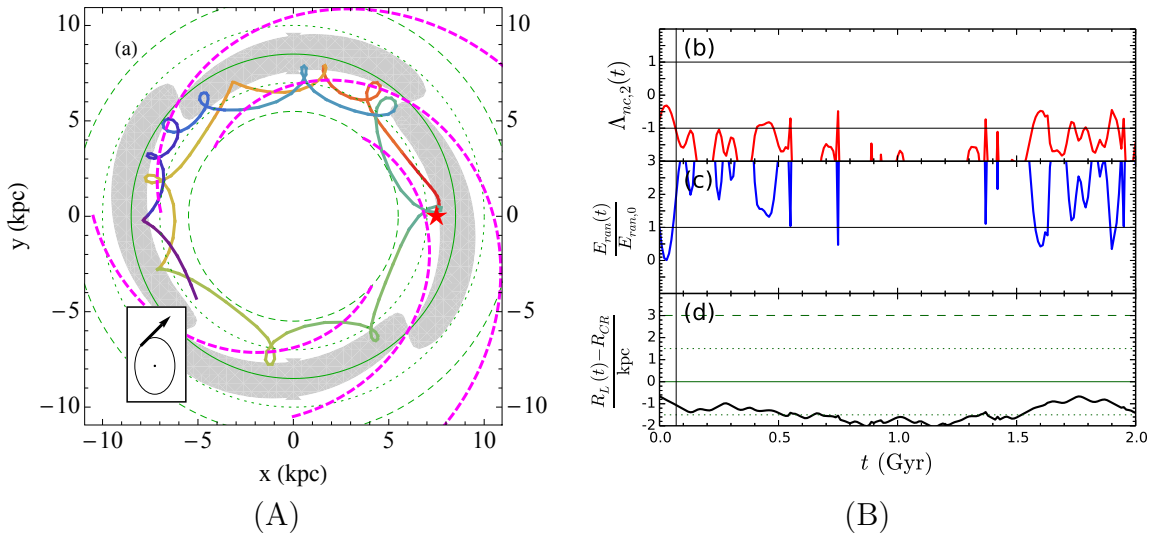

(A) (B)

Figure 4.8: Panels as in Figure 4.7. Orbital properties of a star particle with the potential modified from that in Figure 4.7 so that $R_{CR} = 8$ kpc. The radial coordinate of the star at $t = 0$ is 1 kpc inside corotation and its guiding center radius is $R_{L,0} = 7.3$ kpc. This star is initially in a trapped orbit, but as $E_{ran}(t)$ increases, the star scatters early in the integration interval such that $\Lambda_{nc,2}(t) < -1$ marked with vertical line and is no longer in a trapped orbit likely corresponding to the star's close approach to the spiral arm away from corotation.

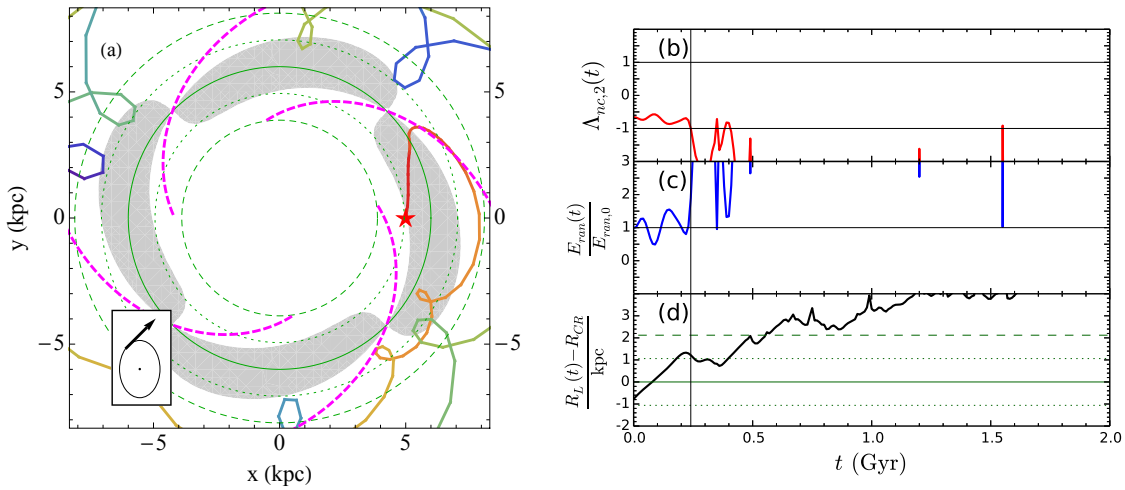

Figure 4.9: Panels as in Figure 4.7. Orbital properties of a star particle with initial conditions modified from those in Figure 4.7 so that $R_{CR} = 6$ kpc. The test particle is launched 1 kpc inside corotation and its guiding center radius is at $R_{L,0} = 5.2$ kpc. This star initially meets the capture criterion, but rapidly scatters when the star's guiding center radius crosses the first ultra-harmonic outer Lindblad resonance. A vertical line indicates the time when the star is no longer captured in a trapped orbit.

Chapter 5

The Amplitude of Radial Excursions

The RMS change in orbital angular momentum for a single transient spiral due to radial migration depends on the amplitude of radial excursions for stars in trapped orbits. The analytic amplitude for radial excursions used in the literature (Sellwood & Binney, 2002, their equation 12) is based on a 2D weak bar potential and otherwise circular orbits (zero random orbital energy) (Binney & Tremaine, 2008; Sellwood & Binney, 2002). The radial excursions in the limit of zero random orbital energy can be taken to approximate a parent orbit, defining the orbital path of the guiding center for stars with some finite random orbital energy.

We briefly summarize the derivation of the amplitude for radial excursions of stars with zero random orbital energy in the presence of a 2D bar, but refer the

reader to Binney & Tremaine (2008), Sellwood & Binney (2002) and the discussion in Appendix A.1 for a more thorough treatment.

Assume a small perturbation in the total potential, such that $\Phi(R,\phi) = \Phi_0(R) + \Phi_1(R,\phi)$ and $|\Phi_1/\Phi_0| \ll 1$. In Binney & Tremaine (2008) (Chapter 3.3b), they show a derivation for the 1^{st} order amplitude radial oscillations about corotation, $R_1(t)$ ($R = R_{CR} + R_1(t)$). They find that the oscillatory behavior about the maximum in the effective potential (see Figure 2.1) obeys,

$$R_1 = \frac{2R_{CR}\Omega_{CR}}{(\kappa^2 - 4\Omega_{CR}^2)}\sqrt{E_p + p^2\cos(2\phi_1)} \tag{5.1}$$

where ϕ_1 is the azimuthal excursion from the local maximum, E_p is the total energy associated with the oscillatory behavior in the rotating frame (equation A.1) and p is the potential amplitude associated with the oscillatory behavior (equation A.2). (see also Binney & Tremaine, 2008, eqn. 3.157)).

Sellwood & Binney (2002) used this derivation, in conjunction with horseshoe orbit theory, to describe the radial migration of stars in the presence of transient spiral structure. Assuming stars are in an extreme trap (ie. $E_p \ll p^2$), Sellwood & Binney (2002) drop E_p and find that a first order radial excursion for stars in a disk with a flat rotation curve is proportional to the square root of the amplitude of the perturbing

potential (Sellwood & Binney, 2002, their equation 12)

$$\Delta R_{max} = 2\sqrt{\frac{|\Phi_b|}{AB}} \tag{5.2}$$

where A and B are Oort's constants for galactic shear

$$A \equiv -\frac{1}{2} R \frac{d\Omega}{dR} \tag{5.3}$$

and vorticity

$$B \equiv -(\Omega + \frac{1}{2} R \frac{d\Omega}{dR}). \tag{5.4}$$

The derivation of equation 5.2 assumes that the random orbital energy of the oscillating star is negligible and that the bar is perpendicular to the direction of circular motion. The oscillatory changes in orbital angular momentum of a star in a trapped orbit are driven by the torque induced by the perturbation to the underlying potential. If a perturbation is in the form of a spiral, rather than a bar, then the strength of the torque must scale with the pitch angle (θ) of the spiral arm. The assumption of a bar (Sellwood & Binney, 2002; Binney & Tremaine, 2008) implies that the torque provided by the potential perturbation is maximized.

5.1 Analytic Evaluation of the Radial Excursions from a Spiral

Trapped orbits can be induced by low pitch angle spiral perturbations, but since the capture region is small for low amplitude spiral patterns (see equation 3.4 to relate pitch angle to the size of the capture region in our model, §4.1.1), the maximum amplitude for changes in guiding center radii (and therefore orbital angular momenta) are expected to be small.

We assume the potential described in §3.1. In the rotating frame, the motion of a star in a trapped orbit can be approximated by the time dependent coordinates $R = R(t) = R_{CR} + R_1(t)$ and $\phi = \phi(t) = \phi_{max} + \phi_1(t)$. We derive the equations of motion in the rotating frame from the Lagrangian,

$$\begin{aligned} \ddot{R} + (\kappa^2 - 4\Omega_{CR}^2)R_1 - 2R_{CR}\Omega_{CR}\dot{\phi_1} &= -\left(\frac{\partial \Phi_1}{\partial R}\right)_{CR} \\ &= \Phi_s \frac{\alpha}{R_{CR}} \sin[\alpha \ln R/R_{CR} + -m\phi(t) + m\Omega_p t]_{CR} \end{aligned} \tag{5.5}$$

and

$$\begin{aligned} \ddot{\phi_1} + 2\Omega_{CR}\frac{\dot{R_1}}{R_{CR}} &= -\frac{1}{R_{CR}^2}\left(\frac{\partial \Phi_1}{\partial \phi}\right)_{CR} \\ &= -\Phi_s \frac{m}{R_{CR}^2} \sin[\alpha \ln R/R_{CR} + -m\phi(t) + m\Omega_p t]_{CR} \end{aligned} \tag{5.6}$$

By adopting the same order of magnitude assumptions as Binney & Tremaine

(2008) for a bar, where $\Phi_s \propto \epsilon$, $\phi_1 \propto 1$ and $R_1 \propto \epsilon^{1/2}$, and time derivatives are multiplied by $\epsilon^{1/2}$, we arrive at the same result (eqn.5.1) modified by $\sqrt{\tan\theta}$ in the final term,

$$R_1 = \frac{2R_{CR}\Omega_{CR}}{(\kappa^2 - 4\Omega_{CR}^2)}\sqrt{E_p + p^2\cos(2\phi_1)\tan\theta} \tag{5.7}$$

However, it is not clear that these assumptions are valid for a spiral pattern, because the geometry of trapped orbits induced by a bar pattern is different from that induced by a low to moderate pitch angle spiral pattern. Indeed, as long as the pitch angle is small, R_1 can be solved explicitly. We show this below.

Integrating equation 5.6 over time gives the following equation:

$$\dot{\phi_1} + 2\Omega_{CR}\frac{R_1}{R_{CR}} = -\Phi_s\frac{m}{R_{CR}^2}\int dt\sin[-\phi_1(t)] \tag{5.8}$$

In order to continue, we must assume a form for $\phi_1(t)$. Contopoulos (1973, 1978) found that most stars in trapped orbits in a perturbed 2D disk librate in the rotating frame in banana shaped orbits on Gyr time-scales. The frequency of oscillation for these orbits is given by (Contopoulos, 1973),

$$\omega^2 = \frac{4|\Phi_s|(4\Omega_{CR}^2 - \kappa_{CR}^2)}{R_{CR}^2(\kappa_{CR}^2 - |\Phi_s|k^2)} \tag{5.9}$$

where $|\Phi_s|$ is the amplitude of the perturbation (given by equation 3.4 in our model). A star that is in a stable trapped orbit will librate about the local maximum in

the effective potential with period, $P = 2\pi/\omega$. Trapped orbits are unstable in the case that the value of the period is less than zero. The highest amplitude azimuthal excursion for a star in a trapped orbits cannot exceed the distance between the local minima on either side of the local maximum. To first order assumption, azimuthal excursions can therefore be described by,

$$\phi_1(t) = |\phi_1| \cos(\omega t + \delta) \tag{5.10}$$

where the amplitude $|\phi_1| = 2\pi/m$ in an m-armed spiral pattern. We here assume the phase constant $\delta = 0$. This sinusoidal approximation becomes less appropriate for increasing values for the spiral pitch angle as high pitch angle spiral patterns diverge from the underlying assumption of near axisymmetry for a spiral density wave.

We plug equation 5.10 into equation 5.8 to get,

$$\dot{\phi_1} + 2\Omega_0 \frac{R_1}{R_0} = -\Phi_s \frac{m}{\omega R_0^2} \int d\tau \sin(-|\phi_1| \cos\tau) \tag{5.11}$$

where $\tau = \omega t$. Equation 5.11 can be explicitly solved from the expansion of $\sin x$,

$$\sin x = \sum_{k=0}^{\infty} \frac{(-1)^k \, x^{1+2k}}{(1+2k)!} \tag{5.12}$$

so,

$$\sin(-|\phi_1| \cos\tau) = \sum_{k=0}^{\infty} \frac{(-1)^{1+k} \, |\phi_1|^{1+2k} \, \cos^{1+2k}\tau}{(1+2k)!}. \tag{5.13}$$

The integral,

$$\int d\tau \sin(-|\phi_1| \cos\tau) = \sum_{k=0}^{\infty} \frac{(-1)^{1+k} |\phi_1|^{1+2k}}{(1+2k)!} \int d\tau \cos^{1+2k}\tau \tag{5.14}$$

has the solution,

$$\int d\tau \sin(-|\phi_1| \cos\tau) = \sum_{k=0}^{\infty} \frac{(-1)^{k} |\phi_1|^{1+2k} \cos^{2+2k}\tau}{(2+2k)!} \, {}_2F_1[\frac{1}{2}, 1+k; 2+k; \cos^2\tau] \tag{5.15}$$

where the hypergeometric function ${}_2F_1$ is defined as

$${}_2F_1(a,b;c;z) = \sum_{n=0}^{\infty} \frac{(a)_n (b)_n}{(c)_n} \frac{z^n}{n!} \tag{5.16}$$

and

$$(x)_n = \begin{cases} 1 & \text{if } n = 0 \\ x(x+1)...(x+n-1) & \text{if } n > 0 \end{cases} \tag{5.17}$$

Keeping the first two terms of order $\sin\tau$ of the integral series we find equation 5.11 becomes,

$$\begin{aligned} \dot{\phi_1} &\approx \frac{m}{R_{CR}^2 \omega} \Phi_s \sin\tau \left(|\phi_1| - \tfrac{|\phi_1|^3}{3!} + ... \right) - 2\Omega_p \tfrac{R_1}{R_{CR}} \\ &\approx \frac{m}{R_{CR}^2 \omega} \Phi_s \sin\tau \sin|\phi_1| - 2\Omega_p \tfrac{R_1}{R_{CR}} \end{aligned} \tag{5.18}$$

Plugging this result into equation 5.5, we find that a star in a trapped orbit will have

radial excursions that follow,

$$R_1 \approx \frac{\Phi_s}{R_{CR}(\kappa^2 - \omega^2)} \left\{ -\alpha \sin(|\phi_1| \cos\tau) + 2m\frac{\Omega_p}{\omega} \sin\tau \sin|\phi_1| \right\} \tag{5.19}$$

The first term in equation 5.19 arises from the radial force associated with the radial gradient in the effective potential near the local maxima. It represents a trapped orbit's diversion from circular around these maxima. The second term comes from the time integral of the azimuthal force, aka. the impulse or change in orbital angular momentum. This change in orbital angular momentum becomes the dominant term in determining maximum radial excursions for a trapped orbit as the pitch angle of the spiral pattern increases.

The maximum radial excursions for stars in trapped orbits, $R_{1,max,EOM} = \max(R_1)$, predicted by our derivation via the equations of motion (equation 5.19), give significantly smaller values than those predicted by the accepted approximation, $R_{1,max,SB02} = \Delta R_{max}/2$ (equation 5.2). In Figure 5.1, we compare the maximum radial excursions for $R_{1,max,EOM}$ (solid, black) and $R_{1,max,SB02}$ (dashed, red) for several select cases. The amplitude of the potential in all cases is given by equation 3.4. For illustrative purposes, we show the expected radial excursions due to epicyclic motion (dotted, blue), where we approximate this as $R_{1,epi} = \sqrt{2}\sigma_R/\kappa$. We adopt the same exponential radial velocity dispersion profile described for Model $f_G(\sigma_R \propto e^{-R/R_\sigma})$ (see §6.3.1 for a detailed description). In Figure 5.1, we show the resulting curves for models

that adopt the potential from §3.4 with values for the model parameters given in Table 3.1, a fractional amplitude for the spiral surface density $\epsilon_\Sigma = \{0.1, 0.3, 0.5\}$, and spiral pitch angle $\theta = \{7°, 12°, 20°, 30°\}$. The radial excursions given by $R_{1,max,EOM}$ for stars in trapped orbits (recall, this can be taken to approximate the guiding center radius for a trapped orbit) are less than or equal to excursions expected from epicyclic motions ($R_{1,epi}$) for low to moderate pitch angle spirals. On the other hand, the radial excursions given by $R_{1,max,SB02}$ are greater than $R_{1,epi}$ in all but the weakest amplitudes for the spiral perturbation. Note that trapped orbits with values for $R_{1,max,EOM} \leq 0$ are not stable.

5.2 Important Observational Constraints

Observations of external galaxies find a range in pitch angle, θ, between 8° and 49°, with median $\theta_{med} = 8° - 22°$ (Ma et al., 1999; Block & Puerari, 1999; Seigar & James, 1998). The spiral arms in our own Milky Way appear to be of intermediate type between grand design and flocculent (Elmegreen, 1998) with pitch angles found to be between 12° (Vallée, 2002, 2015) and 18° (Drimmel, 2000). This is in agreement with the mean pitch angle, $\langle\theta\rangle = 15°$, found for a sample of 51 MW-like (Sbc type) galaxies (Ma et al., 1999).

It is difficult to determine the fractional amplitude of the surface density of an observed spiral pattern, ϵ_Σ. Assuming density change in the galactic disk goes as the

near infrared surface brightness, Rix & Zaritsky (1995) find $m = 2$ Fourier amplitudes between ~ 0.15 and ~ 0.6. Elmegreen et al. (1999, 2011) extend this analysis to define the fractional amplitude (ϵ_Σ) of the spiral arms by assuming a sinusoidal variance in the azimuthal direction. They find, $\epsilon_\Sigma = (I_{max}/I_{min} - 1)/(I_{max}/I_{min} + 1)$ where $I_{max}/I_{min} = 10^{A_r/2.5}$ and A_r is twice the Fourier amplitude. As discussed below, optically identified flocculent spirals have low density near infrared perturbations (if any), with ϵ_Σ between 0.15 and 0.26 (Elmegreen et al., 1999, 2011). Elmegreen et al. (2011) used 46 galaxies from the Spitzer Survey of Stellar Structure in Galaxies (S^4G) to illustrate a trend in spiral amplitude with type. They found that grand design, intermediate and flocculent galaxies have an average $\langle\epsilon_\Sigma\rangle = 0.25 \pm 0.09$, 0.16 ± 0.06 and 0.15 ± 0.07 respectively, with the fractional amplitude, ϵ_Σ, increasing with Hubble type. For Sb type galaxies, like the MW, $\epsilon_\Sigma = 0.24$, 0.16 and 0.10. These values are less than the values typically adopted in this work.

Flocculent spirals are not associated with large amplitude density disturbances as are grand design spirals (Elmegreen & Elmegreen, 1984; Elmegreen et al., 2003, 2011), but have colors and pitch angles consistent with star formation regions that have been sheared to create short spiral-like structures (Elmegreen & Elmegreen, 1984). The mechanism for radial migration via such sheared spirals is not true radial migration in the sense described by Sellwood & Binney (2002) where the perturbation has a single pattern speed. Rather, sheared perturbations follow $\Omega_p(R) \propto \Omega$. In agreement with the discussion in §4.5, Grand et al. (2012) find that a *strong* spiral

perturbation where $\Omega_p(R) \propto \Omega$ produces large amplitude excursions. However, as flocculent spirals do not likely represent strong perturbations in the potential, it is probable that the radial migration induced by flocculent spirals is insignificant.

Grand design spirals have the largest pitch angles and the strongest perturbing potentials. However, grand design spirals (stimulated by external interactions and/or a bar) are likely stable modes (e.g. Elmegreen & Elmegreen, 1984), estimated to have lifetimes on the order of several Gyr (e.g. Elmegreen & Elmegreen, 1983; Struck et al., 2011). This is an important point, as multiple transient spiral patterns with a large range in pattern speeds are necessary for radial migration to effectively mix the galactic disk at all radii.

The above is an important exercise for understanding the realistic efficiency of radial migration in MW-like galaxies. The observed pitch angle values for MW-like galaxies suggest that the changes in guiding center radii (and thus orbital angular momentum) around the radius of corotation are well described by the low pitch angle regime (equation 5.19). A low pitch angle lessens the value of the amplitude of the spiral amplitude, $|\Phi_s|$, thus decreasing the range of values of orbital angular momentum and energy that meet the capture criterion. In Chapter 6, we discuss how the amplitude of the spiral potential affects the fraction of stars in trapped orbits.

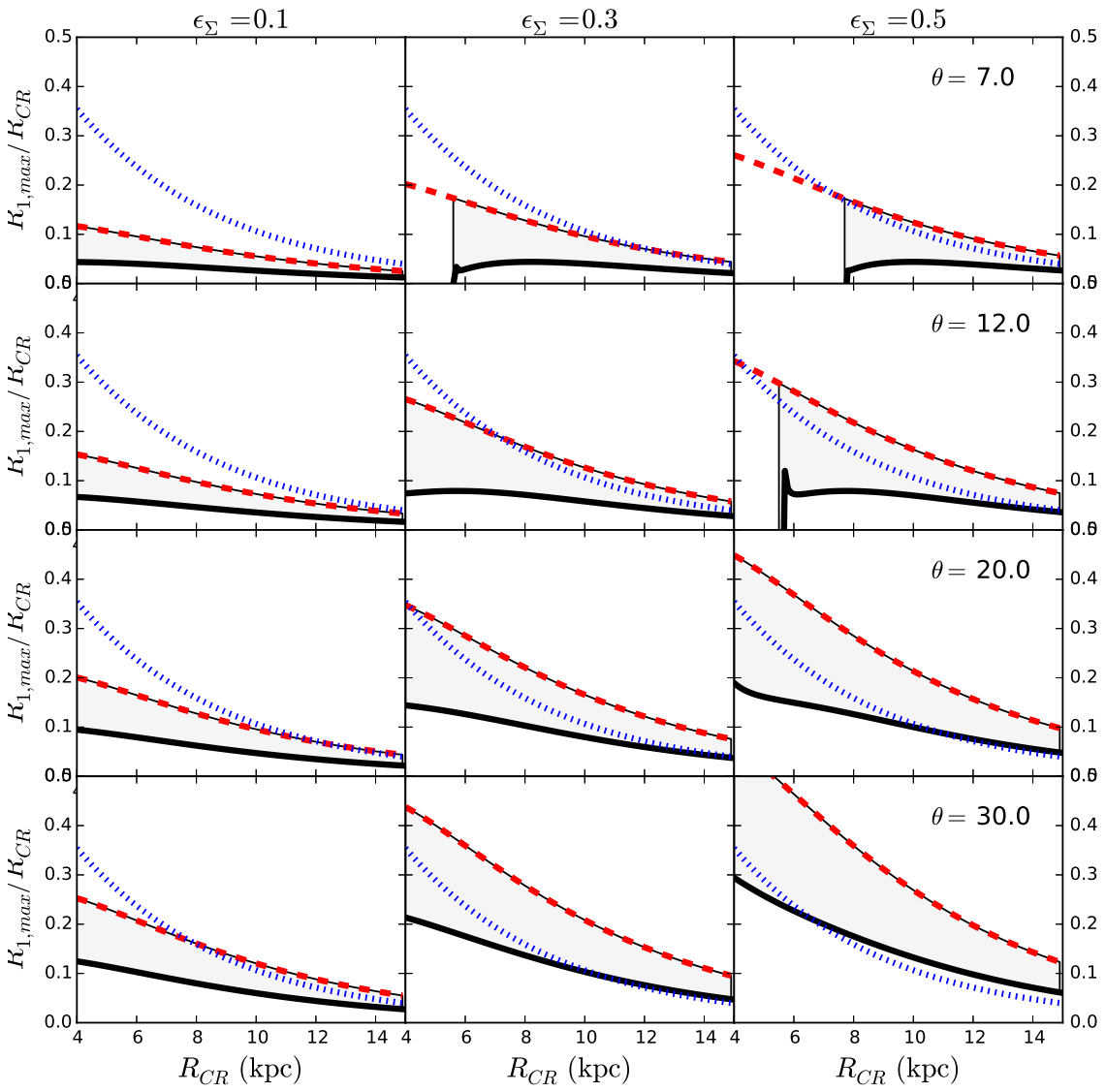

Figure 5.1: Maximum radial excursions for stars in trapped orbits evaluated by equation 5.19, $R_{1,max,EOM} = \max(R_1)$ (solid, black), and equation 5.2, $R_{1,max,SB02} = \Delta R_{max}/2$ (dashed, red). Also shown for comparison are the expected radial excursions from epicyclic motion (dotted, blue). We show the resulting curves for models that adopt the potential from §3.4 with values for the model parameters given in Table 3.1, a fractional amplitude for the spiral surface density $\epsilon_\Sigma = \{0.1, 0.3, 0.5\}$, and spiral pitch angle $\theta = \{7°, 12°, 20°, 30°\}$.

Chapter 6

Modeling the Distribution of Trapped Orbits

The radial migration of an ensemble of disk stars due to a *single* transient spiral pattern is most efficient when the RMS change in the orbital angular momenta of those stars, over the spiral lifetime, is maximized. The efficiency of radial migration, and thus its importance to disk evolution, is therefore directly related to the fraction of disk stars that are initially in trapped orbits. Should multiple transient spiral patterns with a random distribution of pattern speeds, and thus corotation radii, occur over the lifetime of the disk, and should radial migration be efficient for each spiral pattern, the resulting radial migration of stars could have a substantial influence the chemical, kinematic and structural evolution of the disk (Sellwood & Binney, 2002; Schönrich & Binney, 2009a; Roškar et al., 2008; Loebman et al., 2011; Berrier & Sellwood,

2015).

In Chapter 4, we derived an analytic "capture criterion" to determine whether or not a given disk star is in a trapped orbit. In this chapter, we apply our capture criterion to a model of a disk galaxy with the aim to isolate and examine the physical parameters of a populations of stars that determine the distribution and fraction of stars in trapped orbits. We model each disk with an exponential surface density profile (equation 3.11) and a spiral potential (§3.1), where the phase space distribution of stars is described by one of several chosen distribution functions (§3.2). Unless otherwise stated, we used parameter values listed in Table 3.1 when a quantitative analysis is required. Figure 6.1 illustrates the capture region for this specific spiral pattern as a shaded region outlined with a thick, black line. The contours of the effective potential, Φ_{eff}, are shown as thin lines. The peaks of the spiral perturbation are indicated by thick, dashed (magenta) curves.

The capture criterion can be applied to any disk star given its 4D phase space coordinate (R, ϕ, v_R, v_ϕ), the amplitude of the spiral perturbation to the potential at the radius of corotation, $|\Phi_s|_{CR}$, and the slope of the rotation curve at the radius of corotation (equation 4.24). We here adopt a flat rotation curve ($\beta = 2$) and therefore use the form of the capture criterion from equation 4.27. The reader should note that while it is both informative and convenient to express the capture criterion in terms of orbital energy and orbital angular momentum, it requires we adopt a relation between these values and action variables. Equation 4.27 assumes the epicyclic approximation,

which describes mildly non-circular orbits as simple harmonic oscillations about a circularly orbiting guiding center.

At any given position in the disk, the width of the velocity distribution for a stellar population is characterized by the velocity dispersion, σ. A stellar *population* that has a high value for the velocity dispersion has high random energy. Should the ratio of the velocity dispersion to the circular velocity (σ/v_c) be large, the population is kinematically hot. The guiding center radius (R_L from equation 2.5) of a star, and its orbital angular momentum, is determined by its radial coordinate (R) and azimuthal velocity (v_ϕ). Thus for a disk with a given surface density profile and rotation curve, the velocity dispersion is the observable related to the distribution of individual orbital angular momenta of stars that compose the population. This chapter is dedicated to understanding how the random orbital energy of a population relates to the fraction of disk stars that satisfy the capture criterion.

6.1 The Approach

In the method described below, we solve numerically for the fraction of stars in trapped orbits given a particular disk potential and form for the distribution function.

The numerical integration is carried out as follows – At a given radial coordinate (R), we integrate the distribution function over azimuth (ϕ) and the range of velocity values ($\mathbf{v}$) that satisfy the capture criterion (equation 4.27). We set the absolute

upper and lower limits of integration in velocity space to be ± 100 km s^{-1} from the value of $\mathbf{v}$ that corresponds to the peak value of $f(\mathbf{v})$. The solution to this integral, divided by the same integral over all values (not just those that meed the capture criterion), is the fraction of stars in trapped orbits at radius R. We calculate the fraction of stars in trapped orbits for all radial positions between $R_{CR} \pm 4$ kpc in $dR = 0.1$ kpc intervals for each choice of initial conditions. We thus find the radial distribution for the fraction of stars in trapped orbits.

We perform all integrations using the *Wolfram Mathematica v.8.0.4.0* software function `NIntegrate` with the parameters `AccuracyGoal` set to 8 significant digits and `MinRecurrsion` set to 8. We chose the values of these parameters to ensure convergence to a solution within a reasonable amount of time.[1]

The method outlined above calculates the fraction of stars that meets the capture criterion for a given model (i.e. choice for the distribution function and adopted potential). It is known that transient spirals change the distribution function that describes the stellar disk (e.g. Carlberg & Sellwood, 1985; Berrier & Sellwood, 2015), that the amplitude of the spiral perturbation must fluctuate in order for stars to migrate radially (Sellwood & Binney, 2002), and that stars which initially ($t = t_0$) meet the capture criterion (equation 4.27) may be scattered out of trapped orbits (at some time $t > t_0$) even when the spiral potential has constant amplitude (§4.4.3). In this chapter we do not evaluate the time evolution of the captured fraction (see

[1]This is on order of an hour of computing time per set of initial conditions with a 1.8 GHz processor.

§6.4 for further discussion), and therefore refer to the fraction of stars that meets the capture criterion for a given model as the "initial" fraction ($t = t_0$). The initial fraction is equal to the instantaneous fraction of stars that could migrate radially should the perturbation be transient.

Our primary focus here is to understand the relationship between the fraction of stars initially in trapped orbits and the stellar velocity dispersion (σ) for the population. In the process we explore how the fraction of stars in trapped orbits within a chosen radial range depends on the functional form of the distribution function and the parameters values of the spiral potential.

6.2 Trapped Fraction for a Constant Radial Velocity Dispersion

In this section, we assume the phase space distribution function $f_G(\mathbf{x}, \mathbf{v})$ (equation 3.12, described in §3.2.1), a radial velocity dispersion (σ_R) that is constant at all radii, and a fixed ratio of radial and azimuthal velocity dispersions, σ_ϕ/σ_R (equation 3.8). In the next section (§6.3), we explore other prescriptions for the distribution of stars in phase space and allow the velocity dispersion to vary with radius. Under the assumption that a population is characterized by a constant velocity dispersion, we are able to isolate and evaluate how asymmetric drift affects the fraction of stars in trapped orbits.

Asymmetric drift refers to the observed shift in the mean azimuthal velocity of a stellar population (v_a), as well as a skew in its velocity distribution toward slower rotation, with increasing velocity dispersion (e.g. Dehnen & Binney, 1998). It is described by the radial Jeans equations for an axisymmetric disk (Binney & Tremaine, 2008, §4.8.2a) as arising from the balance between rotational and pressure support within the system (a kinematically heated population rotates more slowly). It may be conceptually understood as resulting from the non-circular motions of stars in a disk with surface density increasing toward the galactic center. In such a scenario, a sample of stars at a given radial coordinate will contain more stars with guiding center radii toward inner disk that are near the apocenter of their orbits (and thus have slower rotation due to conservation of orbital angular momentum) than stars from the outer disk that are near pericenter.

6.2.1 Radial Distribution of the Fraction of Stars in Trapped Orbits

The fraction of stars in trapped orbits will be radially dependent. In Figure 6.2, we present two examples of a contour map of $f_G(\mathbf{v})_{\mathbf{x}}$. Each map is for a different radial coordinate (given in the inset), while the azimuthal coordinate in both maps is taken to be at an azimuthal maximum in the same effective potential. We have assumed the radial velocity dispersion is $\sigma_R = 35$ km s^{-1}, setting the azimuthal lag

due to asymmetric drift to be $v_a \approx 15$ km s^{-1} (see equation 3.9). The contour maps are presented in random velocity space (related to velocity space by equation 3.7) and are masked so that only the region of random velocity space that satisfies the capture criterion (equation 4.27, at $t = 0$) are shown. The trapped fraction at each coordinate is given in the inset.

The range of values for the random velocity in the azimuthal direction ($v_{ran,\phi}$, and thus v_ϕ) that satisfies the capture criterion is sensitive to the value of the radial coordinate, R, since whether or not a star meets the capture criterion is primarily a function of orbital angular momentum ($L_z \propto R\, v_\phi$). The range of values for the random velocity in the radial direction ($v_{ran,R}$, and thus v_R) that satisfies the capture criterion is comparatively broad and insensitive to the coordinate at which the capture criterion is evaluated. In Figure 6.3, we show the distribution of random velocities in the azimuthal direction ($v_{ran,\phi}$) only for the same model and spatial coordinates used for the right hand side of Figure 6.2, where the radial velocity is set to be zero, $v_{ran,R} = 0$. Each curve represents the velocity distribution for a stellar population characterised by a value for the radial velocity dispersion (σ_R) that ranges between $5-80$ km s^{-1}, in 5 km s^{-1} increments. The case where the radial velocity dispersion is the same as in Figure 6.2 ($\sigma_R = 35$ km s^{-1}) is shown as a black line. The shaded area of Figure 6.3 indicates the range of azimuthal velocities that meet the capture criterion. Note that as the radial velocity dispersion increases, the peak of the azimuthal velocity distribution shifts toward slower rotation (due to asymmetric drift), affecting the

fraction of that population that meets the capture criterion at a given coordinate. Each curve also represents the distribution of guiding center radii (R_L – and thus orbital angular momentum); therefore, the peak in the orbital angular momentum distribution shifts toward lower orbital angular momentum with increasing radial velocity dispersion.

In order to to derive the capture criterion in equation 4.27 (§4.3), we used the epicyclic approximation. The epicyclic approximation inherently assumes that non-circular motions can be described as small oscillations about a guiding center and therefore is valid for the low random velocity regime. Although we tested and found the capture criterion to be robust for orbits with random velocities up to ~ 50 km s^{-1}, we have not thoroughly tested it above this threshold. We find the high velocity dispersion regime to be instructive, but these model realizations should be taken with caution. For this reason we use either shading or thin lines to indicate model realizations that use radial velocity dispersion $\sigma_R > 50$ km s^{-1} in figures in this chapter.

Figure 6.4 shows the fraction of stars in trapped orbits, at a range of radial coordinates, as a function of the radial velocity dispersion, σ_R, for the same model used in Figure 6.2 (the potential is described in §3.1 with parameters set to the values listed in Table 3.1 and the distribution function described in §3.2.1). As we are interested in understanding how asymmetric drift affects the radial distribution of trapped stars, we ignore the effects of asymmetric drift in the left-hand panel by

setting $v_a = 0$, thus forcing the mean azimuthal velocity to equal the circular velocity ($\langle v_\phi \rangle = v_c$). In the panel on the right we include the prescription for asymmetric drift described above so that $\langle v_\phi \rangle = v_c - v_a$. Each curve represents the fraction of stars in trapped orbits as a function of radius for a value of the radial velocity dispersion (σ_R) that ranges between $5 - 80$ km s^{-1}, in 5 km s^{-1} increments.

The fraction of disk stars that meets the capture criterion at a given coordinate is dependent on the velocity dispersion, which is a measure of the random energy of the stellar *population*.[2] In the limiting case that $\sigma_R \to 0$, all orbits approach circular (in an axisymmetric potential), $R \to R_L$ for all stars, and $v_a \to 0$. The radial distribution of the fraction of stars in trapped orbits saturates at 100% near corotation since these stars meet the capture criterion (primarily determined by their guiding center radii, R_L from equation 2.5). At radii far from corotation, stars do not meet the capture criterion and the fraction of stars in trapped orbits goes to zero. In comparison, a population of stars with finite velocity dispersion has a range of values in its orbital angular momentum distribution at any given coordinate. Note that the surface density is fixed while the radial velocity dispersion is treated as a variable input condition between realizations of our model. We are therefore implicitly making changes to the orbital angular momentum distribution between realizations. Figures 6.2 & 6.3 show that the fraction of stars that meets the capture criterion at a given coordinate depends on the velocity dispersion. With increasing values for

[2]This statement should not be confused with the fact that whether or not an individual *disk* star is in a trapped orbit is largely independent of its random orbital energy (§4.3 & §4.4.2).

the velocity dispersion, the effects of including (or not) a prescription for asymmetric drift in our evaluation of the fraction of stars in trapped orbits becomes important. A prescription for the velocity distribution ($f_G(\mathbf{v})_\mathbf{x}$) at a given radius R that ignores asymmetric drift will have a distribution in guiding center radii (R_L) that peaks at R. When asymmetric drift is included, high velocity dispersion populations have a distribution of guiding center radii that shifts toward the galactic center at any given radius; therefore, the peak of the distribution of stars that meets the capture criterion (R_{peak}) shifts to a radius greater than the corotation radius ($R_{peak} > R_{CR}$). It follows that, with increasing values for the velocity dispersion, the fraction of stars in trapped orbits decreases for all coordinates within the capture region and the radial range within which stars are in trapped increases. The shift in the location of the peak of the radial profile, R_{peak}, towards larger radius reflects the fact that the ratio of the initial fraction of stars in trapped orbits that have $R > R_{CR}$ to $R < R_{CR}$ increases with increasing velocity dispersion. This is discussed in more detail below.

The radial position of the peak of the distribution of the fraction of stars in trapped orbits (R_{peak}) is set by the velocity distribution (and thus the distribution of guiding center radii). Our prescription for the velocity distribution at any given coordinate ($f_G(\mathbf{v})_\mathbf{x}$) is a Gaussian with peak azimuthal velocity set to v_a (equation 3.9). In the case that all phase space coordinates are valid (i.e. without placing bounds via the capture criterion), R_{peak} is the radius at which a star with mean azimuthal velocity $\langle v_\phi \rangle = v_c - v_a$ has a guiding center radius at corotation ($R_L = R_{CR}$). Therefore

R_{peak} can be determined by the relation $R_{peak}\,\langle v_\phi \rangle = R_{CR}\,v_c$. We derive the following equation for the radial offset between the radius of corotation and the radius at which the distribution of the fraction of stars in trapped orbits peaks,

$$R_{peak} - R_{CR} = R_{CR}\left(\frac{v_c}{v_c - v_a} - 1\right) \tag{6.1}$$

Equation 6.1 well describes our model as long as the peak in the velocity distribution at corotation meets the capture criterion. Should the value of the radial velocity dispersion be greater than some critical value, σ_{crit}, the shift in the azimuthal velocity distribution due to asymmetric drift at the radius of corotation would cause the peak in the distribution of guiding center radii (at corotation) to be closer to the galactic center than the innermost radial range of the capture region (R_{min}). Given our prescription for asymmetric drift (equation 3.9) and the relation $R_{min}\,v_c = R_{CR}\,\langle v_\phi \rangle$, we quantify this limit as,

$$\sigma_{crit} = \sqrt{80\,\mathrm{km\,s^{-1}}\,v_c\left(1 - \frac{R_{min}}{R_{CR}}\right)} \tag{6.2}$$

At this limit ($\sigma_R > \sigma_{crit}$), the distribution of the fraction of stars in trapped orbits is dominated by the tail of the velocity distributions from radial coordinates within the capture region, and by velocity distributions with a broad range of velocities from radial coordinated outside the capture region. Thus, the shift in the peak of

the distribution of stars in trapped orbits ($R_{peak} - R_{CR}$) plateaus at a radius nearly[3] equal to the maximum radial range of the capture region. In the top, right panel of Figure 6.5, we plot our approximation for $R_{peak} - R_{CR}$ (equation 6.1) as a dashed (red) curve against data from all realizations of our model. The critical velocity dispersion, σ_{crit} is shown as a thin, vertical line.

6.2.2 The Integrated Fraction of Stars in Trapped Orbits

We henceforth call the total initial fraction of a stellar population that is in trapped orbits the "integrated fraction", $\mathcal{F}_{\Delta R}$. The fraction of stars initially in trapped orbits is a function of radius (see Figure 6.4), and it is therefore valuable to understand how the integrated fraction scales with the size of the radial range. We define the radial range (ΔR) within which we evaluate the integrated fraction ($\mathcal{F}_{\Delta R}$) using five different radial restrictions. Two of the measures, $\mathcal{F}_1$ and $\mathcal{F}_2$, have fixed radial range and evaluate the fraction of stars in trapped orbits within an annulus defined by (1) $R_{CR} \pm 0.5$ kpc (ΔR_1) and (2) $R_{CR} \pm 1$ kpc (ΔR_2). We also apply radial restrictions that may not center on corotation. These are the radial ranges within which the fraction of stars in trapped orbits in every annulus of width dR (given in Table 3.1) is (3) $> 5\%$ ($\Delta R_{5\%}$), (4) $> 25\%$ ($\Delta R_{25\%}$) and (5) greater than half the

[3] As the capture region and the velocity distributions each have some width, the transition between these two regimes is not abrupt.

maximum fraction captured (ΔR_{FWHM}). The radial ranges defined by each of these criteria are shown as functions of the radial velocity dispersion in the middle panels of Figure 6.5. The lower panels of Figure 6.5 show the curves for the integrated fractions $\mathcal{F}_1$, $\mathcal{F}_2$, $\mathcal{F}_{5\%}$, $\mathcal{F}_{25\%}$, and $\mathcal{F}_{FWHM}$ that correspond to evaluation of the integrated fraction within radial ranges ΔR_1, ΔR_2, $\Delta R_{5\%}$, $\Delta R_{25\%}$, and ΔR_{FWHM}. For reference, we use a horizontal, dashed (dark-green) line to show the distance between the Lindblad resonances (radii at which equation 4.31 holds), and a horizontal, dotted (dark-green) line to show the ultra-harmonic Lindblad resonances (the radii at which equation 4.32 holds) in the middle panels of Figure 6.5.

Measures of $\mathcal{F}_{\Delta R}$ are valid in cases where scattering is not important within the associated radial region, ΔR (see §4.4.3 and §6.4, for a thorough discussion). Note that $\Delta R_{5\%}$ (long-dashed, orange), $\Delta R_{25\%}$ (dashed, green) and ΔR_{FWHM} (dot-dashed, black) can be quite large. A star in a trapped orbit that is distant from the capture region has large excursions from its guiding center and thus samples a large fraction of the disk potential. In a realistic disk, such a trajectory would likely lead to scattering via interactions with inhomogeneities in the disk potential that are associated with objects such as dark matter substructure and giant molecular clouds. When modeling radial migration in the disk, one should also take care that the choice for ΔR is less that the radial distance between spiral arms (here $\lambda(R) = 2\pi/k(R)$). Recall, the various curves for $\mathcal{F}_{\Delta R}$ represent the *initial* integrated fraction of stars in trapped orbits within ΔR. The time dependent nature of the integrated fraction of stars in

trapped orbits will be discussed in more detail in future work (see Chapter 8).

At low velocity dispersion, the radial range ΔR_1 (solid, red) is on the order of the radial range where the fraction of stars in trapped orbits approaches 100%. There is therefore a plateau at $\mathcal{F}_1 = 100\%$ in Figure 6.5 in the low velocity dispersion regime. Likewise, when including a prescription for asymmetric drift, there is not a measurable shift in the peak of the distribution of stars in trapped orbits ($R_{peak} - R_{CR}$) at low velocity dispersion since there is a range of radii centered around corotation for which the trapped fraction is 100% in this regime (top, right panel of Figure 6.4).

At high velocity dispersion, there is a noticeable difference between the radial ranges (ΔR) plotted in the left and right hand side of the middle panels in Figure 6.5. When asymmetric drift is ignored, the radial ranges with unconstrained size (i.e. $\Delta R_{5\%}$, $\Delta R_{25\%}$ and ΔR_{FWHM}) grow with growing velocity dispersion. When asymmetric drift is included, these radial ranges decrease in size when $\sigma_R \gtrsim \sigma_{crit}$, and the peak of the distribution of guiding center radii at corotation no longer meets the capture criterion (see equation 6.2). In this high velocity dispersion regime the radial distributions of the fraction of stars in trapped orbits decrease at all radii with increasing velocity dispersion (Figure 6.4), and consequently the radial ranges that have unconstrained size decrease. There is a corresponding decrease in the integrated fraction for $\mathcal{F}_{5\%}$, $\mathcal{F}_{25\%}$, and $\mathcal{F}_{FWHM}$. Since $\mathcal{F}_1$ and $\mathcal{F}_2$ are both evaluated with a smaller radial range than the unconstrained measures of ΔR and have set radial ranges that are centered on the radius of corotation, their values decline more

rapidly with increasing velocity dispersion at $\sigma_R \gtrsim \sigma_{crit}$. It is important to note that the measures ΔR_1 and ΔR_2 are both smaller than the maximum radial range of the capture region in this model. Should they be larger than the maximum range of the capture region, the decrease in the values of $\mathcal{F}_1$ and $\mathcal{F}_2$ with increasing velocity dispersion would be less rapid (as on the left hand side of Figure 6.5).

The radial mass profile for stars in trapped orbits is calculated using the adopted exponential radial surface density profile, where we assume solar mass for all stars. We evaluate the ratio of the mass initially in trapped orbits with radial positions inside corotation ($R < R_{CR}$) to those with radial positions outside corotation ($R > R_{CR}$), and we denote this ratio, $(M_{in}/M_{out})_R$, with the subscript R. Figure 6.6 shows $(M_{in}/M_{out})_R$ adopting the requirements for $\mathcal{F}_1$ and $\mathcal{F}_2$ as thin curves with line styles that correspond to those used in Figure 6.5. We also show $(M_{in}/M_{out})_R$ for the integrated fraction measured over the disk from $R = 0$ to 20 kpc as a long-dashed (black) curve.

The ratio $(M_{in}/M_{out})_R$ is informative about the distribution of stars in trapped orbits, but should not be interpreted as the ratio of stars that could migrate outward versus inward. This is because a star that has radial position outside corotation ($R > R_{CR}$) may have a guiding center radius that is inside corotation ($R_L < R_{CR}$), and vice versa. Indeed, it is the guiding center radius (R_L) of a star in a trapped orbit that oscillates about corotation. The ratio of stellar mass initially in trapped orbits with guiding center radii inside corotation ($R_L < R_{CR}$) to the initial mass

of stars in trapped orbits with guiding center radii outside corotation ($R_L > R_{CR}$), $(M_{in}/M_{out})_L$, is denoted with the subscript L. This ratio is a measure of the initial mass that may migrate outward to inward. In Figure 6.6, $(M_{in}/M_{out})_L$ for $\mathcal{F}_1$, $\mathcal{F}_2$, and over the whole disk are plotted as thick lines with line style coded to correspond to those used for $(M_{in}/M_{out})_R$. Whether or not asymmetric drift is included in our model, $(M_{in}/M_{out})_L > 1$ for all σ_R, reflecting the initial distribution of orbital angular momentum around corotation in our model.

In the left panel of Figure 6.6, where $\langle v_\phi \rangle = v_c$, the mass ratio $(M_{in}/M_{out})_R$ is slightly greater than unity for all velocity dispersions, where the curve that includes the entire disk (long-dashed, thin, black) increases gradually with increasing velocity dispersion. This is simple to understand as the distribution of the fraction of stars in trapped orbits is symmetric about the radius of corotation. The increase in surface density toward the galactic center is small over the ranges sampled by ΔR_1 and ΔR_2, leading to $(M_{in}/M_{out})_R \gtrsim 1$. For the curve that includes the entire disk, the radial range of the fraction of stars in trapped orbits increases with increasing velocity dispersion and therefore the mass ratio $(M_{in}/M_{out})_R$ will increase due to the surface density profile. The increase in all measures of $(M_{in}/M_{out})_L$ with increasing velocity dispersion in the left panel of Figure 6.6 reflects the distribution of orbital angular momentum in the disk. The surface density of stellar guiding centers increases toward the galactic center (we give a more thorough discussion of the orbital angular momentum distribution in §6.3.2).

In the right panel of Figure 6.6, where $\langle v_\phi \rangle = v_c - v_a$, the distributions for $(M_{in}/M_{out})_R$ and $(M_{in}/M_{out})_L$ diverge. For increasing values of the velocity dispersion greater than the low velocity dispersion regime (discussed above), the location of the peak of the radial distribution of stars in trapped orbits (R_{peak}) shifts to radii greater than corotation ($R_{peak} > R_{CR}$), it follows that there is more mass initially in trapped orbits has $R > R_{CR}$ than $R < R_{CR}$, and $(M_{in}/M_{out})_R < 1$. However, the mass ratio $(M_{in}/M_{out})_L$ increases with increasing velocity dispersion. We illustrated in Figure 6.3, that the distribution of guiding center radii (and thus the distribution of orbital angular momentum) at any given coordinate shifts to lower values with increasing velocity dispersion. Therefore, within the ranges given by ΔR_1 and ΔR_2, there is more stellar mass that meets the capture criterion with $R_L < R_{CR}$ than with $R_L > R_{CR}$; this ratio increases with increasing shift in the orbital angular momentum distribution at any given coordinate due to asymmetric drift.

It is informative to consider the mass ratio around corotation over a disk. In the case of an exponential surface density profile (equation 3.11), the total mass is given by,

$$M_{tot} = \int_0^\infty \Sigma(R')\, R'\, dR'\, d\phi' = 2\pi\Sigma_0 R_d^2. \tag{6.3}$$

The mass inside the radius of corotation is

$$M_{in} = \int_0^{R_{CR}} \Sigma(R')\, R'\, dR'\, d\phi' = M_{tot}\,[1 - e^{-b}(b+1)], \tag{6.4}$$

where $b = R_{CR}/R_d$ is the ratio of the radius of corotation to the scale length of the surface density of the disk. Similarly, the mass outside corotation is given by

$$M_{out} = \int_{R_{CR}}^{\infty} \Sigma(R')\, R'\, dR'\, d\phi' = M_{tot}\, e^{-b}(b+1). \tag{6.5}$$

The ratio of the mass inside to outside corotation over the disk is then,

$$\left(\frac{M_{in}}{M_{out}}\right)_{tot} = \frac{e^b}{(b+1)} - 1. \tag{6.6}$$

In our model, $b = 8\,\mathrm{kpc}/2.5\,\mathrm{kpc} \approx 3.6$, giving a value for $(M_{in}/M_{out})_{tot} \approx 7.0$. The value of the mass ratio for stars in trapped orbits over the entire disk (long-dashed, black curve in Figure 6.6) does not approach that of the ratio of the total mass, whether or not we include a prescription for asymmetric drift.

6.2.3 The Functional Dependencies of the Integrated Fraction

We are interested in understanding the functional dependence of the integrated fraction of stars in trapped orbits ($\mathcal{F}$) on the radial velocity dispersion (σ_R). To this end we used the function `NonLinearModelFit` from *Wolfram Mathematica*'s built-in library to find the line of best-fit[4] for the decrease in $\mathcal{F}$ with increasing σ_R. We

[4]We set the fit "method" to "Automatic", thus allowing *Mathematica* to select from its library to minimize fitting residuals.

tested linear, exponential, polynomial, and Gaussian functional forms for all cases when asymmetric drift is included. The curves for $\mathcal{F}$ are best fit with a line when $5 \leq \sigma_R \leq 50$ km s^{-1}, so that

$$\mathcal{F} = \xi_\mu \sigma_R + \xi_\beta, \tag{6.7}$$

where the values of the slope (ξ_μ) and y-intercept (ξ_β) are given in Table 6.1. For all tested models ($5 \leq \sigma_R \leq 80$ km s^{-1}) the curves for $\mathcal{F}$ have a best-fit form that follows a Gaussian profile,

$$\mathcal{F}(\sigma_R) = \xi_1 \exp\left\{-\frac{(\sigma_R - \xi_3)^2}{\xi_2^2}\right\}, \tag{6.8}$$

where the values of the fitting constants, ξ_1 (normalization), ξ_2 (standard deviation) and ξ_3 (mean of distribution), are given in Table 6.2. We emphasize that we fit the data with a Gaussian function since it best fits the data; there is not a compelling physical reason these data should follow a Gaussian profile rather than a straight line, or any other functional form. We show best-fit curves for $\mathcal{F}_1$, $\mathcal{F}_2$, and $\mathcal{F}_{FWHM}$ in Figure 6.7 with line styles set to match those of Figure 6.5, and data points for $\mathcal{F}_1$ (diamonds, red), $\mathcal{F}_2$ (squares, blue), and $\mathcal{F}_{FWHM}$ (circles, black) are plotted as symbols. Thick lines represent the best linear fit and thin lines show the best fit with a Gaussian form. We expect the values of the fitting constant, $\xi_{1,2,3}$ and $\xi_{\mu,\beta}$, to be model dependent, and, as we show below, to be some function of the radius of corotation (R_{CR}) and the amplitude of the spiral potential at corotation ($|\Phi_s|_{CR}$).

Table 6.1: Linear best-fit parameters for the integrated fraction of stars in trapped orbits for a restricted range of radial velocity dispersions ($5 \leq \sigma_R \leq 50$ km s^{-1}). Parameter values are given in Table 3.1.

Integrated Fraction $\mathcal{F}_{\Delta R}$	Slope ξ_μ	y-intercept ξ_β
$\mathcal{F}_1$	-1.3	119
$\mathcal{F}_2$	-1.0	100
$\mathcal{F}_{FWHM}$	-0.8	99

Table 6.2: Gaussian best-fit parameters for the integrated fraction of stars in trapped orbits for equation 6.8 for the full set of radial velocity dispersions ($5 \leq \sigma_R \leq 80$ km s^{-1}). Parameter values are given in Table 3.1.

Integrated Fraction $\mathcal{F}_{\Delta R}$	Normalization ξ_1	Standard Deviation ξ_2	Mean ξ_3
$\mathcal{F}_1$	111	73	-12
$\mathcal{F}_2$	97	82	-16
$\mathcal{F}_{FWHM}$	134	138	-78

We expect the integrated fraction of stars in trapped orbits ($\mathcal{F}_{\Delta R}$) to increase with increasing spiral strength ($|\Phi_s|_{CR}$) since the size of the capture region is larger for stronger spiral strengths (see §4.1.1). In our model, spiral strength (equation 3.4) depends on the radius of corotation (R_{CR}), spiral pitch angle (θ), number of spiral arms (m), the surface density profile ($\Sigma(R)$), and the fractional surface density of the spiral potential (ϵ_Σ). In Figure 6.8, we vary the value of the fractional surface density (ϵ_Σ) to show that, for a given velocity dispersion ($\sigma_R = 25$ km s^{-1} in this example), the integrated fraction of stars in trapped orbits ($\mathcal{F}_{\Delta R}$) scales roughly monotonically with the amplitude of the spiral potential at corotation ($|\Phi_s|_{CR}$). A similar relationship is expected for any linear change in the spiral strength (e.g. changes in m or $\tan\theta$). The slopes of $\mathcal{F}(\epsilon_\Sigma)$ in panel (d) of Figure 6.8 suggests that at least one of the values of the fitting constants are indeed dependent on $|\Phi_s|_{CR}$.

Note that panel (c) of Figure 6.8 shows that the radial ranges ΔR_{FWHM} and ΔR_2 are equal at $\epsilon_\Sigma \approx 0.3$ (although ΔR_{FWHM} is centered at R_{peak}, not R_{CR}). Above this threshold in the size of the radial ranges, there is a difference in the shape of the slopes for the integrated fraction ($\mathcal{F}_{\Delta R}$). The measures $\mathcal{F}_1$ and $\mathcal{F}_2$ evaluate the integrated fraction over a fixed radial range and at a fixed position. Thus, $\mathcal{F}_1$ and $\mathcal{F}_2$ increase more rapidly with increasing spiral amplitude than do measures that evaluate the integrated fraction over a range that also increases with spiral amplitude ($\mathcal{F}_{5\%}$, $\mathcal{F}_{25\%}$ and $\mathcal{F}_{FWHM}$). The mass ratio, $(M_{in}/M_{out})_R$, changes from values that are less than one to greater than one with increasing spiral amplitude. This reflects the fact that

with stronger spiral amplitude, the fraction of stars in trapped orbits near corotation approaches saturation at 100%. A similar relationship is shown in Figure 6.6, where the fraction of stars in trapped orbits saturates at low velocity dispersion. The shift in the value of $R_{peak} - R_{CR}$ in panel (b) between 0.2 kpc for $\epsilon_\Sigma \leq 0.3$ and 0.1 kpc for $\epsilon_\Sigma \geq 0.4$ is of order dR (Table 3.1), and is a numerical anomaly.

The prescription for the amplitude of the imposed spiral pattern (equation 3.4) in our model depends on the exponential surface density profile (equation 3.11) and the wave number (equation 3.5) and goes as $\propto R_{CR}\, e^{-R_{CR}/R_d}$. We therefore explore how the fitting parameters ($\xi_{1,2,3}$ and $\xi_{\mu,\beta}$) depend on the radius of corotation (R_{CR}). In Figure 6.9, we set $\sigma_R = 25$ km s^{-1} and $\epsilon_\Sigma = 0.3$ and vary the value of R_{CR}. The shape of the slopes for $\mathcal{F}_{5\%}$, $\mathcal{F}_{25\%}$, and $\mathcal{F}_{FWHM}$ increase toward the galactic center with increasing peak amplitude for the distribution of the fraction of stars in trapped orbits and decreasing radial ranges for evaluation ($\Delta R_{5\%}$, $\Delta R_{25\%}$, and ΔR_{FWHM}). The curves for $\mathcal{F}_{25\%}$ (dashed, green) and $\mathcal{F}_{FWHM}$ (dot-dashed, black) converge at corotation radii distant from the galactic center, as do the corresponding curves for $\Delta R_{25\%}$ and ΔR_{FWHM}. By comparing the shape of these curve to the slightly divergent behavior of the curve for $\Delta R_{5\%}$ (long-dashed, orange), it follows that the convergence of $\Delta R_{25\%}$ and ΔR_{FWHM} is a consequence of the skew in the distribution of the trapped fractions at these radii. At corotation radii $R_{CR} \lesssim 2R_d$,[5] the width of the distribution for the trapped fraction decreases such that the (fixed) radial ranges ΔR_1 and ΔR_2

[5]We do not explore the trapped fraction at $R_{CR}/R_d < 1.5$.

sample a greater portion of the distribution (including the tails of the distribution), leading to a decrease in $\mathcal{F}_1$ and $\mathcal{F}_2$ toward the galactic center. Panel (b) shows that the offset between the radial peak of the distribution of the trapped fraction and the radius of corotation decreases toward the galactic center. Equation 6.1 predicts that the value for $R_{peak} - R_{CR}$ scales as R_{CR}. As in panel (b) of Figure 6.8, we see numerical noise in the curve for $R_{peak} - R_{CR}$ in panel (b) of Figure 6.9 as the changes in the values for $R_{peak} - R_{CR}$ between realizations are less than or on order of dR (Table 3.1). The values for the mass ratio $(M_{in}/M_{out})_R \ll (M_{in}/M_{out})_{tot}$ (equation 6.6) at all radii. While further investigation into fitting $\xi_1 = \xi_1(|\Phi_s|_{CR})$ gave inconclusive results, it is clear that the values of the fitting constants depend on R_{CR}.

In summary, there is a clear trend that the integrated fraction of stars in trapped orbits depends on the velocity dispersion of stars and goes as $\mathcal{F} \propto e^{-\sigma_R^2}$ when fitting all realizations of this model (i.e. $5 \leq \sigma_R \leq 80$ km s^{-1}). The fitting coefficients for equation 6.8 ($\xi_{1,2,3}$) and for the linear model ($\xi_{\mu,\beta}$) depend on parameters that describe the underlying potential (e.g. adopted radius of corotation and spiral strength), but the exact form is unclear and evidently model dependent.

6.2.4 Comparison to Previous Work

The efficiency of radial migration for a single spiral pattern is maximized in the case that the RMS change in orbital angular momentum for the ensemble of stars in trapped orbits, $\langle (\Delta L_z)^2 \rangle^{1/2}$, is maximized over the spiral lifetime. In a simulation

of seven tagged populations of test particles in a Mestel disk with two spiral arms, where each population had a different scale height and initial velocity dispersion, Solway et al. (2012) found that the value for $\langle(\Delta L_z)^2\rangle^{1/2}$ for a given stellar population, decreases exponentially with linearly increasing values for that population's initial velocity dispersion. It is encouraging that we find a similar relationship between the integrated fraction of stars in trapped orbits $\mathcal{F}_{\Delta R}$ and the radial velocity dispersion ($\mathcal{F}_{\Delta R} \propto e^{-\sigma_R}$) in §6.2.2, strengthening the argument that the efficiency of radial migration depends on the velocity dispersion.

It is not obvious how to further compare our results to the trend found by Solway et al. (2012). The value of $\langle(\Delta L_z)^2\rangle^{1/2}$ is a time dependent quantity (thus including the effects of scattering) for the entire population of stars. Solway et al. (2012) measured $\langle(\Delta L_z)^2\rangle^{1/2}$ over the lifetime of the simulation in order to evaluate the final $\langle(\Delta L_z)^2\rangle^{1/2}$ induced by a transient spiral pattern from initial growth through final decay. The value of $\mathcal{F}_{\Delta R}$ is a measure only of the initial fraction of stars that *may* migrate radially. We therefore interpret the fall off in the initial fraction of stars in trapped orbits with increasing velocity dispersion as a first step in isolating the physics important to understanding the value of $\langle(\Delta L_z)^2\rangle^{1/2}$.

Solway et al. (2012) found an exponential fall in $\langle(\Delta L_z)^2\rangle^{1/2}$ with increasing scale height of the test population. In the current study, we cannot make any predictions about whether or not the vertical position or motion of a star affects its trapped status because we have assumed a 2D disk on the premise that vertical action and

radial action are separable (see §3 & §4.1). However, should the ratio σ_R/σ_z be constant, we expect a similar trend in the initial fraction of stars in trapped orbits as in equation 6.8.

6.3 Trapped Fraction for Radially Dependent Velocity Dispersion

In §6.2, we assume that σ_R is independent of radius. This may be a reasonable assumption for the integrated fraction of stars in trapped orbits within a restricted radial range (e.g. ΔR_1 and ΔR_2), but over a large radial range one might prefer to adopt a prescription for the velocity dispersion that is dependent upon radius ($\sigma_R = \sigma_R(R)$). In this subsection, we explore how the initial fraction of stars in trapped orbits depends on the prescription for $\sigma_R(R)$. Throughout this analysis we assume the disk potential described in §3.1 with parameter values given by Table 3.1, unless otherwise stated. We also compare results obtained under the assumption of a Gaussian velocity distribution, f_G (§3.2.1), with those obtained using a modified Shu distribution function, f_{new} (§3.2.2).

Table 6.3: Important parameters for the models presented in §6.3.

Name	*DF*	$\sigma_R(R)$	R_σ
$f_G(\sigma_R \propto e^{-R/R_\sigma})$	f_G	$\Sigma \propto \sigma_R^2$	$2R_d$
$f_G(\sigma_R \propto R\,e^{-R/R_\sigma})$	f_G	$Q = 1.5$	R_d
$f_{new}(\sigma_R \propto e^{-R/R_\sigma})$	f_{new}	$\sigma_R \propto e^{-R/R_\sigma}$	$3R_d$

6.3.1 Prescriptions for the Radial Velocity Dispersion

We use three prescriptions to describe the distribution of stars in the disk. Below we describe each of these and provide an outline of the important parameters (see also Table 6.3).

Our first model, $f_G(\sigma_R \propto e^{-R/R_\sigma})$, uses a prescription for $\sigma_R(R)$ that is based on the theoretical prediction that a locally isothermal, self gravitating disk with scale height independent of radius and with fixed ratio σ_R/σ_z, will have $\sigma_R^2(R) \propto \Sigma(R)$ (van der Kruit & Searle, 1981; Lewis & Freeman, 1989). Given that we have assumed an exponential surface density profile, we adopt $\sigma_R(R) = \sigma_{R,0}\,e^{-R/R_\sigma}$, where $R_\sigma = 2R_d$ and the radial velocity dispersion is normalized such that $\sigma_R(R = 8 \text{ kpc}) = 40$ km s^{-1} in order to approximate solar neighborhood values. In this model, we adopt a Gaussian distribution function, $f_G(\mathbf{x}, \mathbf{v})$ (described in §3.2.1).

In the second model, $f_G(\sigma_R \propto R\,e^{-R/R_\sigma})$, which also uses a Gaussian velocity distribution ($f_G(\mathbf{x}, \mathbf{v})$), we set the Toomre Q parameter (Toomre, 1964) for local

stellar disk stability to 1.5, i.e.,

$$Q \equiv \frac{\sigma_R(R)\,\kappa(R)}{3.36\,G\,\Sigma(R)} = 1.5, \tag{6.9}$$

with the intention of modeling a kinematically warm disk that is locally stable but may support global instabilities at all radii (see Sellwood, 2014b, for a thorough discussion).[6] In a disk with a flat rotation curve, $\kappa(R) \propto R^{-1}$. Therefore, $\sigma_R(R) \propto R\,e^{-R/R_d}$ for constant Q in our model, where the surface density is normalized such that $\Sigma(R = 8 \text{ kpc}) = 50 \text{ M}_\odot \text{ pc}^{-2}$ (Table 3.1).

We construct the third model, $f_{new}(\sigma_R \propto e^{-R/R_\sigma})$, under the assumption of a kinematically warm disk using a modified Shu distribution function, $f_{new}(\mathbf{x}, \mathbf{v})$ (described in §3.2.2). Dehnen (1999b) finds that the radial velocity dispersion profile produced by the second moments of f_{new} may be well approximated by an exponential radial profile, $\sigma_R(R) = \sigma_{R,0}\,e^{-R/R_\sigma}$, where $R_\sigma = 3R_d$. In this model, the value of $\sigma_{R,0}$ is also normalized such that the radial velocity dispersion $\sigma_R(R = 8 \text{ kpc}) = 40 \text{ km s}^{-1}$.

The radial profiles for $\sigma_R(R)$ for each scenario are illustrated in Figure 6.10, together with values for $\sigma_R(R)$ for the MW that are inferred from observation (Lewis & Freeman, 1989; Pasetto et al., 2012). We also plot a curve for a model identical to $f_G(\sigma_R \propto R\,e^{-R/R_\sigma})$, with the exception that we set $Q = 2$ so that the disk is comparatively stable to all instabilities. Note that the shape of the curve for the model of $\sigma_R(R)$

[6] We are interested in modeling a disk that could have transient instabilities at all radii. Sellwood & Carlberg (2014) found that transient *modes* can occur in their N-body simulations even as the disk is heated to $Q > 1.5$ by spiral activity.

where $Q = 2$ is a good fit in the solar neighborhood at latitudes $-0.5 < z \leq -0.3$ kpc below the Galactic plane (magenta, squares) (Pasetto et al., 2012), while shape is not a good fit to the observational data over the disk. The shape of the model with $Q = 1.5$ is a better fit to the data.

6.3.2 Orbital Angular Momentum Distributions

As we showed in Chapter 4, the most important parameter for determining whether or not a star is in a trapped orbit is its orbital angular momentum and thus its guiding center radius. Stars in trapped orbits have guiding center radii that oscillate within the capture region around corotation. In this chapter, we evaluate the initial ($t = t_0$) distribution of stars in trapped orbits, under a set of assumptions (e.g. the velocity dispersion profile) in a given model. At some later time ($t > t_0$), the distribution of guiding center radii, and thus the orbital angular momentum distribution in the disk, may be rearranged via radial migration and scattering (see §4.4.3). It is therefore instructive to explore the differences in the orbital angular momentum distributions for each of our models.

We calculate the initial radial distribution of orbital angular momentum by finding the angular momentum in each annulus, i (with radial size dR, Table 3.1), of the disk using the following equation:

$$L_z(R_i) = \int_{-\infty}^{\infty}\int_{-\infty}^{\infty}\int_{0}^{2\pi}\int_{R_i}^{R_i+dR} f(\mathbf{x},\mathbf{v})\, L_z(R)\, R\, dR\, d\phi\, dv_R\, dv_\phi, \tag{6.10}$$

where $L_z(R) = R\,v_\phi$. The orbital angular momentum in each annulus of an exponential disk with a flat rotation curve that is entirely composed of stars in circular orbits is given by,

$$L_{z,c}(R_i) = 2\pi \int_{R_i}^{R_i+dR} \Sigma(R)\, v_c\, R^2\, dR. \tag{6.11}$$

In Figure 6.11, we show the radial distribution of orbital angular momentum, $L_z(R_i)$, for each model (Table 6.3) normalized by $L_{z,c}(R_i)$ in each annulus. This normalization $(L_z(R_i)/L_{z,c}(R_i))$ is set under the assumption that the integral of each distribution function over velocity space would give a surface density profile that is well approximated by an exponential (equation 3.11), and that is maximised at all radii when $\sigma_R = 0$ (no lag in $\langle v_\phi \rangle$ due to asymmetric drift). Line styles correspond to those used to represent the radial velocity dispersion profiles for each model in Figure 6.10, where thin lines represent regions where the radial velocity dispersion $\sigma_R > 50$ km s^{-1}.

The radial profile for the mean orbital angular momentum goes as $\langle L_z(R) \rangle \propto \Sigma(R) R \langle v_\phi \rangle = \Sigma(R) R (v_c - v_a)$, where $v_a \propto \sigma_R^2$. The lag (v_a) in the mean orbital velocity of a population is described by the radial Jeans equations, showing that populations with higher random energy have a lower azimuthal streaming velocity (see §6.2 for a brief discussion). It follows that the orbital angular momentum distribution for each model shown in Figure 6.13 decreases toward the galactic center as the the velocity dispersion increases. The shape of the normalized orbital angular momentum distributions can therefore be understood by the relative differences in each model's radial velocity dispersion distribution.

The shape of curve for each orbital angular momentum profile, $L_z(R_i)$, also depends on the adopted radial surface density profile. The two models that adopt a Gaussian velocity distribution ($f_G(\mathbf{v})_{\mathbf{x}}$) have, by construction, an exponential surface density profile (equation 3.11), where we have adopted the parameter values given in Table 3.1. Both of these models also have a velocity dispersion profile that goes to zero at large radii, and thus each normalized orbital angular momentum profile converges to unity with increasing radius. An analysis of the robustness of approximating the integral of $f_{new}(\mathbf{x}, \mathbf{v})$ over velocity space, $\Sigma_{new}(R)$, as an exponential with scale length R_d is given by Dehnen (1999b). We note that at radii $R_i/R_d \gtrsim 4$, the surface density profile for $\Sigma_{new}(R)$ has values greater than approximated by the exponential surface density profile used in our normalization and in models that adopt a Gaussian velocity distribution. Consequently, the normalized orbital angular momentum profile for Model $f_{new}(\sigma_R \propto e^{-R/R_\sigma})$ has values greater than unity at $R_i/R_d \gtrsim 4$.

A population characterised by radial velocity dispersion σ_R at radius R, will have a mean azimuthal velocity $\langle v_\phi \rangle$ that lags the circular orbital velocity by v_a. Therefore, the stars that compose that population have a mean guiding center radius that is closer to the galactic center than the coordinate radius, $\langle R_L \rangle < R$. For constant surface density scale length (R_d), populations with higher velocity dispersion have more centrally concentrated guiding center radii. The distribution of stars in trapped orbits depends on the distribution of guiding center radii (and thus orbital angular momenta) near corotation. The value of $(M_{in}/M_{out})_L$ (the ratio of stars in trapped

orbits with guiding center radii inside corotation to those outside corotation) is a measure of the the slope around corotation of the distribution of guiding center radii for stars in trapped orbits. As stated above, this is relevant to understanding the initial ratio of stars that may migrate outward to inward. The ratio $(M_{in}/M_{out})_R$ is a measure of the slope of the radial orbital angular momentum profile for stars in trapped trapped orbits.

6.3.3 Trapped Fraction for a Given Normalization of the Radial Velocity Dispersion

We now focus on how the adopted normalization for a radially dependent radial velocity dispersion profile ($\sigma_R = \sigma_R(R)$) affects the initial fraction of stars in trapped orbits ($\mathcal{F}_{\Delta R}$). The assumed underlying potential is described in §3.1, where the spiral has parameter values given in Table 3.1. In this section we use two models that adopt an exponential radial velocity dispersion profile and which are outlined in Table 6.3: $f_G(\sigma_R \propto e^{-R/R_\sigma})$ and $f_{new}(\sigma_R \propto e^{-R/R_\sigma})$. The radial velocity dispersion ($\sigma_R(R)$) is normalized such that it takes a value between $\sigma_R(R = 8 \text{ kpc}) = \{5,\ 80\}$ km s^{-1}. The results are illustrated in Figure 6.12, where panels show the (a) the radial distribution of the initial fraction of stars in trapped orbits, (b) the distance between the peak of the radial trapped fraction profile and the radius of corotation ($R_{peak} - R_{CR}$) for a given population of stars, (c) the various radial ranges (ΔR) within which the

integrated fraction is evaluated, (d) the integrated fraction ($\mathcal{F}$), and (e) the measures of the two ratios $(M_{in}/M_{out})_L$ and $(M_{in}/M_{out})_R$.

The fractions and distributions of stars in trapped orbits shown in Figure 6.12 have similar characteristics in both cases. As in Figure 6.5, we approximate offset of the peak of the radial distribution of stars in trapped orbits, $R_{peak} - R_{CR}$, in panels (b) with a dashed (red) curve. The radial position of R_{peak} is well approximated by the radius at which a star with mean azimuthal velocity $\langle v_\phi \rangle$ would have a guiding center radius at corotation. At radial velocity dispersions greater than some critical value, σ_{crit} (equation 6.2), the peak of the velocity distribution at corotation does not meet the capture criterion, and equation 6.1 is not a good approximation for $R_{peak} - R_{CR}$. Rather, at $\sigma_R > \sigma_{crit}$, the offset $R_{peak} - R_{CR}$ has a constant value close to the maximum radial distance of the capture region from the radius of corotation.

There is not a significant difference between the plotted profiles for the model using $f_G(\sigma_R(R))$ (Figure 6.12, left-hand side) and the model using $f_G(\sigma_R)$ (Figure 6.5). Both models have assumed $R_{CR} = 8$ kpc and over a small radial distances the value of $\sigma_R(R)$ approaches constant. However, the choice for the distribution function, f_G or f_{new}, does yield important differences. First, the shape of the curves for the integrated fraction ($\mathcal{F}_{\Delta R}$ in panels (d) in Figure 6.12) that are evaluated over a radial range (ΔR) that is held constant (ΔR_1 and ΔR_2 - solid (red) and short-dashed (blue) lines, respectively) diverge between normalizations of the model that use f_G and those that use f_{new} at high values for the radial velocity dispersion. Second, the

ratio $(M_{in}/M_{out})_L$ increases relatively slowly with increasing radial velocity dispersion when using f_{new} compared to normalizations of the model that use f_G. Finally, panels (a) illustrate that with increasing velocity dispersion the radial distribution the fraction of stars in trapped orbits broadens, although from panels (c) it is clear that this broadening is greater when the velocity distribution is determined by $f_{new}(\mathbf{x}, \mathbf{v})$. Each of these differences is linked to how the orbital angular momentum distribution changes as function of the normalization of the radial velocity dispersion between realizations of models using $f_G(\mathbf{x}, \mathbf{v})$ or $f_{new}(\mathbf{x}, \mathbf{v})$ (see below).

Figure 6.13 shows curves for the normalized orbital angular momentum profiles ($L_z(R_i)/L_{z,c}(R_i)$, see equations 6.10 & 6.11) for each model and adopted normalization. As discussed in §6.3.2, the orbital angular momentum in a given annulus depends on both the radial velocity dispersion and surface density profiles. The surface density profile is held constant (equation 3.11) between model normalizations of $f_G(\mathbf{x}, \mathbf{v})$. However, the surface density profile produced by integrating $f_{new}(\mathbf{x}, \mathbf{v})$ over velocity space ($\Sigma_{new}(R)$) diverges from an exponential profile with increasing velocity dispersion (see Dehnen, 1999b, for a thorough analysis). The surface density $\Sigma_{new}(R)$ exceeds that of an exponential at large radii, and leads to values of for the normalized orbital angular momentum profile ($L_z(R_i)/L_{z,c}(R_i)$) that are greater than unity. Additionally, a stellar population at radius R that is kinematically hot will have a slower mean azimuthal velocity, and thus a lower value for the mean orbital angular momentum, than a kinematically cold population. A slower mean azimuthal veloc-

ity at radius R is indicative of a more centrally concentrated distribution of guiding center radii for stars at R. Thus, for a fixed surface density profile, the total orbital angular momentum of the disk increases with decreasing velocity dispersion. As the surface density profile between normalizations of the model that uses $f_{new}(\mathbf{x}, \mathbf{v})$ is not fixed, the slope of the normalized orbital angular momentum profiles are relatively flat.

The total orbital angular momentum of the stellar disk is not constant between models or normalizations. Rather, the total orbital angular momentum of the disk decreases with increasing velocity dispersion as the guiding center radii of stars in the disk become more centrally concentrated. As discussed in §6.3.2, the orbital angular momentum in a given annulus decreases with increasing velocity dispersion for a given surface density profile. Note that the slope of the orbital angular momentum distribution around corotation ($R_{CR} = 8$ kpc in this model) is highly dependent on the normalization for Model $f_G(\sigma_R \propto e^{-R/2R_d})$, and less so for Model $f_{new}(\sigma_R \propto e^{-R/3R_d})$. The radial velocity dispersion in the model that uses $f_G(\mathbf{x}, \mathbf{v})$ increases much more rapidly toward the galactic center than it does in the model that uses $f_{new}(\mathbf{x}, \mathbf{v})$.

In Model $f_{new}(\sigma_R \propto e^{-R/R_\sigma})$, the curves representing the integrated fraction ($\mathcal{F}_{\Delta R}$) and the ratio $(M_{in}/M_{out})_L$ are relatively flat at velocity dispersions higher than the critical velocity dispersion ($\sigma_R > \sigma_{crit}$), while the unfixed radial ranges for evaluation (ΔR) increase with increasing velocity dispersion. This reflects that fact that for increasing velocity dispersion the distribution of guiding center radii remains fixed,

for the modified Shu distribution function ($f_{new}(\mathbf{x}, \mathbf{v})$), even as the radial excursions for stars in the population become large. We also note that the slope for the ratio $(M_{in}/M_{out})_L$ is related to the slope of the orbital angular momentum distribution around corotation (Figure 6.13).

6.3.4 Trapped Fraction for a Given Radius of Corotation

We now explore how the radial distribution for the initial fraction of stars in trapped orbits is a function of the radius of corotation (R_{CR}). In Figure 6.14, we show our findings for the three models outlined in Table 6.3: (1) we adopt $f_G(\mathbf{x}, \mathbf{v})$ with $\sigma_R^2(R) \propto \Sigma(R)$, (2) we adopt $f_G(\mathbf{x}, \mathbf{v})$ with $\sigma_R(R)$ set so that $Q = 1.5$, and (3) we adopt $f_{new}(\mathbf{x}, \mathbf{v})$ with $\sigma_R(R) \propto e^{-R/3R_d}$ (see Dehnen, 1999b, for an interesting discussion). Each model adopts the parameter values in Table 3.1 and $\sigma_R(R)$ is normalized as outlined in §6.3.1.

Recall that the form of the capture criterion used here (equation 4.27) was derived under the assumption of the epicyclic approximation (see discussion in §6.2.1). This criterion was tested and found to be robust for stars with random velocities less than 50 km s^{-1} (§4.4.2). In Figure 6.14, we show the data in regions of the disk where the radial velocity dispersions exceed $\sigma_R > 50$ km s^{-1}, but omit a discussion about trends in this region as any conclusions would be uncertain. However, in §6.4, we

discuss how the integrated fraction may be interpreted in the high velocity dispersion regime.

At all radii of corotation (in regions of the disk where $\sigma_R \leq 50$ km s^{-1}) trends in the integrated fractions, $\mathcal{F}_{5\%}$, $\mathcal{F}_{25\%}$, and $\mathcal{F}_{FWHM}$, and the size of the unconstrained radial ranges for evaluation ($\Delta R_{5\%}$, $\Delta R_{25\%}$, and ΔR_{FWHM}), primarily depend on the adopted radial velocity dispersion profiles for each model. The radial velocity profile for Model $f_G(\sigma_R \propto R\, e^{-R/R_\sigma})$ approaches zero at large radii. Consequently, with increasing radius, the shift in the peak of the distribution of the trapped fraction, $R_{peak} - R_{CR}$, goes to zero, the unconstrained radial ranges converge to the size of the capture region (as most of the stars in trapped orbits are in the capture region), and the integrated fraction corresponding to evaluations that use an unconstrained radial range increase (as most of the stars in that radial range are in trapped orbits). Model $f_{new}(\sigma_R \propto e^{-R/R_\sigma})$ has the most shallow radial velocity dispersion profile, and thus the shape of the curves for $R_{peak} - R_{CR}$, the unconstrained radial ranges for evaluation of the integrated fraction, and the corresponding integrated fractions, are relatively flat.

It has been stated (Roškar et al., 2008; Loebman et al., 2011) that radial migration may play a role in growing the disk. In our models, the ratio $(M_{in}/M_{out})_L$ signifies the initial ratio of stars that may migrate outward (stars with initial guiding center radii *in*side corotation) to stars that may migrate inward (stars with initial guiding center radii *out*side corotation) should the spiral be transient. $(M_{in}/M_{out})_L$ is a mea-

sure of the radial distribution of guiding center radii of stars in trapped orbits, which is in turn a function of the distribution function ($f(\mathbf{x}, \mathbf{v})$), and its moments ($\Sigma(R)$ and $\sigma_R(R)$). In panel (e) of Figure 6.14, we show that in all models tested, more stars are in trapped orbits with guiding center radii *in*side corotation ($R_L < R_{CR}$) than *out*side corotation ($R_L > R_{CR}$), with a higher $(M_{in}/M_{out})_L$ ratio toward the inner disk. We emphasize that the choice of distribution function ($f(\mathbf{x}, \mathbf{v})$) has an important effect on the ratio $(M_{in}/M_{out})_L$ (see §6.3.2 & §6.3.3) for high radial velocity dispersion, $\sigma_R(R)$ (illustrated in Figure 6.10). The implication is that the net change in orbital angular momentum of all stars captured in trapped orbits will be positive should they migrate. This begs the question, what is the source of orbital angular momentum and energy during radial migration? It is likely that this is a multi-parameter problem that may include gas in-fall and motions in the disk (e.g. Roškar et al., 2008; Schönrich & Binney, 2009a). In future work, we will explore how the combination of radial migration and conservation of orbital angular momentum and energy in an isolated disk could lead to spiral disruption (see Chapter 8). Again, one should note that Figure 6.14 is only representative of the *initial* fraction of stars in trapped orbits.

6.4 Discussion

The fraction of stars in trapped orbits at any given coordinate or integrated over the disk is an instantaneous quantity that assumes the imposition of a spiral perturbation did not change the initial phase space distribution function. We here argue that the initial distribution of stars in trapped orbits should be interpreted as an upper limit.

First, $\Lambda_{nc,2}(t)$ is explicitly a time-dependent quantity (equation 4.27). In §4.4.3, we showed that stars which initially met the capture criterion could rapidly be scattered[7] out of a trapped orbit before experiencing a significant change in orbital angular momentum. Scattering events could affect the fraction of stars in trapped orbits over time. This is an especially important point for stars in trapped orbits that have either (1) large radial excursions from the guiding center, since such stars sample a larger fraction of the underlying disk potential and are therefore are more likely to scatter as they encounter inhomogeneities in the disk, or (2) a path for the guiding center radius that crosses a Lindblad resonance. Stars may scatter into or out of trapped orbits due to interactions with inhomogeneities in the potential, but the later type of scattering can only happen when a star is in a trapped orbit. For this reason we expect the integrated fraction to decrease as a function of time, $\partial\mathcal{F}/\partial t \leq 0$. Indeed, Barros et al. (2013) observe a region of decreasing surface density in their test-

[7]We define "scattering" as an event where a star' s change in orbital angular momentum is correlated with a change in random orbital energy, distinct from radial migration.

particle simulation that grows in what appears to be the capture region, consistent with scattering processes. In addition, Berrier & Sellwood (2015) found that transient spiral arms smooth the orbital angular momentum distribution away from corotation, thus lowering the fraction of stars with orbital angular momenta within the capture region.

Second, Carlberg & Sellwood (1985) showed that a rapidly growing spiral perturbation would cause a non-adiabatic response in the stellar disk over a broad radial range and a second order change in the orbital angular momentum distribution (via the action-angle distribution function). As we have shown, a heated population of stars has a lower fraction of stars in trapped orbits. We propose that such heating by the spiral would lead to fewer stars being captured in trapped orbits than would be expected from the initial integrated fraction.

Third, our analysis assumes that all orbits are constrained to a 2D disk. This approximation is valid for stellar orbits that are nearly circular since the vertical and radial actions are separable (this an underlying assumption in the derivation of the capture criterion).[8] A star that has large random motions requires that vertical and radial actions be coupled (and thus the validity of the capture criterion is untested), but perhaps more importantly, it has excursions into the vertical dimension where the azimuthal force from the spiral is weaker.[9] By assuming a 2D disk, we are neglecting vertical motions and thus overestimating how strongly stars in 3D orbits interact with

[8]Indeed, we expect the capture criterion to be less robust for stars with highly non-circular orbits.

[9]The azimuthal force from the spiral pattern is necessary for trapped orbits to exist (Sellwood & Binney, 2002, see §2 and[].

the spiral pattern. The fraction of stars in a disk population that has large random motions increases with increasing velocity dispersion. We therefore expect there is a systematic overestimate of the initial fraction of stars in trapped orbits with increasing velocity dispersion. As mentioned in §6.2.4, Solway et al. (2012) found an exponential decrease in the RMS change in orbital angular momentum for an ensemble of stars due to a transient spiral with increasing scale height of the population.

We defer a more thorough discussion of the time-dependence of the fraction of stars captured in trapped orbits to future work (Chapter 8).

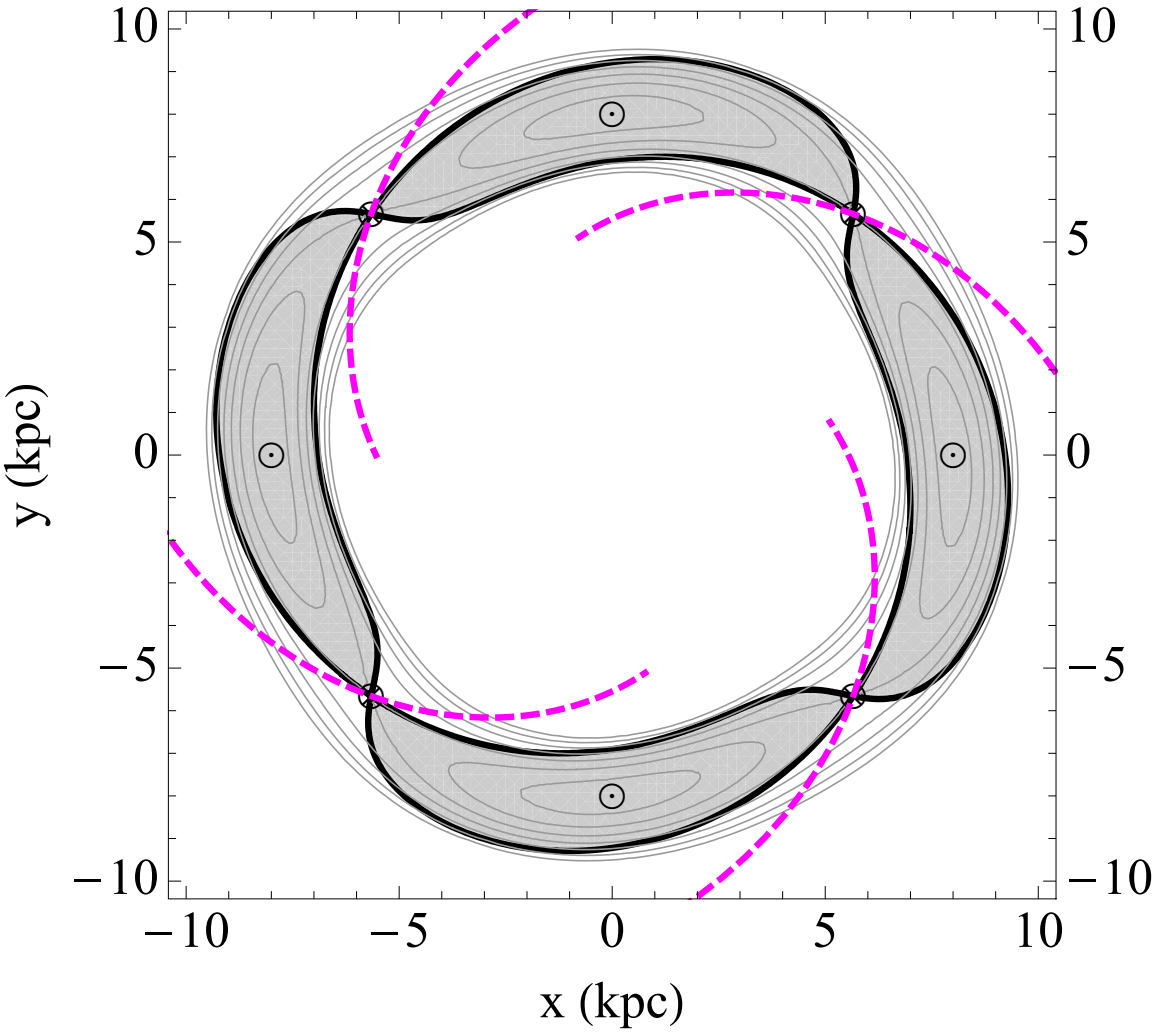

Figure 6.1: Contours of the effective potential, Φ_{eff}, for a trailing spiral pattern with parameter values listed in Table 3.1. The peaks of the spiral perturbation are shown as thick, dashed (magenta) curves. The local maxima in Φ_{eff} (between spiral arms) are marked with the symbol $\odot$ and the saddle points (the deepest part of the spiral potential at corotation) are marked with $\otimes$. The capture region has a thick (black) outline and is shaded grey. The parameter values that produce the capture region and effective potential shown in this figure are used for much of the analysis in this chapter.

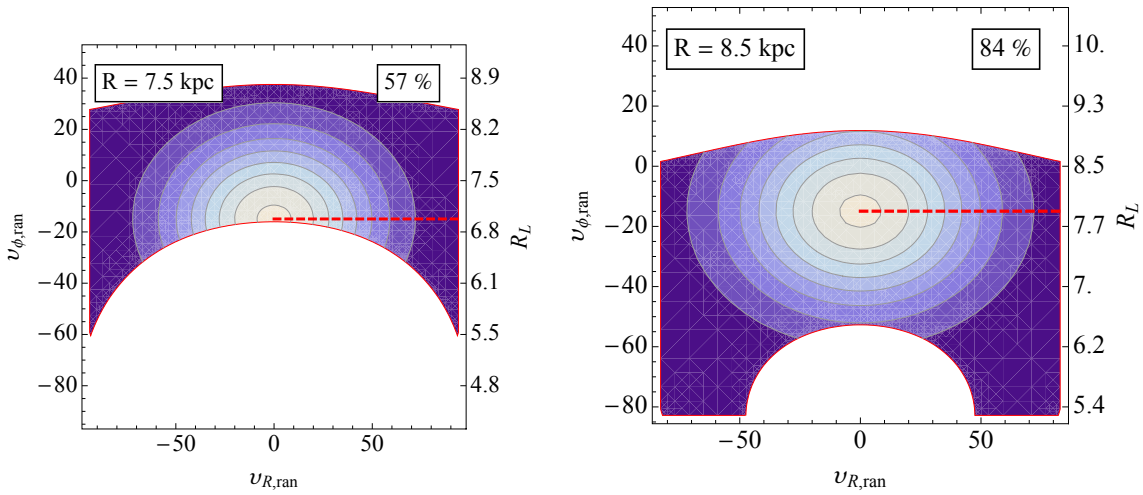

Figure 6.2: Contour maps of $f_G(\mathbf{v})_{\mathbf{x}}$ for two different radial coordinates (in the upper left-hand insets) from the same model. The azimuthal coordinate is set to be at a maximum in the effective potential. The spiral pattern is the same as illustrated in Figure 6.1 with parameter values from Table 3.1. The radial velocity dispersion is $\sigma_R = 35$ km s^{-1}, thus setting the azimuthal lag due to asymmetric drift to be $v_a = \sigma_R^2/(80 \text{ km s}^{-1}) \approx 15$ km s^{-1}. We present the maps in random velocity space (related to velocity by equation 3.7) so that the horizontal axes show the radial random velocity, $v_{ran,R}$ and the left-hand vertical axes show the azimuthal random velocity, $v_{ran,\phi}$. We mask the contour maps so that only the values of $\mathbf{v}_{ran}$ that satisfy the capture criterion (equation 4.27, for $t = 0$) are shown. Note that the random azimuthal velocities that satisfy the capture criterion shift with radial coordinate R, while the capture criterion are much less sensitive to differences in radial velocity. The integrated percent of the distribution that meets this criterion is given in the upper right-hand inset for each case. The right-hand vertical axes show the guiding center radius (R_L) associated with $v_{ran,\phi}$ at R. In each plot we connect the centroid of the velocity distribution to the right-hand axis with a horizontal, dashed (red) line. Due to asymmetric drift, the peak in the random azimuthal velocity corresponds to a guiding center radius that is closer to the galactic center than the coordinate radius.

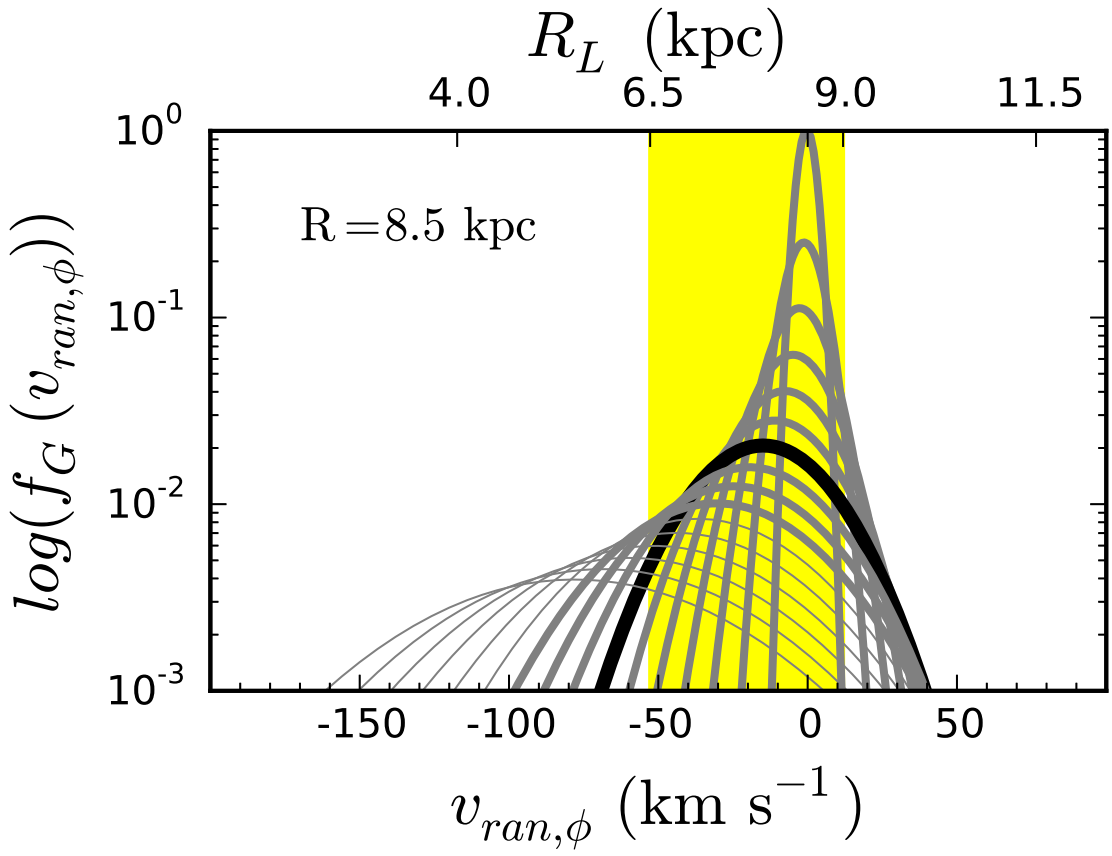

Figure 6.3: Random azimuthal velocity ($v_{ran,\phi}$) distributions assuming the same model and spatial coordinates as in the right hand panel of Figure 6.2. The vertical axis shows the logarithmic value of $f_G(v_{ran,\phi}) = f_G(v_{ran,R} = 0, v_{ran,\phi})_{R=8\text{kpc}}$. Each curve represents the azimuthal velocity distribution for a stellar population characterised by a value for the radial velocity dispersion (σ_R) that ranges between $5 - 80$ km s^{-1}, in 5 km s^{-1} increments. The black line indicates the case where the radial velocity dispersion is the same as in Figure 6.2 ($\sigma_R = 35$ km s^{-1}). The shaded (yellow) area indicates the range of azimuthal velocities that meet the capture criterion. The upper horizontal axis shows the guiding center radius (R_L) associated with $v_{ran,\phi}$. Due to asymmetric drift, the peak in the random azimuthal velocity distribution shifts toward slower rotation with increasing velocity dispersion. In the same manner, the peak of the probability distribution of guiding center radii shifts toward radii that are closer to the galactic center than the coordinate radius, R. Thin lines indicate model realizations that use radial velocity dispersion $\sigma_R > 50$ km s^{-1}.

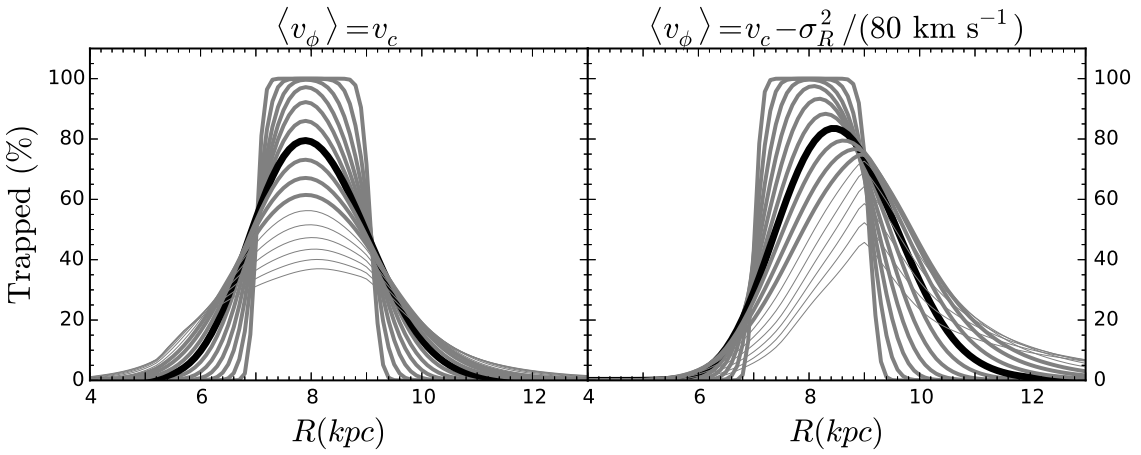

Figure 6.4: Radial distributions for the fraction of stars in trapped orbits for the same model used in Figure 6.2, where we assume a Gaussian velocity distribution (f_G), and he perturbing spiral potential has parameters set to $R_{CR} = 8$ kpc, $m = 4$, $\epsilon_\Sigma = 0.3$, and $\theta = 25°$. Radial velocity dispersions range between $5 \leq \sigma_R \leq 80$ km s^{-1} in 5 km s^{-1} increments. For reference, the radial profile for $\sigma_R = 35$ km s^{-1} is in bold. The panel on the left ignores the lag in mean azimuthal velocity due to asymmetric drift ($\langle v_\phi \rangle = v_c$) and the panel on the right includes a correction that is modeled as a simple offset to the mean azimuthal velocity ($\langle v_\phi \rangle = v_c - \sigma_R^2/(80\ \mathrm{km\ s^{-1}})$). Thin lines indicate model realizations that use radial velocity dispersion $\sigma_R > 50$ km s^{-1}.

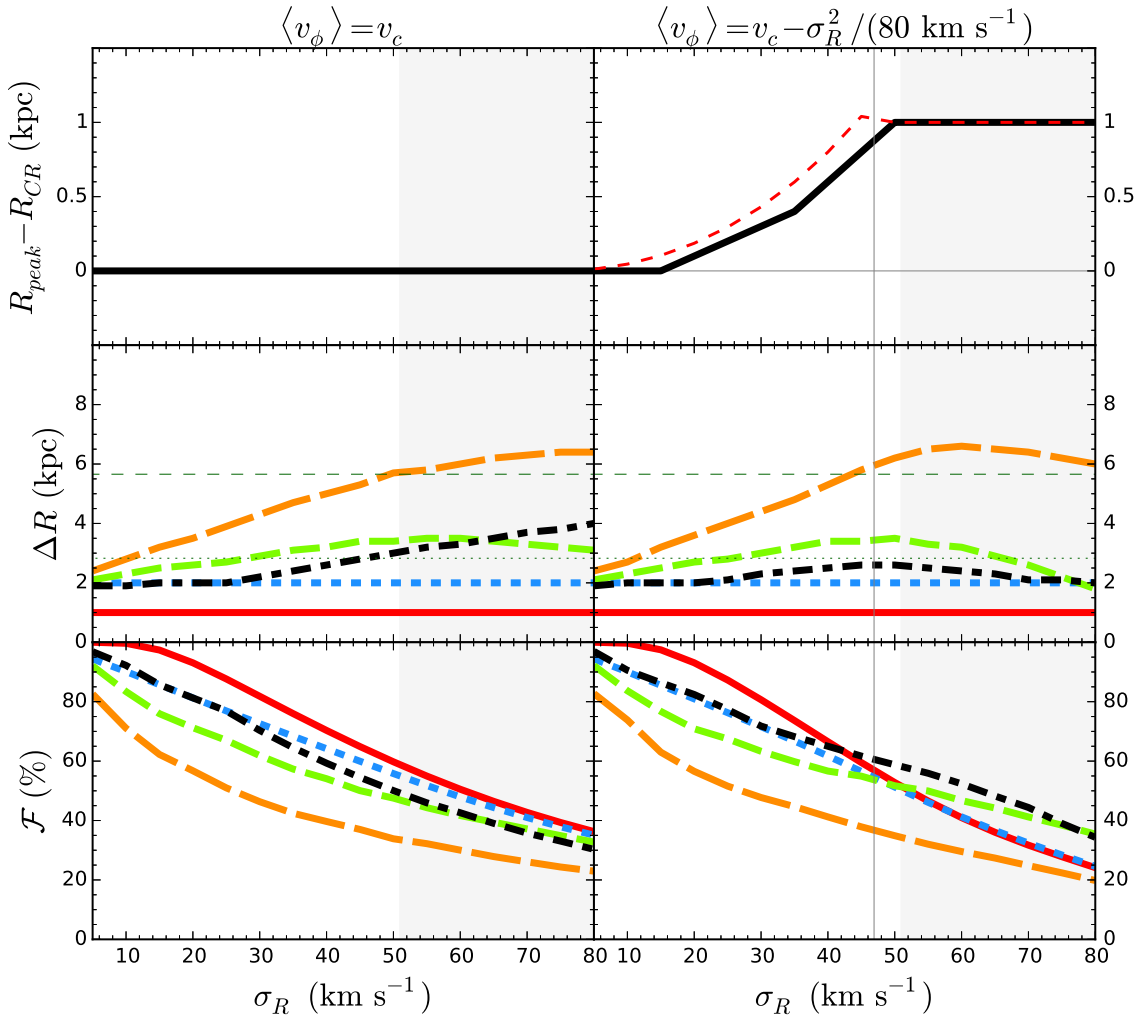

Figure 6.5: The upper panels show the offset of the peak in the radial distribution (from Figure 6.4) for the fraction of stars captured in trapped orbits, $(R_{CR} - R_{peak})$, in solid, black, and the approximated offset as a dashed (red) curve. The middle panels show the radial range (ΔR) used to evaluate the integrated fraction of stars ($\mathcal{F}_{\Delta R}$) for $R_{CR} \pm 0.5$ kpc (ΔR_1) (horizontal, solid, red), $R_{CR} \pm 1$ kpc (ΔR_2) (horizontal, short-dashed, blue), and the radial range within which the annular fraction of stars in trapped orbits is $>$ 5% ($\Delta R_{5\%}$) (long-dashed, orange), $>$ 25% ($\Delta R_{25\%}$) (dashed, green), and greater than half the maximum value (ΔR_{FWHM}) (dot-dashed, black). For reference, the horizontal (dark-green) lines indicate the distances between the Lindblad resonances (dashed) and ultra-harmonic Lindblad resonances (dotted). The bottom panels show the corresponding integrated fraction of stars in trapped orbits, $\mathcal{F}_{\Delta R}$ (in corresponding line styles). As in Figure 6.4, the panels on the left ignore the effects of asymmetric drift. A vertical line indicates the critical velocity dispersion, σ_{crit}. Shaded regions indicate model realizations that use radial velocity dispersion $\sigma_R > 50$ km s^{-1}.

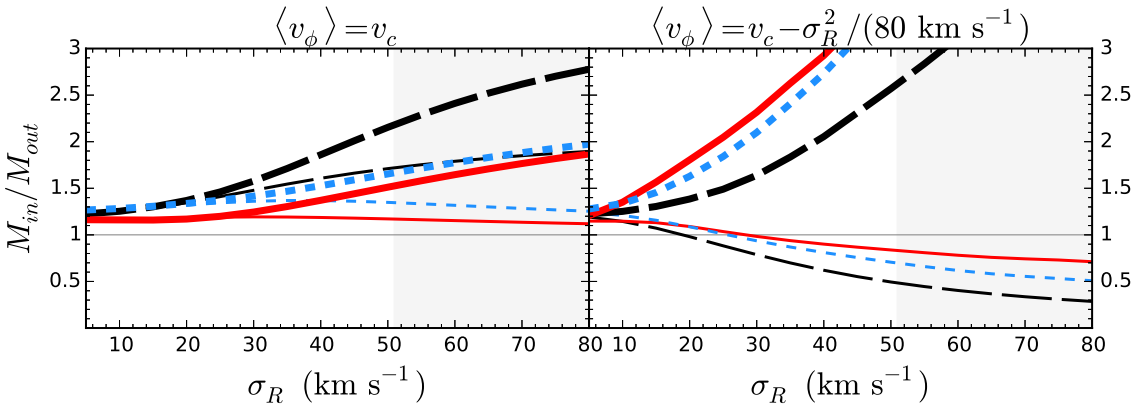

Figure 6.6: The ratio of the trapped mass $(M_{in}/M_{out})_R$ (thin) and $(M_{in}/M_{out})_L$ (thick) for $\mathcal{F}_1$ (solid, red) evaluated within ΔR_1, $\mathcal{F}_2$ (short-dashed, blue) evaluated within $DeltaR_2$, and the integrated fraction evaluated over the disk from $0 < R \leq 20$ kpc (long-dashed, black). The panels on the left ignore the effects of asymmetric drift. Shaded regions indicate model realizations that use radial velocity dispersion $\sigma_R > 50$ km s^{-1}.

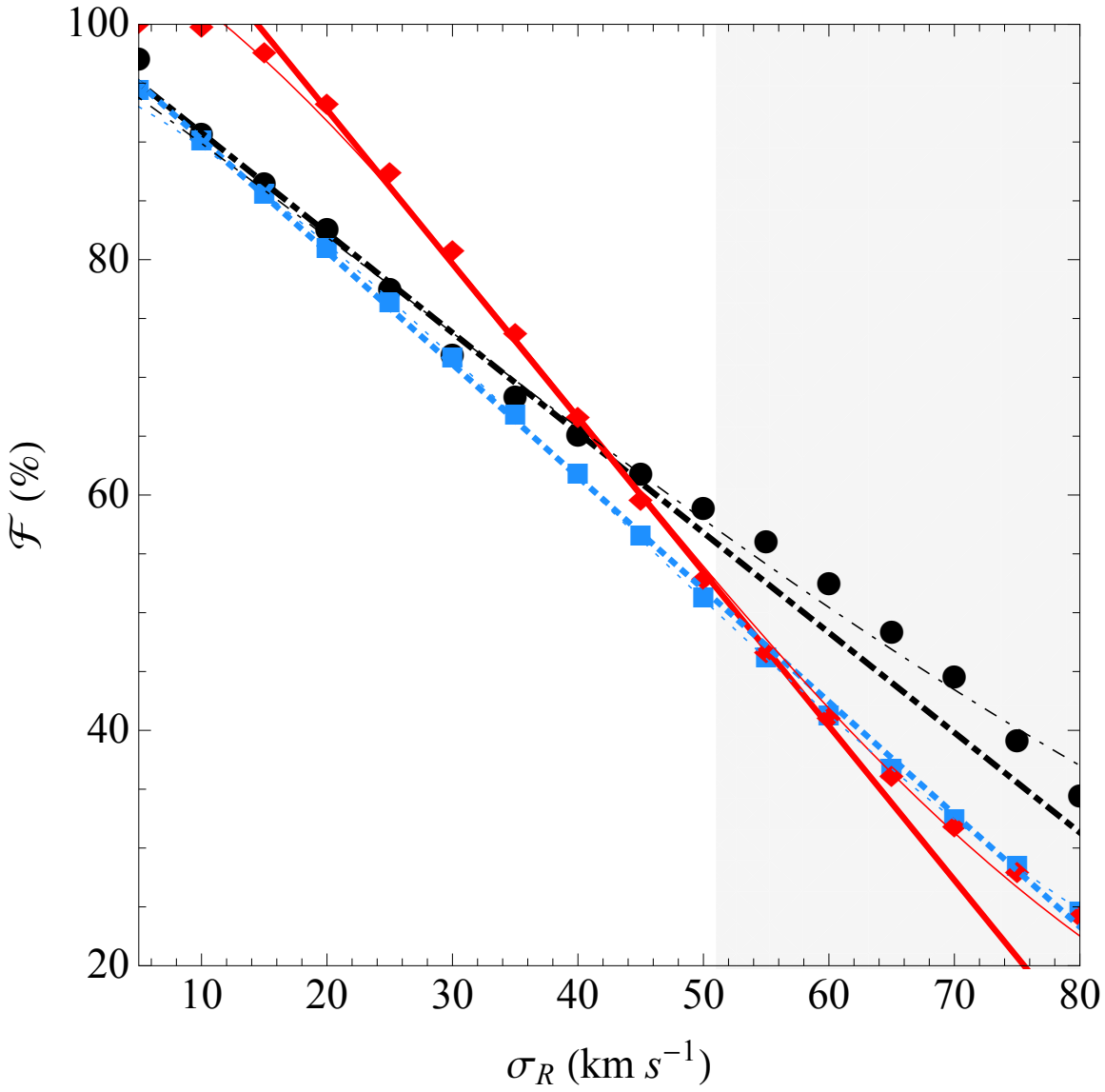

Figure 6.7: Best fit curves for $\mathcal{F}_1$ (solid, red), $\mathcal{F}_2$ (short-dashed, blue) and $\mathcal{F}_{FWHM}$ (dot-dashed, black). Linear fits are shown as thick lines, whereas Gaussian fits are shown as thin lines. The evaluations for $\mathcal{F}_1$, $\mathcal{F}_2$, and $\mathcal{F}_{FWHM}$ from this study are marked with diamonds (red), squares (blue) and circles (black), respectively. The fitting parameters for equation 6.7 are given in Table 6.1 and the fitting parameters for equation 6.8 are given in Table 6.2. The shaded region indicates a radial velocity dispersion $\sigma_R > 50$ km s^{-1}.

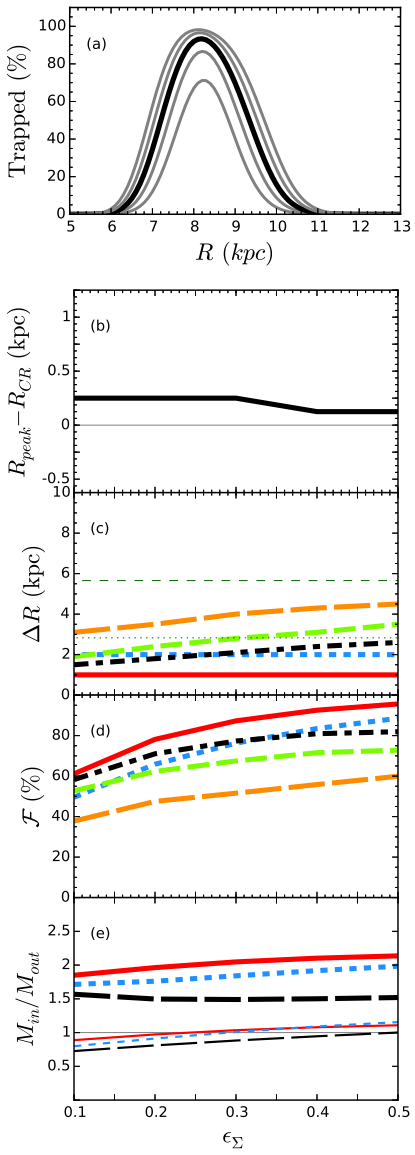

Figure 6.8: Dependence of the integrated fraction on the spiral strength, measured by ϵ_Σ. Panels show (a) the radial distribution of the fraction of stars in trapped orbits, (b) the distance of the peak of the radial trapped fraction profile from corotation ($R_{peak} - R_{CR}$), (c) the radial range (ΔR) within which the integrated fraction is evaluated, (d) the integrated fraction of stars in trapped orbits ($\mathcal{F}_{\Delta R}$), and (e) the ratios for (M_{in}/M_{out}), for $\epsilon_\Sigma = 0.1 - 0.5$ in 0.1 intervals where the initial conditions are otherwise the same as in the scenario for Figure 6.4 with $\sigma_R = 25$ km s^{-1}. The line styles have the same definition as in Figures 6.4-6.6 with the exception that the line in bold in panel (a) signifies the model realization where $\epsilon_\Sigma = 0.3$.

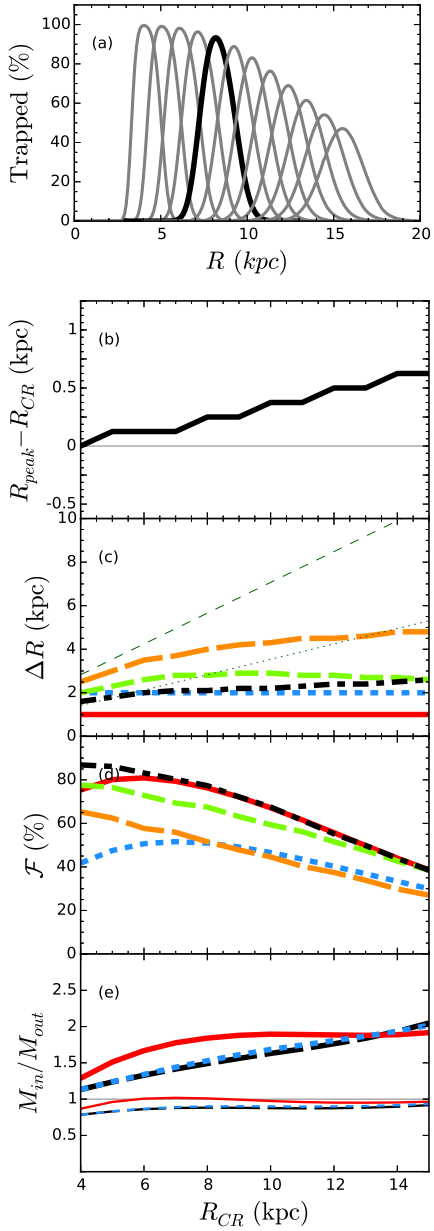

Figure 6.9: Dependence of the integrated fraction on the radius of corotation in the adopted model. Panels show (a) the radial distribution of the fraction of stars in trapped orbits, (b) the distance of the peak of the radial trapped fraction profile from corotation ($R_{peak} - R_{CR}$), (c) the radial range (ΔR) within which the integrated fraction is evaluated, (d) the integrated fraction of stars in trapped orbits ($\mathcal{F}_{\Delta R}$), and (e) the ratios for (M_{in}/M_{out}) for $R_{CR} = 4 - 15$ kpc in 1 kpc intervals where the initial conditions are otherwise the same as in the scenario for Figure 6.4 with $\sigma_R = 25$ km s^{-1}. Line styles are the same as in Figures 6.4- 6.6 with the exception that the line in bold in panel (a) signifies the model realization where $R_{CR} = 8$ kpc.

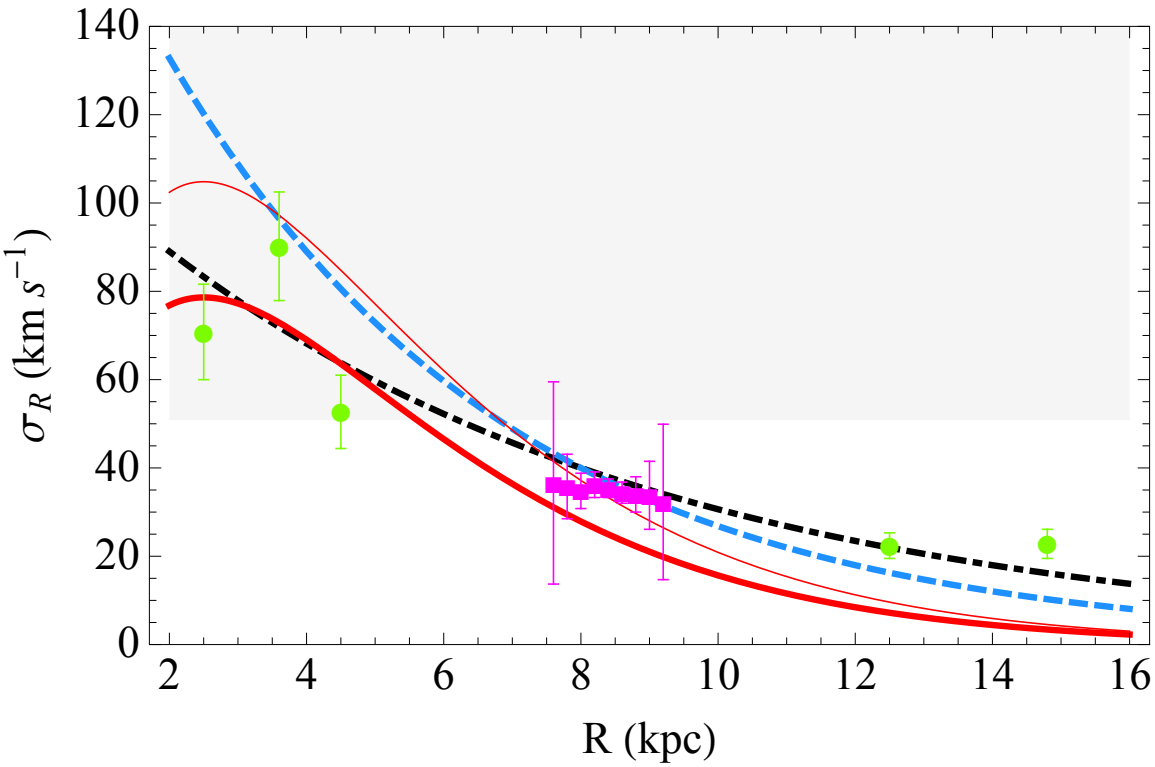

Figure 6.10: Prescriptions for the radial velocity dispersion profile, $\sigma_R(R)$, used in the three models outlined in Table 6.3 with parameter values given in Table 3.1. The curves show $\sigma_R \propto \Sigma(R)^{1/2} \propto e^{-R/2R_d}$ (dashed, blue), $\sigma_R \propto e^{-R/3R_d}$ (dot-dashed, black), and $\sigma_R(R) \propto R\,e^{-R/R_d}$ normalized so that $Q = 1.5$ (thick, red) and $Q = 2$ (thin, red) for a flat rotation curve. For reference, we have plotted observationally derived $\sigma_R(R)$ with error bars for the MW for K-giant stars (green, circles) (Lewis & Freeman, 1989). We also show a selection of "thin disk" stars from the RAVE survey with positions below the galactic plane $-0.5 < z \leq -0.3$ kpc (magenta, squares) (Pasetto et al., 2012), where values for $\sigma_R(R)$ at other Galactic latitudes are not significantly different but have been omitted from this plot for ease of reading. The values for $\sigma_R(R)$ that satisfy $Q = 1.5$ in our model are lower than observed at all radii, suggesting that this model is a poor fit for our Galaxy. The shaded region indicates a radial velocity dispersion $\sigma_R > 50$ km s^{-1}.

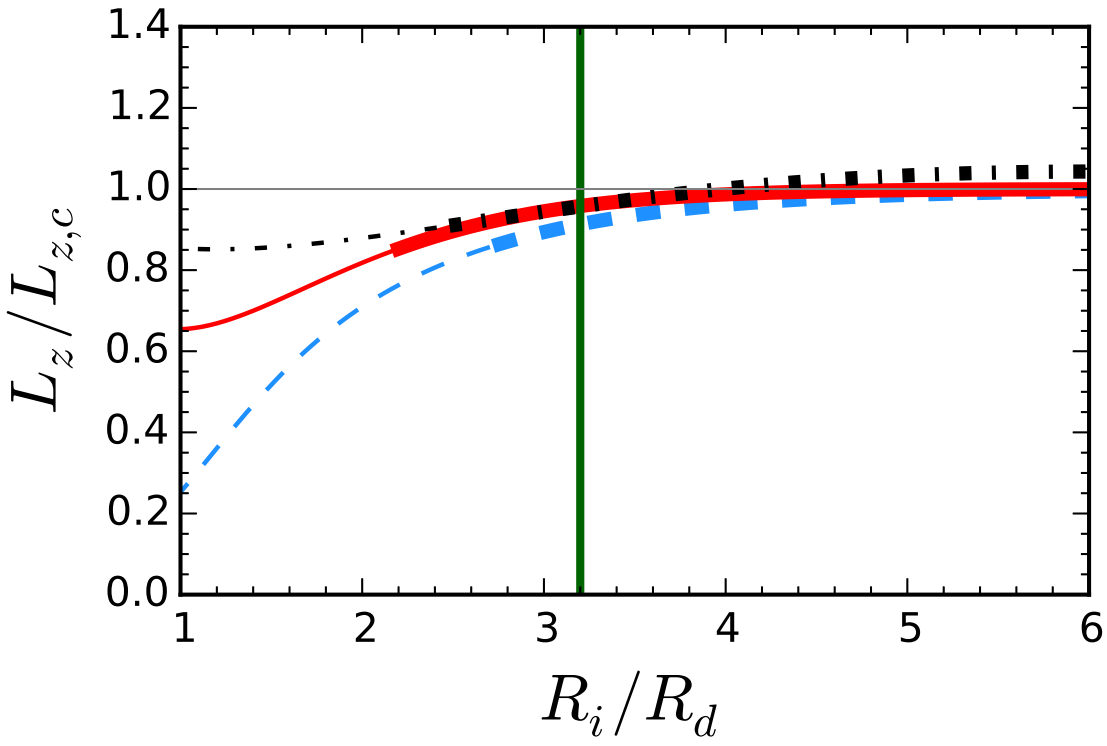

Figure 6.11: Radial distribution of orbital angular momentum for the following three disk models: $f_G(\sigma_R \propto e^{-R/2R_d})$ (blue, dashed), $f_{new}(\sigma_R \propto e^{-R/3R_d})$ (black, dot-dashed), and $f_G(\sigma_R \propto R\, e^{-R/2R_d})$ (red, solid), where $R_d = 2.5$ kpc. Each curve is normalized the orbital angular momentum distribution for an exponential disk that is entirely composed of stars in circular orbits ($L_z(R_i)/L_{z,c}(R_i)$). Each annulus has radial range $dR = 0.1$ kpc. A vertical, green line indicates the radius of normalization ($R_0 = 8$ kpc). Thin lines indicate the radial region where each model has radial velocity dispersion $\sigma_R > 50$ km s^{-1}.

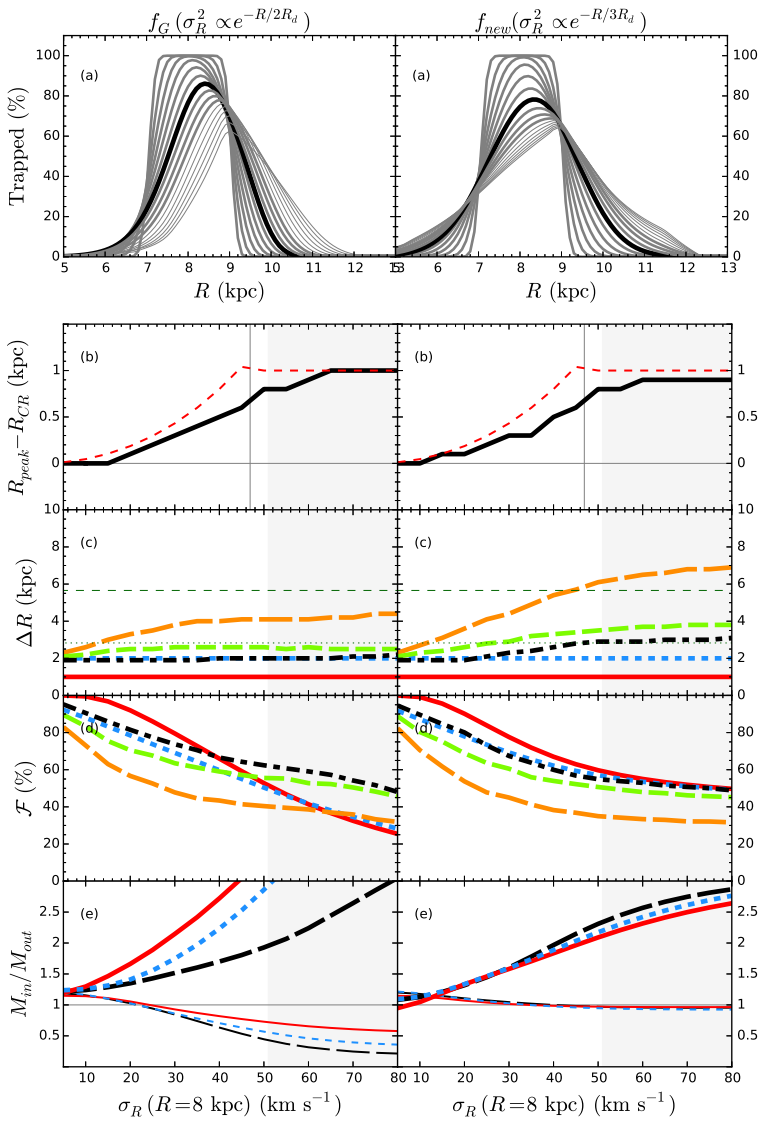

Figure 6.12: Dependence of the integrated fraction on the normalization of the radial velocity dispersion profile assumed to follow $\sigma_R \propto \Sigma(R) \propto e^{-R/R_\sigma}$ for two distribution functions, f_G and f_{new}. Panels show (a) the radial distribution of the fraction of stars in trapped orbits, (b) the distance between the peak of the radial trapped fraction profile and the radius of corotation ($R_{peak} - R_{CR}$), (c) the radial range (ΔR) within which the integrated fraction is evaluated, (d) the integrated fraction ($\mathcal{F}_{\Delta R}$), and (e) the ratios for the various definitions of (M_{in}/M_{out}). Line styles have the same meaning as in Figures 6.4-6.6. For all scenarios, the velocity dispersion is normalized such that $\sigma_R(R = 8 \text{ kpc}) = \{5, 80 \text{ km s}^{-1}\}$ shown in intervals of 5 km s^{-1}. For reference, the case with the velocity dispersion normalized such that $\sigma_R(R = 8 \text{ kpc}) = 35$ km s^{-1} is in bold in panels (a). Thin lines (panels a) and shaded regions (panels b-e) indicate model realizations that use radial velocity dispersion $\sigma_R > 50$ km s^{-1}.

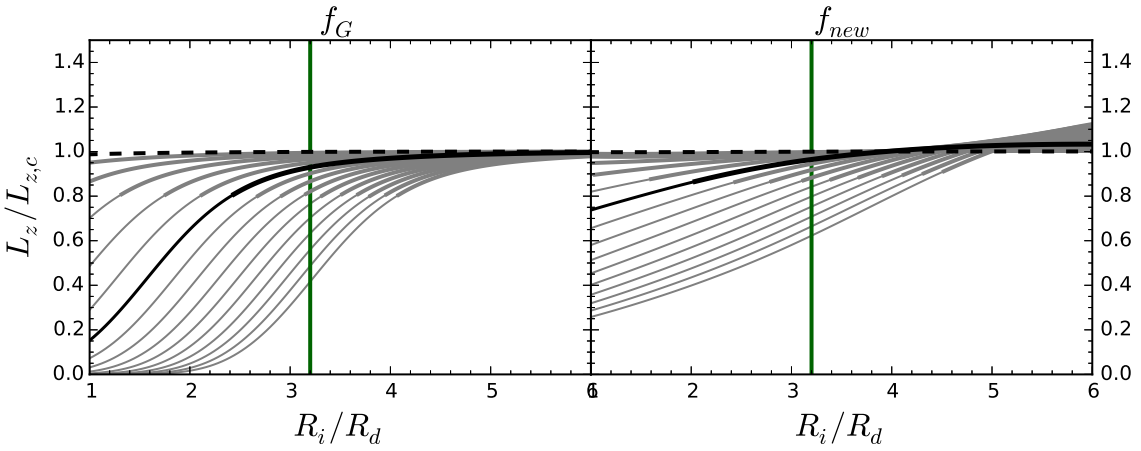

Figure 6.13: Radial distribution of orbital angular momentum for $f_G(\sigma_R \propto e^{-R/2R_d})$ and $f_{new}(\sigma_R \propto e^{-R/3R_d})$ where σ_0 is set such that $\sigma_R(R = 8 \text{ kpc}) = \{5, 80 \text{ km s}^{-1}\}$, shown in intervals of 5 km s^{-1}. Each set of curves is normalized such that the value of the orbital angular momentum equals unity in the annulus where $R_0 = 8$ kpc. For reference, the curves for normalizations that adopt $\sigma_R(R = 8 \text{ kpc}) = 35$ km s^{-1} are shown in black, and those when $\sigma_R(R = 8 \text{ kpc}) = 5$ km s^{-1} are shown as black, dashed curves. A vertical, green line indicates the radius of normalization ($R_0 = 8$ kpc). Thin lines indicate the radial region where each model realization uses a radial velocity dispersion $\sigma_R > 50$ km s^{-1}.

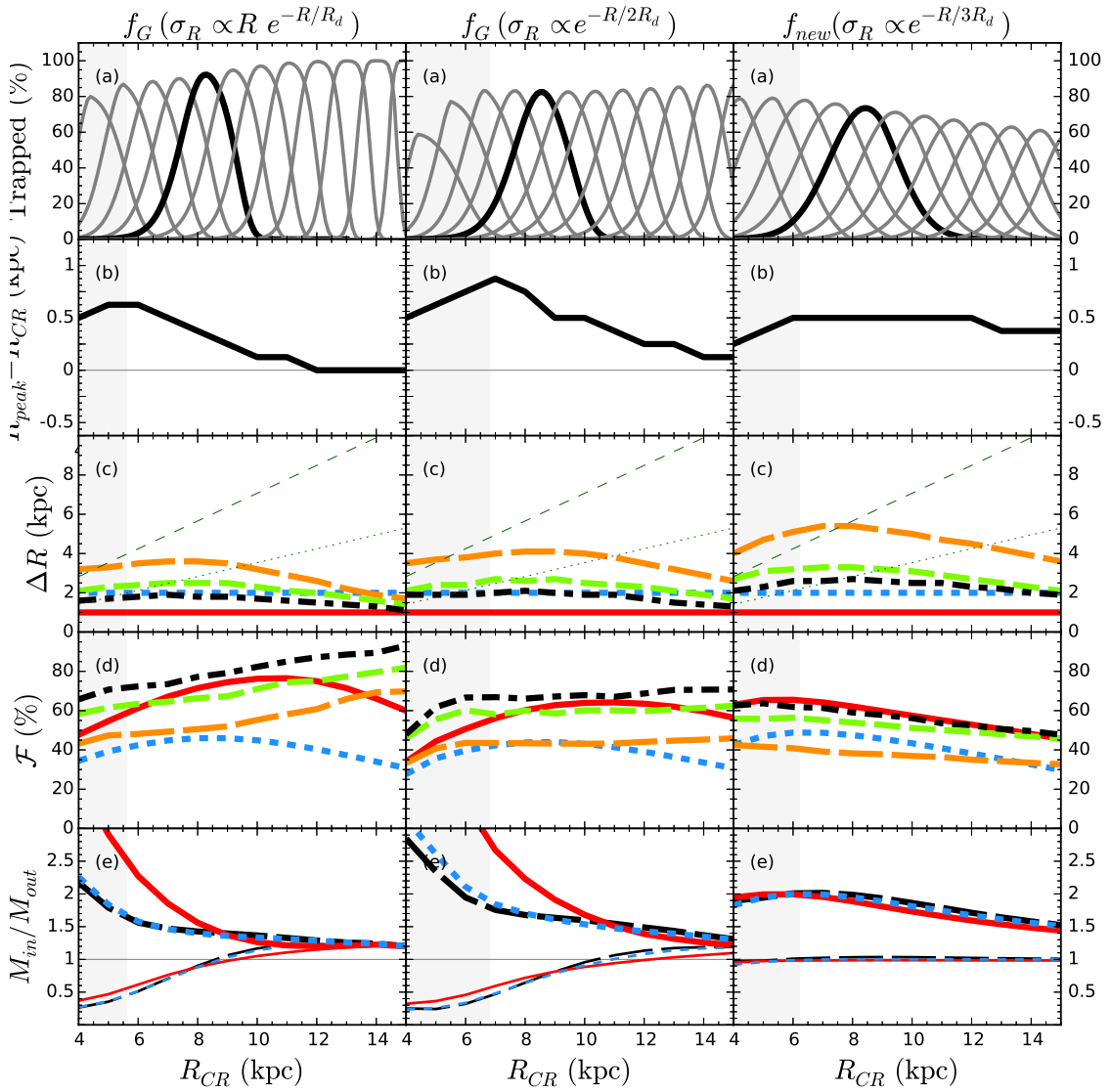

Figure 6.14: Dependence of the integrated fraction on the radius of corotation in models listed in Table 6.3. Each model assumes the radial velocity dispersion profile is radially dependent. Panels show (a) the radial distribution of the fraction of stars in trapped orbits, (b) the distance between the peak of the radial trapped fraction profile and the radius of corotation ($R_{peak} - R_{CR}$), (c) the radial range (ΔR) within which the integrated fraction is evaluated, (d) the integrated ($\mathcal{F}_{\Delta R}$), and (f) the various measures of the ratios for (M_{in}/M_{out}). Line styles have the same meaning as in figs 6.4-6.6. Shaded regions indicate where each model has a radial velocity dispersion $\sigma_R > 50$ km s^{-1}.

Chapter 7

Summary & Conclusions

This work focuses on understanding the physical parameters important to the efficiency of radial migration in disk galaxies (i.e. changes to stellar angular momentum around corotation without associated kinematic heating). A trapped orbit (defined in §2.1), caused by changes in orbital angular momentum from gravitational torques by spiral arms, describes the motion of a star's guiding center radius as it oscillates across and back through the radius of corotation of a spiral perturbation. Should the spiral be transient, a disk star in a trapped orbit could migrate radially, i.e. have a long-lived change in its mean orbital radius reflecting the change in orbital angular momentum.

Should radial migration be an efficient process, it could have a significant impact on the evolution of disk galaxies. Radial migration is most efficient for a single, transient spiral pattern when the RMS change in orbital angular momentum, $\langle(\Delta L_z)^2\rangle^{1/2}$,

for an ensemble of trapped stars is maximized.[1] The value of $\langle(\Delta L_z)^2\rangle^{1/2}$ from a single spiral increases with increasing fraction of stars captured in trapped orbits and with increasing changes in orbital angular momentum for each individual star. We address both of these measures in this work. The following is a summary of our findings and some concluding remarks on the importance of radial migration to spiral galaxy evolution.

7.1 Summary

7.1.1 Capture Criterion

In Chapter 4, we derive the "capture criterion" that determines whether or not a star with some finite radial action (which may be related to orbital random energy by equation 2.3) in a 2D disk is in a trapped orbit (equations 4.17 & 4.18). This is in contrast to the capture criterion for a 2D disk in the literature (Contopoulos, 1978), which assumes zero random orbital energy. We further derive a general expression for the capture criterion in terms of a star's random orbital energy ($E_{ran}(t)$) and orbital angular momentum ($L_z(t)$) in a disk where the underlying potential leads to a given rotation curve (equation 4.26). In a disk with a flat rotation curve the capture criterion ($\Lambda_{nc,2}$) is well described by equation 4.28.

[1] Recall, for radial migration to be efficient over the disk, the duty cycle of transient spiral patterns must be high and have a range of patterns speeds.

We find that orbital angular momentum is the most important factor in determining whether or not a star in the disk is in a trapped orbit, while random orbital energy is less influential. We use the capture criterion to derive an expression for the region, called the "capture region" (§4.1.1), within which a star with zero random orbital energy must be located in order to be captured in a trapped orbit. We propose that whether or not a star is in a trapped orbit is closely approximated by whether or not its guiding center radius ($R_L(t)$) is within the capture region. Radial excursions from random orbital energy may cause a star that is not in a trapped orbit to enter the capture region, or a star that is in a trapped orbit to leave the capture region, but the star's status as captured or not in a trapped orbit is not influenced by these excursions.

A star that is in a trapped orbit will remain in a trapped orbit indefinitely, unless the star is scattered. We define scattering as any event that causes a star to experience a change in it guiding center radius that is associated with a change in random orbital energy. Thus, a scattering event can cause a star that is in a trapped orbit to no longer meet the capture criterion. In an inhomogeneous potential with multiple, small-scale length perturbations, as opposed to the potential we assume for the current study, it is more likely that a star in a trapped orbit will be scattered. We find that when the guiding center radius of a star in a trapped orbit approaches a Lindblad resonance, the star is rapidly scattered out of a trapped orbit. Since the parameter $\Lambda_{nc}(t)$ is a time-dependent quantity, it is important to realize that a star which initially meets

the capture criterion may not remain in a trapped orbit for long enough to migrate radially.

7.1.2 Amplitude of Radial Excursions

The amplitude of the RMS change in orbital angular momentum for an ensemble of trapped stars depends on the maximum amplitude change in orbital angular momentum for each individual star in a trapped orbit. In Chapter 5, we investigate the relationship between the maximum amplitude of radial excursions for a star's guiding center radius (related to changes in orbital angular momentum through equation 2.5) and properties of the spiral potential. We explicitly solve the equations of motion to find the radial excursions of a star in a trapped orbit induced by a spiral density wave (equation 3.3) in a disk with a flat rotation curve. The time dependent radial excursions from corotation for the guiding center radius of a trapped star is given in equation 5.19. Maximum radial excursions are proportional to the fractional amplitude (ϵ_Σ) and tangent of the pitch angle ($\propto \tan\theta$) of the spiral potential.

The radial excursions for the guiding center radius of a star in a trapped orbit due to a spiral pattern are significantly smaller than those induced by a bar pattern with the same the same fractional amplitude. This is a consequence of the differing geometry between the two perturbations, and thus the assumptions allowed for each solution. Further, we find that the maximum radial excursions from a spiral perturbation with parameter values similar to those found in MW-like spiral galaxies, are

smaller or on the order of excursions from epicyclic motions.

7.1.3 Mixed Fraction

The efficiency of radial migration, and thus its importance to the evolution of a spiral disk, is directly related to the fraction of disk stars in trapped orbits. In Chapter 6, we apply the capture criterion to a series of realizations of several models of disk galaxies to investigate how properties of spiral patterns and the adopted distribution function affect the initial distribution of the fraction of stars in trapped orbits and the integrated fraction ($\mathcal{F}_{\Delta R}$) over one of several specified radial ranges (ΔR). In all models, we adopt a disk with an exponential surface density profile and assume an underlying potential that gives rise to a flat rotation curve, with a superposed spiral density wave perturbation (§3.1). The value of the integrated fraction ($\mathcal{F}_{\Delta R}$) sets an upper limit on the migrating fraction stars in the disk (§6.4).

We find that the initial fraction of stars in trapped orbits depends on the radial velocity dispersion (σ_R). At any given radial coordinate R, the velocity dispersion characterizes the width of the azimuthal velocity distribution, and thus the distribution of orbital angular momentum (as $L_z \propto R\, v_\phi$). The capture criterion specifies a range of orbital angular momenta for a star to be in a trapped orbit. The fraction of a stellar population that meets the capture criterion at a given radius therefore depends on the velocity dispersion. For all models explored in this work, the radial distribution for the fraction of stars in trapped orbits grows in radial range but

decreases in peak amplitude with increasing velocity dispersion. Consequently, the integrated fraction of stars in trapped orbits is smaller for stellar populations with higher velocity dispersion.

Under the assumption of a 2D Gaussian velocity distribution at any given coordinate ($f_G(\mathbf{v})_{\mathbf{x}}$), and assuming a shift in the centroid of the velocity distribution toward slower rotation with increasing velocity dispersion (to account for the effects of asymmetric drift, eqn. 3.9), we find that the integrated fraction of stars in trapped orbits depends on the radial velocity dispersion as $\mathcal{F}(\sigma_R) \propto e^{-\sigma_R^2}$ (§6.2). We compare this result with the exponential decrease in $\langle(\Delta L_z)^2\rangle^{1/2}$ with linearly increasing radial velocity dispersion for an ensemble of stars in §6.2.4.

In all models we explored, a greater number of stars are initially in trapped orbits that have guiding center radii inside corotation ($R_L < R_{CR}$) than outside ($R_L > R_{CR}$). This is consistent with the idea that radial migration could have a net effect of moving stellar orbital angular momentum outward. However, it must be noted that our result is indicative only of the distribution of the initial fraction of stars in trapped orbits. In realistic systems, the time-dependent influence of an evolving disk, gas motions, substructure, and irregular and chaotic orbits must also be considered.

7.2 Conclusions

Our results demonstrate that radial migration is not important for high velocity dispersion populations, like old, inner and thick disk populations. Further, radial migration would not have been important at early times, as the early disk likely had a high velocity dispersion (e.g. Genzel et al., 2006; Glazebrook, 2013, and references therein). We expect radial migration to be more important for low velocity dispersion populations, like young disk or outer disk populations. These conclusions are in agreement with the current inside-out formation scenario for disk galaxy evolution (Abadi et al., 2003; Brook et al., 2004; Villalobos & Helmi, 2008; Kazantzidis et al., 2008; Bird et al., 2013; Minchev et al., 2013, 2015) and with the recent interpretation of APOGEE/SDSS-III Data Release 12 data (Hayden et al., 2015) of disk stars in the MW. Hayden et al. (2015) find that the positive skew in the metallicity distribution for stars in the outer disk may be explained by stars that have migrated radially, but the high-α abundance stars (likely the earliest formed stars) in the inner disk ($R \lesssim 11$ kpc) do not have a skew in their metallicity distribution, suggesting radial migration is less influential at early stages of disk formation. Our results are also consistent with the recent finding of *low eccentricity*, super-solar metallicity stars in the solar circle (Kordopatis et al., 2015).

This work has an interesting implication for the formation of outer disks should they be produced through the process of radial migration. In this scenario, stars born inside the truncation radius of the disk migrate radially outward and populate

the outer disk. Recall that trapped stars with low random orbital energy do not have large excursions from their guiding centers and that the guiding center of a star in a trapped orbit is within the capture region. Disk stars that are distant from the galactic center have a low velocity dispersion, and thus individual stars at high galactocentric radii mostly have low random orbital energy. Should the outer disk have formed via radial migration, trapped stars would have had a trajectory that was largely restricted to the area inside the capture region. Therefore, a transient spiral pattern would have had to have existed that produced a capture region which overlapped (or very nearly overlapped) the truncation radius. Otherwise, trapped stars would migrate, but they would not migrate beyond the truncation radius. Such a spiral could not be a transient swing amplified density wave or spiral mode (see for example Lin & Shu, 1964; Toomre, 1969; Sellwood & Carlberg, 2014, and references therein), as these structures require both some finite surface density beyond corotation and an associated bounding end (namely the outer Lindblad resonance). Rather, such a spiral would likely be tidally produced (see Dobbs et al., 2010, for an interesting discussion on the possible corotating nature of tidally induced spirals. As shown in §4.5, transient corotating spirals would induce radial migration across the entire radial range of the spiral pattern.). As it is known that tidally produced arms stimulate star formation (e.g. Chromey et al., 1998; Elmegreen et al., 2007), an outer disk that formed via radial migration would be populated by both old disk stars (that migrated radially) and a generation of stars that formed at the time of closest approach. In the

picture presented here, each population would be both chemically and kinematically distinct. It would be interesting to search for dual populations in outer disks to place constraints on the dynamical nature of tidally induced spiral arms and the role of radial migration as a formation mechanism.

Chapter 8

Future Work

Having investigated the physics important to the distribution and fraction of stars in trapped orbits, I now wish to explore the time-dependent nature of radial migration for an ensemble of stars. For a given fraction of trapped stars, radial migration is most efficient when the timescale for maximizing the value of $\langle(\Delta L_z)^2\rangle^{1/2}$ equals the spiral lifetime. It is therefore critical to understand what drives each timescale and whether or not they may, in fact, be related to one another.

Simulated isolated disk galaxies frequently exhibit transient spiral structure, but there is a large range in the lifetimes of spiral arms in different simulations and no consensus on their dynamical nature much less on the mechanism for their disruption. There are two leading theories at this time: The first theory proposes that a small perturbation to the underlying potential may be amplified through a combination of self gravity, the differential rotation of a disk, and stellar random

motions (Goldreich & Lynden-Bell, 1965; Julian & Toomre, 1966) . In the linear approximation (Julian & Toomre, 1966), such "swing amplified" spirals would rapidly disrupt outside corotation. In high resolution N-body simulations of disk galaxies, D'Onghia et al. (2013) found what they identify as swing-amplified spirals that are self-perpetuating, a phenomenon not expected from the linear theory. The second theory is that transient spirals are swing amplified modes (Sellwood & Carlberg, 2014) with constant pattern speed. Sellwood & Carlberg (2014) propose that these local modes disrupt as a direct consequence of the motions of stars in trapped orbits. Indeed, they invoke the prediction of Sellwood & Binney (2002) that the amplitude of a spiral should be limited by the size of the capture region. This suggests that the same physics that leads to radial migration may also limit the spiral amplitude (Sellwood & Binney, 2002). It is therefore possible that radial migration is a self limiting process.

Whether the spirals produced by D'Onghia et al. (2013) are qualitatively different from those produced by Sellwood & Carlberg (2014) has yet to be determined. However, the role of horseshoe orbits in the disruption of these spirals could lead to important insights about the nature of spiral structure in both simulations.

In future work, I propose to explore the relationship between radial migration and spiral disruption in several stages. First, I will use Monte Carlo realizations of a given distribution function to populate with test particles a disk galaxy that has a single spiral pattern and integrate the orbits over several Gyr. The capture criterion

will allow me to identify trapped stars and then calculate $\langle(\Delta L_z)^2\rangle^{1/2}$ for only these stars. I will identify a timescale for maximizing $\langle(\Delta L_z)^2\rangle^{1/2}$, in the absence of any complications that may arise from multiple spiral patterns or a spiral pattern with radial- or time-dependent pattern speed. This stage will add important insight to later stages of my proposed research as it will act as a control when I do the same analysis on simulations with more complex spiral structure.

The next stages will include the use of snapshots from the above mentioned simulations (D'Onghia et al., 2013; Sellwood & Carlberg, 2014). I will use my capture criterion to find the location and size of the capture region associated with each spiral pattern as well as to identify star particles that are in trapped orbits, and therefore to track the orbital properties of individual trapped stars. This method will enable me to explore the time-dependent relationship between spiral arms and stars in trapped orbits. Additionally, I will continue to devote time toward developing a theoretical framework I have started for understanding spiral disruption due to the presence of trapped orbits. This analytic approach is an extension of the theoretical work on spiral structure by Lynden-Bell & Kalnajs (1972).

After the above steps are complete, I would like to build a suite of chemical evolution models of a MW-like galaxy to explore the impact of radial migration on spiral galaxies.

Appendix A

Two Capture Criteria

In the literature, there are two separate criteria (Binney & Tremaine, 1987; Contopoulos, 1978) for whether or not a star with zero random orbital energy ($E_{ran} = 0$) is in a trapped orbit. The maximum radial excursion for a trapped orbit used by Sellwood & Binney (2002) (their eqn. 12) comes from the the equations of motion used to derive the capture criterion in Binney & Tremaine (1987). This is not the criterion we discuss in §4.1 of this work, but it is related to our derivation of the radial excursions for a trapped orbit due to a spiral pattern (Chapter 5). In this appendix, we outline the set of assumptions used in the derivation of each capture criterion.

A.1 Criterion used by Sellwood & Binney

The capture criterion in Binney & Tremaine (1987) (Chapter 3.3b) is derived using perturbation theory. The disk potential ($\Phi(R, \phi)$) is assumed to be composed of an underlying axi-symmetric potential ($\Phi_0(R)$) plus an m-armed perturbation to the potential ($\Phi_1(R, \phi)$). The effective potential, Φ_{eff} (equation 2.2), is the potential in a frame that rotates with the pattern speed of the perturbation to the potential (Ω_p). Following the derivation from Binney & Tremaine (1987), a minimum in the effective potential at the radius of corotation (R_{CR}, where $\Omega(R) = \Omega_p$) is located at azimuth given by $\phi = 0$. The local maxima in the effective potential (between the arms of the perturbation) are at the radius of corotation and azimuth given by $\phi = \pi/m$ and at consecutive intervals every $2\pi/m$.

It is assumed that the guiding centre of a star in a trapped orbit is located at a local maximum in the effective potential at position (R_0,ϕ_0) = (R_{CR}, π/m). It is further assumed that the equations of motion for a star in a trapped orbit can be described as small, oscillatory excursions around its guiding centre such that $R_1(t)$ is the time dependent radial distance from the radius of corotation ($R_1(t) = R(t) - R_{CR}$), and the azimuthal excursions are described by $\psi(t) = m(\phi(t) - \phi_0)$. Orbital motions around this guiding centre are thus assumed to be similar to an epicyclic excursion in that there is no change in angular momentum.

They show that there is an integral of motion in the rotating frame for a star in

a trapped orbit that is given by (Binney & Tremaine, 1987, equation 3.128),

$$E_p = \frac{1}{2}\dot{\psi}(t)^2 - p^2 \cos\psi(t), \tag{A.1}$$

where (Binney & Tremaine, 1987, equation 3.127b)

$$p^2 = |\Phi_b(R_{CR})| \frac{4}{R_{CR}^2} \frac{(4\Omega_{CR}^2 - \kappa_{CR}^2)}{\kappa_{CR}^2} \tag{A.2}$$

and $|\Phi_b(R_{CR})|$ is the amplitude of the perturbation to the potential evaluated at the radius of corotation and Ω_{CR} and κ_{CR} are the circular and orbital frequencies of a star evaluated at $R_0 = R_{CR}$ in the underlying axi-symmetric potential. In equation A.1, $\frac{1}{2}\dot{\psi}(t)^2$ is the $\hat{\phi}$-directional kinetic energy in the rotating frame and $-p^2\cos\psi(t)$ is the potential in this regime. A star with $E_p < p^2$ will oscillate with simple harmonic motion in the potential described by $-p^2\cos\psi$, whereas a star that does not satisfy this criterion will circulate around the galactic centre in the rotating frame.

We re-express $E_p < p^2$ by using equation A.1, so that,

$$\frac{1}{2}\frac{\dot{\psi}(t)^2}{(1+\cos\psi(t))} < p^2. \tag{A.3}$$

By rearranging some constants and substituting for p,

$$\frac{1}{2}(4\Omega_{CR}^2 - \kappa_{CR}^2)\frac{\kappa_{CR}^2}{4\Omega_{CR}^2}\frac{R_1(t)^2}{(1+\cos\psi(t))} < |\Phi_b(R_{CR})|. \tag{A.4}$$

APPENDIX A. TWO CAPTURE CRITERIA

In a power law potential (e.g., equation 4.19), we can write the relation $\gamma^2\Omega^2 = \kappa^2$, where the value of gamma must satisfy $1 \leq \gamma \leq 2$ (γ is related to β from §4.3 by $\gamma = \sqrt{4-\beta}$). Under this assumption, equation A.4 can be expressed,

$$\frac{1}{2}\frac{(4-\gamma^2)\gamma^2}{4}\Omega_{CR}^2\frac{(R(t)-R_{CR})^2}{(1+\cos\psi(t))} < |\Phi_b(R_{CR})|, \tag{A.5}$$

where we have replaced $R_1(t)$ with $R(t) - R_{CR}$ as defined at the beginning of this section. In a disk with a flat rotation curve ($\gamma^2 = 2$), a star in libration around the local maximum in the effective potential must satisfy

$$\frac{1}{2}\Omega_{CR}^2\frac{(R(t)-R_{CR})^2}{(1+\cos\psi(t))} < |\Phi_b(R_{CR})|. \tag{A.6}$$

A star that has a large value for $R(t) - R_{CR}$ may not satisfy equation A.5 and will circulate about the galactic centre with a guiding centre radius $R_0 \neq R_{CR}$. Indeed, equation A.5 cannot be used to evaluate whether or not a star is in a trapped orbit if $\Omega_0 \neq \Omega_{CR}$ because of the initial assumption that $R_0 = R_{CR}$ and that all non-circular motions come from oscillations about the star's guiding centre, which is located at the local maximum in the effective potential.

The capture criterion derived in Binney & Tremaine (1987) can be used only for stars with zero random energy. It predicts that a star will either meet the capture criterion or be on a circular orbit about the galactic centre. Non-circular motions are produced by a star that meets the capture criterion as it oscillates about its guiding

centre.

A.2 Criterion derived by Contopoulos

The capture criterion discussed in §4.1 and derived by Contopoulos (1978) assumes that the star being evaluated has zero radial action, corresponding to zero random orbital energy by equation 2.3. In this method, the motions of a star in a trapped orbit around the local maximum in the effective potential are caused by changes in that star's angular momentum. Therefore, $R(t) = R_L(t)$. Contopoulos's capture criterion (equation 4.7) has both an upper and lower limit that must be satisfied in order for the star to be in a trapped orbit and can be applied to all disk stars that have zero random orbital energy. The lower limit,

$$\Lambda_c > -1 \tag{A.7}$$

determines the boundary between stars in trapped orbits and stars that circulate about the galactic centre in the rotating frame. We use this limit as the statement that describes a scenario similar to the capture criterion in §A.1 ($E_p < p^2$). One should keep in mind that the capture criterion we now discuss (equation A.7) states whether or not a star with any given angular momentum (and therefore any given guiding centre radius) is in a trapped orbit; whereas, it is assumed in §A.1 that the star has a guiding centre radius at R_{CR}.

We can evaluate equation A.7 by using the same perturbation to the potential as in §A.1. The value of Λ_c is given by equation 4.6. Its evaluation requires one to calculate the Jacobi integral of the star, E_J, given by equation 2.1. The velocity of a star in the rotating frame is given by $\mathbf{x}_\phi(t) = R_L(t)(\Omega_c(R_L(t)) - \Omega_{CR})\hat{\boldsymbol{\phi}} + \mathbf{v}_{ran}$. In the limit that $\mathbf{v}_{ran} \to 0$ (zero random energy), we find that the capture criterion can be expressed as,

$$\frac{[\Phi_0(R_L(t)) - \Phi_0(R_{CR})] + \frac{1}{2}R_L(t)^2|\Omega_c(R_L(t)) - \Omega_{CR}|^2 + \frac{1}{2}\Omega_{CR}^2(R_{CR}^2 - R_L(t)^2)}{(1+\cos\psi(t))} < |\Phi_b(R_{CR})|. \tag{A.8}$$

In a flat rotation curve and in the limit that $\Phi_0(R(t)) \approx \Phi_0(R_{CR})$ and $\Phi_1(R_L(t)) \approx \Phi_1(R_{CR})$, we find,

$$\Omega_{CR}^2 \frac{R_{CR}|R_L(t) - R_{CR}|}{(1+\cos\psi(t))} < |\Phi_b(R_{CR})|. \tag{A.9}$$

The criterion in equation A.9 is neither an exact mathematical nor physical equivalent to the criterion in equation A.6. In the current case (equation A.9) the star has azimuthal motion that is associated with a circular orbit around the galactic centre, where $R(t) = R_L(t)$ and $\Omega_c(R_L(t)) = v_c/R_L(t)$. This method does not assume a priori that $R_L = R_{CR}$, as is the case in §A.1.

Bibliography

Abadi, M. G., Navarro, J. F., Steinmetz, M., & Eke, V. R. 2003, ApJ, 597, 21

Allende Prieto, C., Beers, T. C., Wilhelm, R., Newberg, H. J., Rockosi, C. M., Yanny, B., & Lee, Y. S. 2006, ApJ, 636, 804

Athanassoula, E., Bienayme, O., Martinet, L., & Pfenniger, D. 1983, A&A, 127, 349

Baba, J., Saitoh, T. R., & Wada, K. 2013, ApJ, 763, 46

Barbanis, B. 1976, Celestial Mechanics, 14, 201

Barbanis, B., & Woltjer, L. 1967, ApJ, 150, 461

Barros, D. A., Lépine, J. R. D., & Junqueira, T. C. 2013, MNRAS, 435, 2299

Berrier, J. C., & Sellwood, J. A. 2015, ApJ, 799, 213

Binney, J. 1987, in NATO ASIC Proc. 207: The Galaxy, ed. G. Gilmore & B. Carswell, 399–412

Binney, J., & Tremaine, S. 1987, Galactic dynamics (Princeton University Press)

BIBLIOGRAPHY

—. 2008, Galactic Dynamics: Second Edition (Princeton University Press)

Bird, J. C., Kazantzidis, S., & Weinberg, D. H. 2012, MNRAS, 420, 913

Bird, J. C., Kazantzidis, S., Weinberg, D. H., Guedes, J., Callegari, S., Mayer, L., & Madau, P. 2013, ApJ, 773, 43

Block, D. L., & Puerari, I. 1999, A&A, 342, 627

Bond, N. A., et al. 2010, ApJ, 716, 1

Bovy, J., Rix, H.-W., & Hogg, D. W. 2012a, ApJ, 751, 131

Bovy, J., Rix, H.-W., Liu, C., Hogg, D. W., Beers, T. C., & Lee, Y. S. 2012b, ApJ, 753, 148

Brook, C. B., Kawata, D., Gibson, B. K., & Freeman, K. C. 2004, ApJ, 612, 894

Brown, E. W. 1911, MNRAS, 71, 438

Burnett, B., & Binney, J. 2010, MNRAS, 407, 339

Burnett, B., et al. 2011, A&A, 532, A113

Carlberg, R. G., & Sellwood, J. A. 1985, ApJ, 292, 79

Casagrande, L., Schönrich, R., Asplund, M., Cassisi, S., Ramírez, I., Meléndez, J., Bensby, T., & Feltzing, S. 2011, A&A, 530, A138+

Chandrasekhar, S. 1943, Reviews of Modern Physics, 15, 1

BIBLIOGRAPHY

Chirikov, B. V. 1979, Phys.Rep, 52, 263

Chromey, F. R., Elmegreen, D. M., Mandell, A., & McDermott, J. 1998, AJ, 115, 2331

Contopoulos, G. 1973, ApJ, 181, 657

—. 1975, ApJ, 201, 566

—. 1978, A&A, 64, 323

de Jong, J. T. A., Yanny, B., Rix, H.-W., Dolphin, A. E., Martin, N. F., & Beers, T. C. 2010, ApJ, 714, 663

De Simone, R., Wu, X., & Tremaine, S. 2004, MNRAS, 350, 627

Debattista, V. P., Mayer, L., Carollo, C. M., Moore, B., Wadsley, J., & Quinn, T. 2006, ApJ, 645, 209

Dehnen, W. 1999a, AJ, 118, 1190

—. 1999b, AJ, 118, 1201

Dehnen, W., & Binney, J. J. 1998, MNRAS, 298, 387

Dobbs, C. L., Theis, C., Pringle, J. E., & Bate, M. R. 2010, MNRAS, 403, 625

D'Onghia, E., Vogelsberger, M., & Hernquist, L. 2013, ApJ, 766, 34

Drimmel, R. 2000, A&A, 358, L13

BIBLIOGRAPHY

Elmegreen, B. G., & Elmegreen, D. M. 1983, ApJ, 267, 31

Elmegreen, B. G., Elmegreen, D. M., & Leitner, S. N. 2003, ApJ, 590, 271

Elmegreen, B. G., & Hunter, D. A. 2006, ApJ, 636, 712

Elmegreen, D. M. 1998, Galaxies and galactic structure, ed. Elmegreen, D. M.

Elmegreen, D. M., Chromey, F. R., Bissell, B. A., & Corrado, K. 1999, AJ, 118, 2618

Elmegreen, D. M., & Elmegreen, B. G. 1984, ApJS, 54, 127

Elmegreen, D. M., Elmegreen, B. G., Ferguson, T., & Mullan, B. 2007, ApJ, 663, 734

Elmegreen, D. M., et al. 2011, ApJ, 737, 32

Friel, E. D., & Janes, K. A. 1993, A&A, 267, 75

Fuchs, B. 2001, MNRAS, 325, 1637

Genzel, R., et al. 2006, Nature, 442, 786

Gilmore, G., & Reid, N. 1983, MNRAS, 202, 1025

Gilmore, G., & Wyse, R. F. G. 1985, AJ, 90, 2015

—. 1991, ApJ, 367, L55

Glazebrook, K. 2013, , 30, 56

Goldreich, P., & Lynden-Bell, D. 1965, MNRAS, 130, 125

BIBLIOGRAPHY

Goldreich, P., & Tremaine, S. 1982, ARAA, 20, 249

Grand, R. J. J., Kawata, D., & Cropper, M. 2012, MNRAS, 421, 1529

Hayashi, H., & Chiba, M. 2006, PASJ, 58, 835

Hayden, M. R., et al. 2015, ArXiv e-prints

Holmberg, J., Nordström, B., & Andersen, J. 2009, A&A, 501, 941

Ivezić, Ž., et al. 2008, ApJ, 684, 287

Jones, B. J. T., & Wyse, R. F. G. 1983, A&A, 120, 165

Julian, W. H., & Toomre, A. 1966, ApJ, 146, 810

Jurić, M., et al. 2008, ApJ, 673, 864

Katz, D., Soubiran, C., Cayrel, R., Barbuy, B., Friel, E., Bienaymé, O., & Perrin, M.-N. 2011, A&A, 525, A90

Kazantzidis, S., Bullock, J. S., Zentner, A. R., Kravtsov, A. V., & Moustakas, L. A. 2008, ApJ, 688, 254

Kordopatis, G., et al. 2011, A&A, 535, A107

—. 2015, MNRAS, 447, 3526

Kormendy, J. 2013, Secular Evolution in Disk Galaxies, ed. J. Falcón-Barroso & J. H. Knapen (Cambridge University Press)

BIBLIOGRAPHY

Lacey, C. G. 1984, MNRAS, 208, 687

Lewis, J. R., & Freeman, K. C. 1989, AJ, 97, 139

Lin, C. C., & Shu, F. H. 1964, ApJ, 140, 646

—. 1966, Proceedings of the National Academy of Science, 55, 229

Lin, C. C., Yuan, C., & Shu, F. H. 1969, ApJ, 155, 721

Loebman, S. R., Roškar, R., Debattista, V. P., Ivezić, Ž., Quinn, T. R., & Wadsley, J. 2011, ApJ, 737, 8

Lynden-Bell, D., & Kalnajs, A. J. 1972, MNRAS, 157, 1

Ma, J. 2002, A&A, 388, 389

Ma, J., Zhao, J. L., Shu, C. G., & Peng, Q. H. 1999, A&A, 350, 31

Martinet, L. 1974, A&A, 32, 329

Martínez-Barbosa, C. A., Brown, A. G. A., & Portegies Zwart, S. 2015, MNRAS, 446, 823

Matteucci, F., & Francois, P. 1989, MNRAS, 239, 885

Minchev, I., & Famaey, B. 2010, ApJ, 722, 112

Minchev, I., Famaey, B., Combes, F., Di Matteo, P., Mouhcine, M., & Wozniak, H. 2011, A&A, 527, A147+

BIBLIOGRAPHY

Minchev, I., Famaey, B., Quillen, A. C., Dehnen, W., Martig, M., & Siebert, A. 2012, A&A, 548, A127

Minchev, I., Martig, M., Streich, D., Scannapieco, C., de Jong, R. S., & Steinmetz, M. 2015, ApJL, 804, L9

Minchev, I., et al. 2013, ArXiv e-prints

Nordström, B., et al. 2004, A&A, 418, 989

Papayannopoulos, T. 1979a, A&A, 77, 75

—. 1979b, A&A, 79, 197

Pasetto, S., et al. 2012, A&A, 547, A71

Peñarrubia, J., McConnachie, A., & Babul, A. 2006, ApJL, 650, L33

Pichardo, B., Martos, M., Moreno, E., & Espresate, J. 2003, ApJ, 582, 230

Pohlen, M., & Trujillo, I. 2006, A& A, 454, 759

Rix, H.-W., & Zaritsky, D. 1995, ApJ, 447, 82

Roca-Fàbrega, S., Valenzuela, O., Figueras, F., Romero-Gómez, M., Velázquez, H., Antoja, T., & Pichardo, B. 2013, MNRAS, 432, 2878

Roškar, R., Debattista, V. P., Quinn, T. R., & Wadsley, J. 2012, MNRAS, 426, 2089

Roškar, R., Debattista, V. P., Stinson, G. S., Quinn, T. R., Kaufmann, T., & Wadsley, J. 2008, ApJL, 675, L65

Ruchti, G. R., et al. 2011, ApJ, 737, 9

Schmidt, M. 1959, ApJ, 129, 243

—. 1963, ApJ, 137, 758

Schönrich, R., & Binney, J. 2009a, MNRAS, 396, 203

—. 2009b, MNRAS, 399, 1145

Searle, L., & Sargent, W. L. W. 1972, ApJ, 173, 25

Seigar, M. S., & James, P. A. 1998, MNRAS, 299, 685

Sellwood, J. A. 2014a, Reviews of Modern Physics, 86, 1

—. 2014b, Reviews of Modern Physics, 86, 1

Sellwood, J. A., & Binney, J. J. 2002, MNRAS, 336, 785

Sellwood, J. A., & Carlberg, R. G. 2014, ApJ, 785, 137

Shu, F. H. 1969, ApJ, 158, 505

Solway, M., Sellwood, J. A., & Schönrich, R. 2012, MNRAS, 422, 1363

Somerville, R. S., & Davé, R. 2014, ArXiv e-prints

Spitzer, Jr., L., & Schwarzschild, M. 1953, ApJ, 118, 106

Steinmetz, M., et al. 2006, AJ, 132, 1645

Struck, C., Dobbs, C. L., & Hwang, J.-S. 2011, MNRAS, 414, 2498

Toomre, A. 1964, ApJ, 139, 1217

—. 1969, ApJ, 158, 899

Vallée, J. P. 2002, ApJ, 566, 261

—. 2015, MNRAS, 450, 4277

van der Kruit, P. C. 1987, A&A, 173, 59

van der Kruit, P. C., & Searle, L. 1981, A&A, 95, 105

Vera-Ciro, C., D'Onghia, E., Navarro, J., & Abadi, M. 2014, ApJ, 794, 173

Villalobos, Á., & Helmi, A. 2008, MNRAS, 391, 1806

Wielen, R. 1977, A&A, 60, 263

Wielen, R., Fuchs, B., & Dettbarn, C. 1996, A&A, 314, 438

Wyse, R. F. G., Gilmore, G., Norris, J. E., Wilkinson, M. I., Kleyna, J. T., Koch, A., Evans, N. W., & Grebel, E. K. 2006, ApJ, 639, L13

Wyse, R. F. G., & Silk, J. 1989, ApJ, 339, 700

Curriculum Vitae

Kathryne Daniel received her A.B. from Bryn Mawr College where she majored in Physics and Classical & Near Eastern Archaeology, graduating Cum Laude and with Honors. After college, she spent close to a year bicycling in Europe before deciding to pursue a career in Astrophysics. She received her M.A. in Astronomy (2005) from Johns Hopkins University working with Dr. Karl Glazebrook before taking leave to start a family. In 2009, she returned to Johns Hopkins to complete her Ph.D. In 2011, she was awarded the three year National Science Foundation Graduate Research Fellowship and in 2014 she received the AAUW American Dissertation Fellowship. During her Ph.D. work, she was selected to participate in a summer school for High Performance Astro-Computing for galaxy simulation (2010), two *International Gaia Schools* (2012, 2013), and the *International School for Modeling in Astrophysics: Gravitational Dynamics* (2014). Starting in August 2015, Kathryne will begin an appointment as Visiting Assistant Professor at Swarthmore College, where she will continue her research and teach classes in astronomy.